2017

Precision Metrology of Laser Plasmas in the XUV Band

John Szilagyi
University of Central Florida

PRECISION METROLOGY OF LASER PLASMAS IN THE XUV BAND

by

JOHN M. SZILAGYI
B. S. Electrical Engineering, University of Central Florida, 2007
M. S. Electrical Engineering, University of Central Florida, 2010
M. S. Physics – Photonics, Friedrich Schiller University of Jena, Jena, Germany 2011

A dissertation submitted in partial fulfillment of the requirements
for degree of Doctor of Philosophy
in the Department of Electrical and Computer Engineering
in the College of Engineering and Computer Science
at the University of Central Florida
Orlando, Florida

Summer Term
2017

Major Professor: Martin C. Richardson

ABSTRACT

The XUV band, a region of light spanning the wavelength range of 5 - 200 nm, is located between the Ultraviolet and X-ray regions of the electromagnetic spectrum. It is further divided into a 100 - 200 nm region called the Vacuum Ultraviolet (VUV), and a 5 – 100 nm region called the Extreme Ultraviolet (EUV). Applications of this light have been slow to develop due to the lack of suitable sources, efficient optics, and sensitive detectors. Recently, many industries such as the semiconductor manufacturing industry, medical surgery, micromachining, microscopy, and spectroscopy have begun to benefit from the short wavelengths and the high photon energies of this light. At present, the semiconductor chip industry is the primary reason for the investment in, and development of, XUV sources, optics, and detectors.

The demand for high power EUV light sources at 13.5 nm wavelength is driven by the development of the next generation of semiconductor lithography tools. The development of these tools enables the continued reduction in size, and the increase in transistor density of semiconductor devices on a single chip. Further development and investigation of laser produced plasma EUV light sources is necessary to increase the average optical power and reliability. This will lead to an increase in the speed of EUV lithographic processes, which are necessary for future generations of advanced chip design, and high volume semiconductor manufacturing.

Micromachining, lithography, and microscopy benefit from improvements in resolution due to the shorter wavelengths of light in the VUV band. In order to provide adequate illumination for these applications, sources are required which are brighter and have higher average power. Laser produced plasma (LPP) VUV light sources are used extensively for lithography and defect detection in semiconductor manufacturing. Reductions in the wavelength

and increases in the average power will increase the rate and yield of chip manufacture, as well as reduce the costs of semiconductor manufacture.

The work presented in this thesis, describes the development of two laser plasma source facilities in the Laser Plasma Laboratory at UCF, which were designed to investigate EUV and VUV laser plasma sources. The HP-EUV-Facility was developed to optimize and demonstrate a high power 13.5 nm EUV LPP source. This facility provides high resolution spectroscopy across 10.5 - 20 nm, and absolute energy measurement of 13.5 nm +/- 2% in 2π sr. The VUV-MS-Facility was developed to investigate VUV emission characteristics of laser plasmas of various target geometries and chemistries. This facility provides absolute calibrated emission spectra for the 124 - 250 nm wavelength range, in addition to, at wavelength plasma imaging. Calibrated emission spectra, in-band power, and conversion efficiency are presented in this work for gas targets of Argon, Krypton, and Xenon and solid targets of Silicon, Copper, Molybdenum, Indium, Tantalum, Tin, and Zinc, across the laser intensity range of $8.0 \times 10^6 - 3.2 \times 10^{12}$ W/cm^2.

To my wife Deborah and my family

ACKNOWLEDGMENTS

I would like to thank Dr. Richardson for his support, invaluable guidance, and the many opportunities he provided, without which my work would not be possible. During my time at LPL there are many people who helped contribute to this work. Many thanks to Dr. Masnavi for his extensive expertise in modeling of laser plasmas, and his invaluable discussions and help. I am very grateful to Dr. Parchamy's valuable work in developing plasma sources and metrology discussed in this study, and analysis of experimental data. Special thanks to Dr. Matthieu Baudelet for his support, and invaluable help with spectroscopy. I would like to acknowledge Yuseong Jang, for his interdental work in developing the VUV imaging system, and work in developing the facilities discussed in this work. To Nathan Bodnar who was instrumental in designing and developing the EUV Source in this research, including the ADaPTS control system, and to Josh Bradford who was instrumental in designing and developing the EUV Source's high power laser systems. I would also like to thank everyone mentioned above, and LPL for their friendship. To my family, for all your love and support. Finally, to the most important person in my life, my wife Deborah, I am eternally grateful for her love, patience, and encouragement.

TABLE OF CONTENTS

LIST OF FIGURES

LIST OF ACRONYMS

AR	–	Anti-reflective
BW	–	Bandwidth
CaF_2	–	Calcium fluoride
CCD	–	Charged coupled device
CE	–	Conversion efficiency
CRE	–	Collisional-radiative equilibrium model
DPP	–	Discharge produced plasmas
DPSS	–	Diode pumped solid state
Yb:YAG	–	Erbium-Doped Yttrium Aluminum Garnet
EUV	–	Extreme ultraviolet
EUVL	–	Extreme ultraviolet lithography
HHG	–	High harmonic generation
HP-EUV-Facility	–	High Power EUV Source Facility
HR	–	High reflectivity
HVM	–	High volume manufacturing
HR	–	High-reflectivity
IBA	–	Inverse Bremsstrahlung absorption
LiF_2	–	Lithium fluoride
LPL	–	Laser Plasma Laboratory
LPP	–	Laser produced plasma
LTE	–	Local thermal equilibrium

MCP	–	Multi-channel plate
MgF_2	–	Magnesium fluoride
MLM	–	Multi-layer mirror
NA	–	Numerical aperture
Nd:YAG	–	Neodymium-Doped Yttrium Aluminum Garnet
$Nd:YVO_4$	–	Neodymium-Doped Yttrium Vanadate
PID	–	proportional-integral-derivative
sccm	–	Standard cubic centimeter
slm	–	Standard liter per minute
SNR	–	Signal to noise ratio
Sn	–	Tin
SnCl2	–	Tin (II) chloride
TEC	–	Thermoelectric cooler
TIR	–	Total internal reflection
VUV	–	Vacuum ultraviolet
VUV-MS-Facility	–	VUV Metrology Source Facility
UTA	–	Unresolved transition array
UV	–	Ultraviolet
XUV	–	Extreme ultraviolet

CHAPTER 1: INTRODUCTION

Light is what allows us to know our universe. For centuries humans have relied on it to understand and survive in our world. The sun, the moon and the stars, were the only sources of light until fire was harnessed. Harnessing this new source of light provided the means to see in the dark and as well as a source of heat. As man studied and refined the use of fire, brighter, controlled, and more reliable sources of light became available. Light sources continued to develop. However, little was understood about the nature of light, until in the 17th century when Isaac Newton discovered that white light from the sun was composed of different colors. [1] This discovery opened the field of spectroscopy and started investigation of different types of light.

In 1816 Michael Faraday theorized that "radiant matter" was a fourth state of matter unlike solid, liquid, and gas. [2] With the development of electricity, thorough investigations of the properties of this "matter" was possible. Experiments performed by William Crookes in 1879, where he passed electricity through evacuated glass tubes (Crookes Tubes), determined that "radiant matter" was indeed a 4th matter state. [2] After years of investigation by others, it wasn't until 1927 when Irving Langmuir coined the term plasma, after likening to the flow of charged particles to how blood carried particles. [3] Building on Crookes work and others investigating the properties of plasma, Wilhelm Röntgen earlier in 1895 had covered a modified Crookes tube with black paper, to block the visible light emission due to florescence of the glass. The tube was modified to have the glass at the anode end of the tube replaced by aluminum, in order to allow the electrons in the cathode ray to pass through into the air. When preparing for this experiment, he darkened the room and noticed a phosphorescent screen shimmering nearby on a table. Not knowing what the phenomenon was, he surmised that a radiant energy was

emanating from the tube. He called them x-rays, where "X" denoted something unknown and rays because they seemed unimpeded by many common materials. [4] Unknown to Röntgen, x-rays were being formed by the deceleration of the electrons through Bremsstrahlung emission when they interacted with the atoms in the aluminum window of the Crookes tube. Applications using x-rays to image internal body structures such as bones were quickly developed, without understanding what X-rays were. Initially, x-rays were ruled out to be light, because they did not refract, reflect, or diffract when interacting with "normal" materials. Eventually they were proven to be a form of light by Max von Laue in 1912, when he demonstrated diffraction of x-rays through a crystal, while simultaneously confirming that crystals are composed of regularly spaced space charges. The use of these new plasma sources opened up the light spectrum, and provided a valuable tool for investigating physical phenomenon in applications such as x-ray imaging, and crystal diffraction.

Most man made light sources for x-rays and UV light were discharge based plasma sources, until laser plasmas were developed. When the laser was demonstrated by Theodore Maiman in 1960, an explosion of research into increasing laser power was started. The intensity and spatial coherence of laser light made it possible to concentrate photon energy into a small millimeter to micron sized areas. When directed onto absorptive materials small localized plasmas could be created through the processes of multi-photoionization, thermionic photoemission, and inverse Bremsstrahlung. Initially the main use for laser plasmas were for modifying solid materials and for spectroscopy. The light emission from these plasmas provided many wavelengths of light, from IR through UV. Eventually laser plasmas reached energies high enough that when focus produced intensities higher than ~10^{10} W/cm^2, high enough to provided emission of high energy photons with wavelengths through the x-ray region. Today laser plasma

sources are commonly used to produce light across the light spectrum. Much of the ultraviolet (UV) through x-ray spectrum is still being explored using these laser plasmas.

Light sources in the XUV band have had an increase in the demand for industrial applications. This band falls between UV and Soft X-ray (Figure 1.1), covering wavelengths from 5 nm (250 eV) to 200 nm (6 eV). The XUV band is further subdivided into extreme ultraviolet (EUV) and vacuum ultraviolet (VUV) bands. Photons in these bands have characteristic energies high enough to cause photoionization in most materials such as oxygen, nitrogen, aluminum, and silicon. Here when a photon is absorbed into an atom, an electron gains enough energy to transition from a bound to a free state. Another characteristic of the XUV band is the high to total absorption of photons in atmospheric gases, due to photoionization and photon energies exceeding the band gaps of materials. High absorption limits the use of transmissive optics to the longer wavelengths of the VUV band, while optics in the EUV band rely almost exclusively on reflective or diffractive optics.

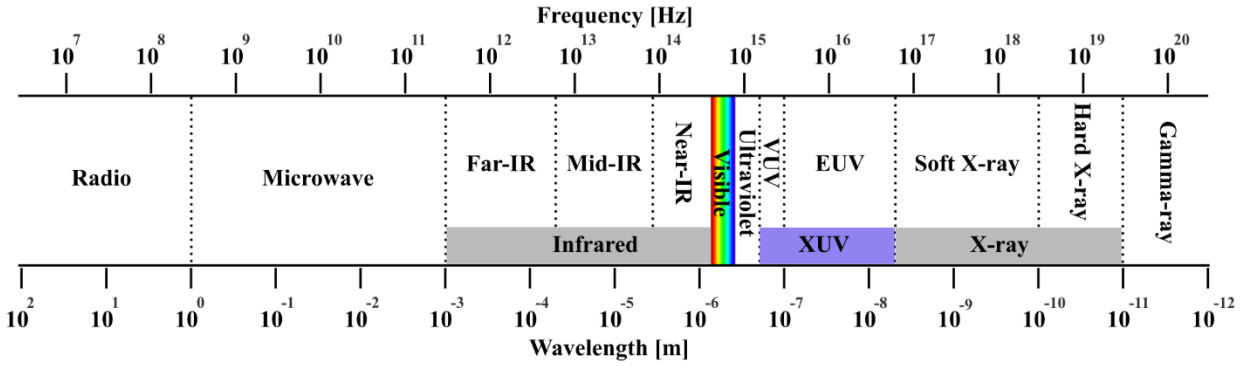

Figure 1.1: XUV band show in relation to other bands of light in the electromagnetic spectrum

Due to the short optical wavelengths and high photon energy of EUV and VUV light, scientific and industrial applications are continuously being developed. Light in these bands has

been used in a wide variety of fields including micromachining [5] [6], lithography [7] [8] [9] [10], spectroscopy [11] [12], and microscopy [13] [14]. Covering all of these fields, the semiconductor industry has one of the most prevalent uses of this of XUV band. With applications that require imaging of the source to small scales, such as micromachining, lithography, and microscopy, high brightness and low etendue are important. Etendue, is a product of the source size and solid angle of emission which is subtended by the imaging system aperture, and defines how well a system can collect light. Since the etendue does not decrease through an imaging system, the collection of light from a source is primarily limited by the source size; therefore, achieving low etendue sources is optimal for high power applications such as lithography and micro machining. The more optical power from the source that can be collected and therefore used, the quicker an imaging application process can be performed. Additionally, higher power sources are also need to compensate for transmissive and reflective losses in the optical elements of XUV systems.

The semiconductor industry continually drives to increase the computing power of semiconductor devices while striving to reducing or maintaining the cost of manufacturing through lithography. Lithography is a multi-step process that is used to build semiconductor devices. In this process, a silicon wafer is coated with a photosensitive resist that when exposed to light can be etched with an acid. Light is projected onto the resist in the pattern to be etched. The unexposed areas of the resist are removed exposing the semiconductor to the etchant, resulting in an etched structure in the wafer. Then the resist is removed from the wafer and additional material is deposited. This process is repeated several times producing the complex structures necessary to create semiconductor devices. The light currently used in this process is 193 nm VUV light. However, the industry is currently reaching limits of resolution due to the

relatively long wavelengths of current 193 nm VUV sources with respect to semiconductor feature sizes near to 10 nm. In order to continue to reduce feature sizes further, the need for high power shorter wavelength EUV sources is growing. Current wavelength limitations are reduced with EUV Lithography, providing higher resolution lithography for producing smaller semiconductor device feature sizes. EUV Lithography will allow for further reduction in semiconductor feature size, and therefore increase the density semiconductor devices. [15] In order for EUV laser produced plasma sources to realize this need, they must be developed to provide sufficient light for adoption into high volume manufacturing.

Due the industrial demand for high power XUV sources, two laser produced plasma source facilities were developed within the Laser Plasma Laboratory. The High Power EUV Source Facility (HP-EUV-Facility) was developed to optimize and demonstrate a high power 13.5 nm EUV laser produced plasma (LPP) source. This source target is a tin based mass limited liquid droplet. It is irradiated by a 1030 nm, 2kW maximum average power, 100 mJ maximum pulse energy, 43 ns pulse width thin-disk laser with at target intensities up to 1.6×10^{11} W/cm^2. This facility provides high resolution spectroscopy across 10.5 – 20 nm, and absolute energy measurement of 13.5 nm+/- 2% in 2π sr. The other laser plasma facility developed is the VUV-MS-Facility. It was developed to investigate VUV emission characteristics of laser plasmas. This facility supports various target geometries including planar targets, bulk gas, and gas jet targets. The facility has two laser systems which provide an at target intensity of $4.9 \times 10^6 – 2.2 \times 10^{11}$ W/cm^2. One laser is a flash lamp pumped laser with a wavelength of 1064 nm, 35W maximum average power, 350 mJ maximum pulse energy, with 10ns pulse, the other is fiver laser with a wavelength of 1064 nm, 500W maximum average power, 42 mJ maximum pulse energy, with a 60 – 500 ns pulse width. The VUV-MS-Facility provides absolute calibrated emission spectra for

the 250 – 124 nm wavelength range, and high resolution spectra for 124 – 22 nm, as well as at wavelength plasma imaging. The development of these plasma source facilities is presented in this thesis. Additionally, calibrated emission spectra, in-band power, and conversion efficiency is presented for gas targets of Argon, Krypton, and Xenon and solid targets of Silicon, Copper, Molybdenum, Indium, Tantalum, Tin, and Zinc, across a laser intensity range of $8.0x10^{6}$ – $3.2x10^{12}$ W/cm^2. This work developed two source facilities for investigation of laser plasma sources for the XUV wavelength region. It also presents and demonstrate plasma source candidates for VUV and 13.5 nm EUV light generation.

1.1 EUV Radiation

The Extreme Ultraviolet (EUV) wavelength band is the band of light between x-rays and vacuum-ultraviolet (VUV) light, with a corresponding wavelength of 5 nm (250 eV) to 100 nm (12 eV) (Figure 1.2). [16] [17] EUV light is a photo ionizing radiation, where the photon energy is sufficient to excite a bound electron to a free state. Also light in this band has energies that overcome the work function of solid metals, which range from 2.1 – 6.4 eV. [18] This energy is the minimum energy necessary to move an electron from the surface of the metal to a point just outside the surface of a metal. The energies of EUV photons are also effective at breaking atomic bonds of molecules in most materials. Typical photon energies for breaking common molecular bonds between atoms like carbon, oxygen, nitrogen, and silicon range from 1.51 – 11.11 eV. [19] All of these physical processes add challenges to the use of materials with EUV light, as they will degrade with time. In addition to degradation, buildup of charge in materials due to these electrons and ions, can create damaging electrical currents for semiconductor devices.

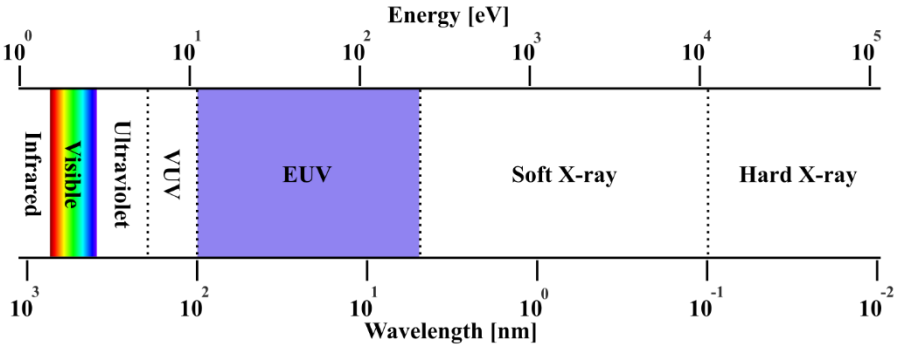

Figure 1.2: EUV band shown in relationship to the optical spectrum

EUV photon energies are higher than the band gaps of all semiconductors which range between .08 – 6.36 eV [20], and insulators which range between 9 – 22.1 eV. [21] Additionally, these energies are sufficient to photoionize most materials. These processes cause high absorption into many materials. In solids, EUV light has absorption lengths less than 1 μm. This prevents standard optics such as lenses from being used and requires the use of grazing incidence or, high precision multi-layer reflection optics. Absorption in air is also very high and applications require low atmospheric pressures on the order of 10^{-4} Torr.

1.1.1 Sources and Application

The generation of EUV radiation can be accomplished in many ways. Sources of these sources can be divided into two groups: spectrally coherent and incoherent light sources. Spectrally coherent light is light which has a constant phase difference between waves within the light. A key property of coherent light waves is their ability to constructively and destructively interfere with each other. As discussed in Section 1.1.1.1 coherent EUV sources include synchrotron sources, lasers, and high harmonic generation sources. These sources have a monochromatic wavelength and are typically tunable across tens of nanometers. Coherent

sources also typically have bright emission with narrow beam emission. Incoherent sources, as discussed in Section 1.1.1.2, include discharge sources and laser plasma sources. These sources have broadband emission composed of a relatively narrow EUV band and out-of-band emission in the infrared through VUV, which makes up the majority (>95%) of emission. These sources, have large solid angles of emission, and can reach average powers of several hundreds of watts. For imaging application such as lithography, incoherent light prevents aberrations due to optical interference.

The following sections (Section 1.1.1.1 and Section 1.1.1.2) describe several common sources for coherent and incoherent EUV light. Examples and ranges of some of the key optical parameters such as average power, emission angles, and wavelength content are given for comparison. Additionally, some of the key applications are also described.

1.1.1.1 Coherent EUV Sources

Synchrotron sources are one of the most important sources fundamental to research in EUV light. These high brightness pulsed sources are highly coherent and have high spectral bandwidth ranging from 10 eV to 10000 eV. [22] These dependable stable sources rely on strong magnetic fields, on the order of a few Tesla, [23] to accelerate bunches of electrons along curved trajectories at relativistic speeds. [24] Due to the conservation of energy and momentum, photons are emitted tangentially to the curvature of the electron path in a conical distribution. As seen in Figure 1.3, the synchrotron source is composed of an electron gun, which feeds a booster ring with electrons. The booster ring then accelerates the electrons to relativistic speeds into a storage ring. The polygonal ring has several straight sections separated by bending magnets. The conical

emission at these magnets has an emission angle proportional to the angular change in the electrons trajectory and $1/\gamma$, where γ is the Lorentz factor. [25] The number of photons emitted is proportional to the number of electrons in the beam, [26] with average power as high as hundreds of kW. [22]

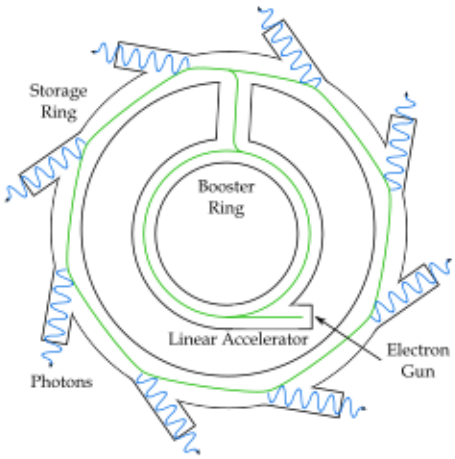

Figure 1.3: Synchrotron radiation facility layout

In the straight sections of synchrotrons, devices are inserted to greatly increase the intensity of the emitted radiation. These are called wigglers and undulators. Each of these are tuned to have different properties and wavelengths, and are used as an individual facility, which is called a beam line. [27] Both undulators and wigglers use alternating magnetic fields of several Tesla to apply a sinusoidal motion to the electron trajectory. The Undulator Strength Parameter defined as,

$$K = \frac{eB_0\lambda_u}{2\pi m_e c} = 0.934 \cdot B_0\lambda_u \qquad (1.1)$$

where e is the charge of an electron, B_0 is the magnetic field of the undulator, λ_u is the spatial period of the undulator's magnets, m_e is the electron rest mass, and c is the speed of light. When this parameter is less than one then the device is considered an undulator, if it is much larger than 1, on the order of 10, it is considered a wiggler. Undulators use a lower intensity magnetic field, less than a couple of Tesla, to produce monochromatic narrow line emission and its harmonics. The angle of emission is typically tens of μrad and is defined as, $\theta = 1/(\gamma\sqrt{N})$ where γ is the Lorentz factor, and N is the number of periods in the undulator. [25] Undulators have photon flux of $N_p = N_e N^2$, where N_e is the number of electrons and N is the number of periods. [26] Wigglers use higher magnetic fields of several Tesla to produce a wider emission cone ($\theta \gg 1/\gamma$) with broad spectral bandwidth composed of densely spaced spectra lines that closely resembles bending magnet emission, and higher photon flux that is N times the number of electrons, and higher than bending magnets. [28] [26] These synchrotron, undulator, and wiggler sources are excellent sources for metrology for EUV light. However, they are very large from 0.1 to 1 km in diameter, which require large facilities that cover several acers. They are also very expensive to operate due many megawatts of power they consume. For this reason, there are only about 46 synchrotron facilities in the world, and only 7 within the US. They are very impractical to use for EUV or VUV sources in lithography. These facilities are used in almost every EUV industry to make calibrated measurements of optics, detectors, and spectrometers.

EUV lasers and high harmonic generation (HHG) provide spatially coherent sources of light. EUV lasers recently have experienced rapid development. EUV lasers use a cylindrical shaped, hot dense plasma as a gain media. They can provide a narrow spectral bandwidth on the order of 10^{-3} nm, which can be 0.1% of the bandwidth of synchrotrons. [29] These lasers are produced with either a discharge produced plasma (DPP) or a laser produced plasma (LPP). In

DPP EUV lasers, an electric discharge across a capillary filled with a gas creates a hot dense plasma. [30] The formed plasma is then excited by a second large electric pulse that increases the plasma temperature to optimal range, at which point a coherent EUV pulse up to a microjoule is generated. [31] For higher energy laser produced plasmas are required. The gain medium in these lasers is created by irradiating a planar target with a hundred Joule level picosecond laser to form a hot dense plasma. The plasma is then irradiated with a second tens of picoseconds laser pulse to create electron collisions with the Ni like ions exciting elections to the 4d level, as seen in the level diagram in Figure 1.4. The electrons then decay to the 4p level with simulated emission and the electron then experiences a fast radiative decay to the ground state. This fast radiative decay allows for the formation of a population inversion. These lasers have demonstrated pulse energies as high as 1.5 μJ with 1-5 ps pulse durations, at conversion efficiencies of 10^{-6}. [32] [29] The spatial coherence of the output of these lasers is on the order of 10 mrad. [29] However, the repetition rates of these laser range from a few pulses per day to 10 Hz. These sources can be seeded by external coherent sources such as HHG for improved coherence.

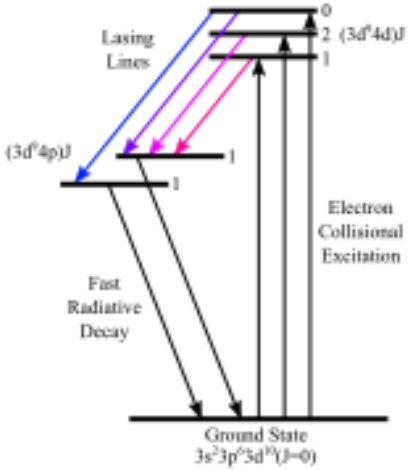

Figure 1.4: Simplified energy level diagram of a Ni-like EUV laser [29]

HHG EUV sources, like EUV lasers, provide highly spatially coherent and spectral coherent EUV light; however, they provide tunable wavelengths across the whole EUV band. Additionally, HHG EUV sources laser sources provide ultrafast pulse widths, at repetition rates on the order of 10 kHz. These up-converted lasers produce EUV light by irradiating a noble gas plasma with an infrared ultrafast high intensity laser pulse. The laser pulse is converted to higher harmonics when the high intensity electric field of the laser pulse causes an electron to tunnel into the vacuum level of the atom and is accelerated back to the parent atom. This emits Bremsstrahlung like radiation. When the laser pulse phase matching is achieved with the phase of the emitted light, efficient conversion of the laser pulse into higher harmonics is achieved. The conversion efficiency of these sources are on the order of 10^{-5}, which is an order of magnitude better than EUV lasers. HHG sources typically produce no more than a few microjoule of pulse energy at long EUV wavelengths, and a few hundred picojoules at shorter wavelengths. [33]

Both EUV lasers and HHG EUV sources provide both spatially and spectrally coherent EUV light. These systems are very compact to compared synchrotron sources, and often fit on a table top. The pulses these sources provide range from a few microjoules to hundreds of nanojoules. An advantage of HHG EUV sources is their kHz repetition rates and wavelength tunability, making them ideal for small scale metrology and imaging in a research environment. Conversion efficiencies ranging from 10^{-5} – 10^{-6} and highest average powers on the order of 10^{-2} mW, rule out these sources in applications like lithography. However, they are used extensively in microscopy for imaging nanoscale objects.

1.1.1.2 Incoherent EUV Sources

Discharge produce plasmas (DPP) and laser produced plasmas (LPP) are the two main types of incoherent sources that produce EUV light. These sources rely on plasma temperatures in the several tens of eV, and emit incoherent light across infrared through EUV into large solid angles. Most discharge gas plasmas rely on pinched plasmas, which temporarily increases the plasmas temperature and density. However, the plasma quickly collapses due to heat transfer and hydrodynamic instabilities. These sources have produced an average power as high as 50W in 2π sr in the 13.5 nm EUVL band, with conversion efficiencies of 0.75%. [34] There are several varieties of DPP sources including the above discussed capillary discharge, hollow cathode triggered gas discharge, [35] and Z-pinch gas discharge. [34]

High power LPP EUV sources have steadily increased in output power to over 250 Watts. [36] Due to the high power and conversion efficiency, as compared to DPP source, LPP sources have been selected for HVM EUVL. As seen in Figure 1.5, these sources use a high power laser to vaporize planar or droplet targets, in close proximity to a large collection optic which focuses the light to an intermediate focus. The plasma formed from these plasmas emit infrared to EUV radiation into 4π sr. Due to this, narrow band (2% at 13.5 nm) collector mirrors and filters are necessary to remove out-of-band emission. Several commercial high power sources use a 10 μm wavelength source laser to irradiate liquid Tin (Sn) droplets, to produce 13.5 nm light for the EUVL. [37] [38] These sources have reported as high as 4.7% conversion efficiency from laser power to EUV power in a 2% bandwidth at 13.5 nm in 2π sr. [38] An advantage of droplet target sources is that the target material is refreshable, allowing continuous run times measured in days. Light collected to the intermediate focus for in-band wavelengths

are often measured in hundreds of Watts. [36] [39] [37] [38] A disadvantage of these sources is their production of tin target debris, requiring debris mitigation to protect the collection optics. [40] [41] The source discussed in this thesis uses 1 μm wavelength laser to irradiate mass limited tin (Sn) solution liquid droplets. It has several key advantages over pure Sn droplet sources, with the most significant being low emitted target debris. [42]

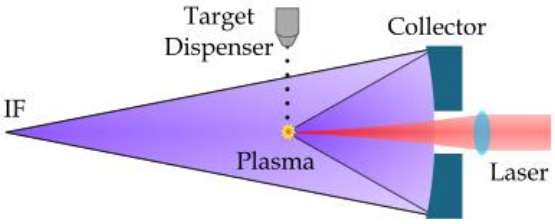

Figure 1.5: EUV laser plasma source

The development of new EUV sources have in many cases created opportunities for applications. EUV imaging systems have long been used by satellites to study solar phenomenon. [43] With the development of laboratory sources, new application for EUV light became apparent. It has also been used for microscopy extensively for EUV mask inspection for defects and for biological microscopy. [44] [45] [46] The short wavelength of EUV light allows for optical penetration of dense plasma. Coherent EUV sources are also used for time resolved interferometry of these plasmas. [47] Furthermore, these sources are used for ultrafast spectroscopy. [48] In the last decade the development of EUV applications, for high volume manufacturing of semiconductors, have greatly expanded due to the new field of Extreme Ultraviolet Lithography (EUVL). EUVL is critical to the development of the next generation of semiconductor chip manufacture. [42] [15]

1.1.2 EUV Lithography

Extreme Ultraviolet Lithography (EUVL) is the next generation lithography patterning architecture that uses 13.5 nm wavelength light for high volume manufacturing (HVM) in the semiconductor industry. 52 years ago "Moore's Law" was proposed by Gordon Moore of Intel, [49] and later revised, [50] stating that the number of transistors on a microprocessor will double every two years. The lithographic techniques used to manufacture chips have advanced over the years to keep pace with this law as seen in Figure 1.6. The number of transistors on a single chip processor now exceeds 7 billion, while maintaining the cost of the microchip. The reason for this is that the minimum feature size has continued to decrease allowing more transistors to fit on the chip.

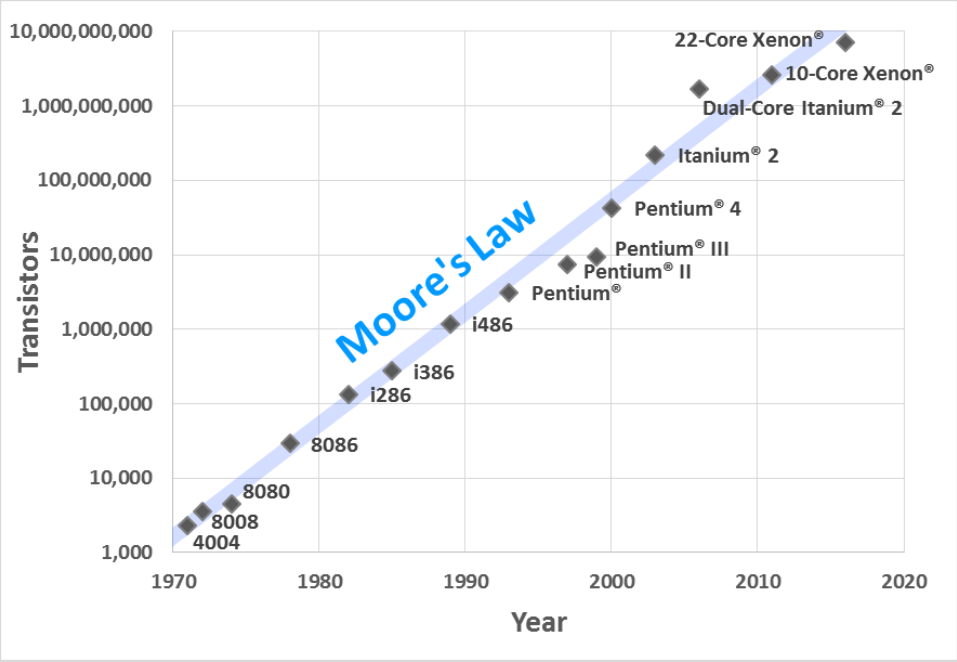

Figure 1.6: Moore's law in transistors vs. year, for Intel processors [51] [52] [53] [54]

With lithography, the minimum feature size is defined by a modified form of the Rayleigh resolution criterion formula as, [16]

$$d_{MFS} = k_1 \frac{\lambda}{NA} \qquad (1.2)$$

where k_1 is a constant determined by several factors from the lithographic technique, NA is the numerical aperture of the illumination optics, and λ is the wavelength. The semiconductor industry has already decreased k_1 near to the physical limits of 193 nm wavelength lithography tools, as well as increased the NA of the projection optics to as high as 1.35. To make smaller feature sizes than is typical of 193 nm, lithography for HVM is using a technique commonly called "multi patterning". [55] [8] In this process a structure on the wafer is made by exposing and etching a pattern into the wafer, a new resist is applied and the wafer is exposed and etched again to produce features smaller than possible with the first exposure. However, this process duplicates the steps necessary to make a device which ultimately makes the cost of semiconductor device manufacture increase. Currently, 8 step multi-patterning is being employed in HVM to perform lithography intended for EUVL. [8] Figure 1.7 shows specifications in k_1 factor vs numerical aperture and resolution, for ASML production lithography tools. [37] [56] [57] [58] [59] [60] It shows that for each wavelength there is a gain in resolution. Also, the resolution decreases as the tools increase NA and the k_1 factor. By using a wavelength of 13.5 nm, EUVL brings the potential minimum feature size an order of magnitude smaller using Equation (1.2). This will extend the life of silicon lithography and relax the requirements on k_1 and NA as seen in Figure 1.7.

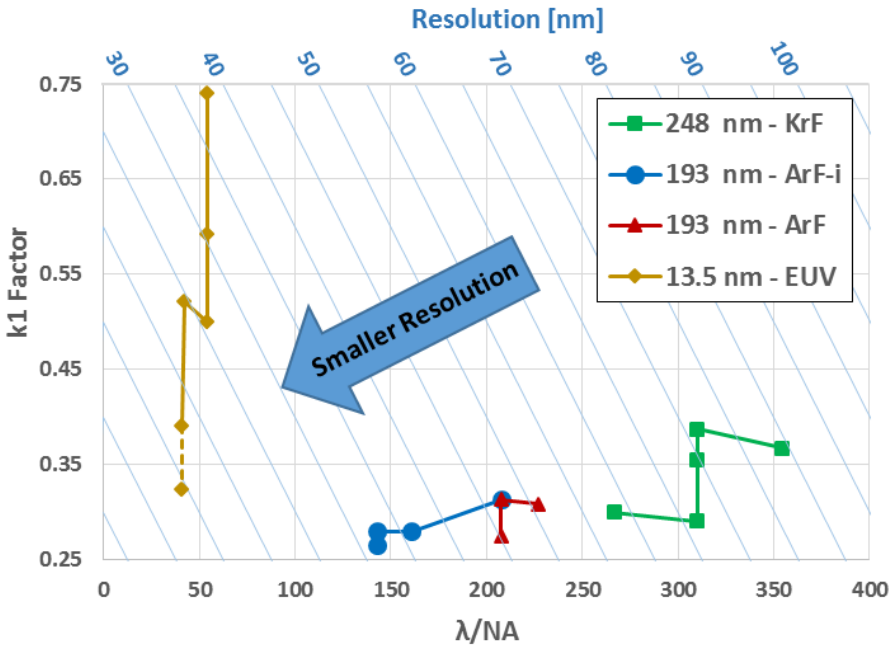

Figure 1.7: ASML 248, 193, and 13.5 nm lithography tool specifications in k_1 Factor vs. λ/NA and resolution [37] [56] [57] [58] [59] [60]

There are many technological challenges that are limiting immediate adoption of EUVL for HVM. In conventional lithography techniques EUV light is generated by a source, and is collected with collection optics. The light is then transferred to a reticle through illumination optics and the reflected image is then reduced to the photoresist with the projection optics. EUV optics however, are all reflective multi-layer mirrors that have narrow bandwidth with a peak reflectivity of 69.6 %. [61] In order to collect light from the intermediate focus and illuminate the reticle, current EUV sources use 4 mirrors, which is then projected onto the wafer for patterning with 6 additional mirrors. [62] With 11 mirrors at a best case reflectivity shown above, the total system transmission is 1.6 %. These significant losses through the optics require higher source power to illuminate the photoresist. Additionally, Current photoresists have lower than anticipated sensitivity of 5 – 30 mJ/cm^2, [63] with current prototype systems needing a range of 30 – 50 mJ/cm^2. [64] As a consequence, more light from the EUV source is required for proper

exposure. The current production level EUV lithography tool provides 125W of usable EUV light. [39] However, greater than 180W is required for full production level. [15] With lower source power the exposure time of the photo resist increase directly, which lowers wafer throughput and cost effectiveness. Until major technical improvements are made to EUV sources, EUVL will not be adopted to full production level. With the full implementation of EUV lithography delayed, pace of Moore's Law has slowed to doubling every 2.5 years. [65]

1.1.3 Optics for EUV

Optics for short wavelengths, such as EUV light, require special considerations due to the high absorption of EUV light in most materials. Here, the refractive index as function of frequency is represented in the general form as,

$$n(\omega) = 1 - \delta(\omega) + i\beta(\omega) \tag{1.3}$$

where $\delta(\omega)$ is the refractive index decay, and $\beta(\omega)$ is the extinction coefficient. [16] These terms are derived from the atomic scattering factor,

$$f = f_1 - if_2 \tag{1.4}$$

where f_1 is related to the phase velocity variation, and f_2 relates to the decay of the amplitude due to absorption and,

$$\delta(\omega) = \frac{n_a r_e \lambda^2}{2\pi} f_1(\omega), \quad and \quad \beta(\omega) = \frac{n_a r_e \lambda^2}{2\pi} f_2(\omega)$$

(1.5)

where n_a is the average density of atoms in the material, r_e is the classical electron radius, λ is the vacuum wavelength. [16] There are many methods determining these optical constants, which are further discussed in. [66] The listed values for f_1 and f_2 of most elements with the atomic number of 1 – 92 can be found in. [67] Based on these values the absorption length or skin depth can be determined by,

$$l_{abs} = \frac{\lambda}{4\pi\beta} \tag{1.6}$$

EUV light's high absorption in all materials, prevents the use of thick optical elements such as conventional lenses used in the UV through IR region. As a result, the recourse is to use several types of reflective, and more recently diffraction-based optics. For normal incidence reflection from a material surface from light propagating in free space, the reflectivity is defined by,

$$R = \frac{|1 - n_t|^2}{|1 + n_t|^2} \tag{1.7}$$

where n_t is the refractive index of the material. At short wavelengths of EUV light, $\delta \ll 1$ and $\beta \ll 1$, and therefore, [68]

$$R \simeq \frac{\delta^2 + \beta^2}{4} \tag{1.8}$$

With EUV light, the reflectivity is on the order of 10^{-5} which renders normal incidents single layer mirrors ineffective. However, using Snell's law, the critical angle for total external reflection for EUV light is found to be $\theta_c = \sqrt{2\delta}$. [16] At grazing incidence, reflectivity is high for single layer mirrors. Reflectivity spectra for common materials are found in. [66] Several imaging systems use glancing incidence optics, such as the Kirkpatrik-Baez mirror system, and Wolter imaging systems. [69] [70]

Multi-layer mirrors (MLM) provide the highest reflectivity, at normal incidence. These mirrors rely on two alternating layers of high and low atomic number (Z) material, as seen in Figure 1.8. Each layer pair scatters incident light, which constructively interfere under the Bragg's law corrected for refraction given as,

$$m\lambda = 2d \sin\theta_i \sqrt{1 - \frac{4\delta d^2}{m^2\lambda^2}} \qquad (1.9)$$

where m is the diffraction order, d is the layer pair spacing, θ_i is the incident angle, δ is the bilayer weighted real part of the refractive index. [16] The low Z material acts as a spacer with the lowest refractive index possible ($n_l = 1 - \delta_{low\,Z} + i\beta_{low\,Z}$). While the high Z material ($n_h = 1 - \delta_{high\,Z} + i\beta_{high\,Z}$) provides scattering, while minimizing absorption.

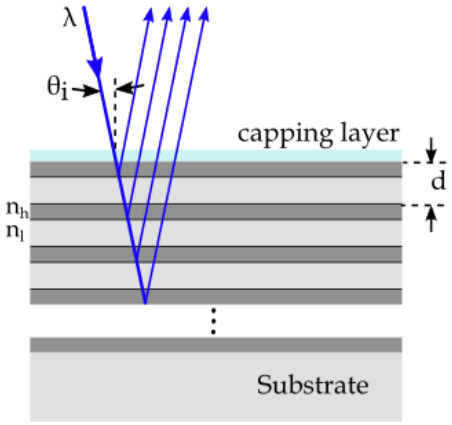

Figure 1.8: Multilayer mirror showing scattered light from Bragg condition

For EUV light, these layers are typically less than 10 nanometers thick. In addition to the Bragg condition, the ratio of the high Z material to the low Z material thickness defined as,

$$\Gamma = \frac{t_h}{d} \tag{1.10}$$

where $d = t_h + t_l$ is the layer pair thickness, t_h is the e Z material thickness, and t_l is the low Z material thickness. The optimal value Γ at normal incidence is determined by solving,

$$\tan(\pi\Gamma_{opt}) = \pi\left(\Gamma_{opt} + \frac{\beta_{low}}{\beta_{high} - \beta_{low}}\right) \tag{1.11}$$

where Γ_{opt} is the optimal value of Γ, β_{low} is the absorption components for the index of refraction for the low Z material, and β_{high} is for the high Z material. [16] Mirrors for EUV light have achieved near theoretical reflectivity of 68.8 % with a bandwidth centered at 13.5 nm using ~100 layer pairs of Molybdenum (Mo) and Silicon (Si) coatings. [61] [71] A significant issue with these mirrors, is that the mirror layers

interdiffuse into each other over time. A thin carbon layer is sometimes added between each layer to reduce this as seen in Figure 1.9. [61]

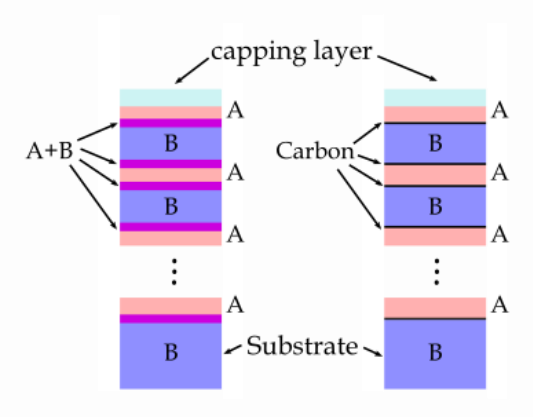

Figure 1.9: Multilayer mirror interlayer diffusion (A+B) of layer A and B (left), and an interlayer carbon barrier (right)

1.2 VUV Radiation

The Vacuum Ultraviolet (VUV) region is a band of light in the wavelength range from 100 nm (13 eV) to 200 nm (6 eV). The VUV band derives its name and characteristics, by high absorption of its photons by air (Figure 1.10), mainly due to Oxygen, Water and CO_2. [72] [73] Typical systems involving VUV light require a vacuum environment or a gas purged environment to remove oxygen, and in some cases nitrogen. VUV light is ionizing radiation, where the photon energy is capable of stripping electrons from atoms, thereby causing molecular bonds to break in materials. This can degrade of optics and materials within a VUV system over time by changing their molecular structure.

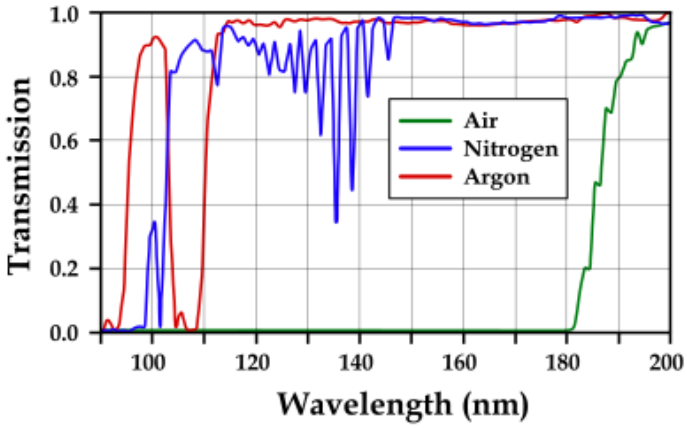

Figure 1.10: Transmission from 90 – 200 nm, through air, nitrogen, and argon at 1 ATM pressure [73]

Transmissive optics for VUV light are limited to a few materials such as, fused silica, calcium fluoride (CaF_2), magnesium fluoride (MgF_2), and lithium fluoride (LiF), as seen in Figure 1.11. Standard optical materials used in the visible wavelength region, such as fused silica and BK-7 possess little to no transmission in the VUV band. For wavelengths longer than 170 nm UV-fused silica and sapphire have good transmission. For shorter wavelengths CaF_2, MgF_2, and LiF offer good transmission with cutoff wavelengths at 130, 115, 105 nm, although with significantly higher expense. For wavelengths lower than 105nm, there are no transmissive optics. Here, reflective optics must be used.

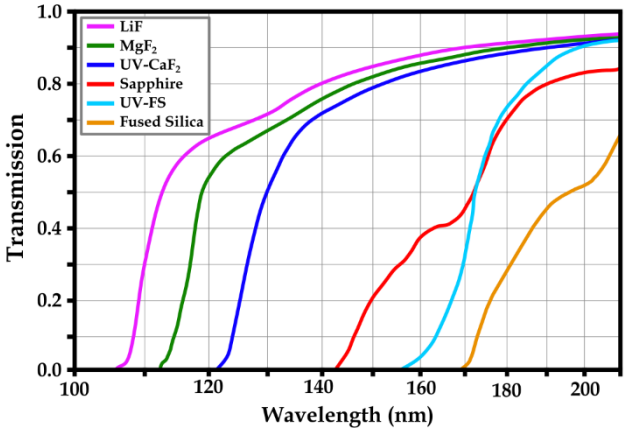

Figure 1.11: Transmission from 100 – 210 nm for common VUV optics (3 mm thick) [74]

1.2.1 Sources and Applications

There are a wide variety of sources in the VUV band, both coherent and incoherent, with many applications. One of the most common sources are excimer lasers. These lasers usually consist of a high pressure noble gas and or a halogen gas, which is exited with an electric discharge. The excited atoms form temporary molecules called excimers. These unstable molecules quickly break their temporary bond, emitting a VUV photon. [75] Excimer lasers provide pulses with the durations in the tens of nanoseconds with energies into the hundreds of millijoules. [76] Excimer lasers that emit in the VUV band are Ar^{2*}, Kr^{2*}, F^{2*}, Xe^{2*}, and ArF, with emission wavelengths of 126, 146, 157, 172 and 175, and 193 respectively. Of these, the most widely used is the ArF laser. Current commercially available systems provide 40 Watts, 11 mJ at 193 nm. [36] ArF lasers are used extensively as the source for exposing photoresist in semiconductor lithography. [7] [8] They are also widely used for corrective laser eye surgery. [13]

HHG sources, as discussed in Section 1.1.1.1 are also prevalent in the VUV band providing coherent harmonic generation of VUV light with ultrafast pulse widths in the low hundreds of femtoseconds. Typically, by reaching the 7^{th} or 9^{th} harmonic with corresponding

wavelengths of 149 nm and 116 nm, 0.5 mW of coherent VUV light can be produced at repetition rates of 10 MHz. [77] With pulse energies of hundreds of watts, HHG VUV sources do not produce enough peak power to surpass excimers lasers in applications such as micromachining or photolithography, they can be used for spectroscopy and microscopy due to their high brightness, and the higher resolution afforded by the short wavelengths.

For broadband VUV sources, one of the most common source is the deuterium (D2) arc lamp. This source is composed of a DC electric discharge through a pressurized deuterium gas. An aperture between the electrodes restricts the curt flow to a small volume creating a region of high intensity emission. D2 lamps have stable emission spectrum (Figure 1.12), with output fluctuations on the order of 0.005% (peak-peak). [78] They are available with output powers in the tens of watts, and as high as 30 watts. [78] In addition, at wavelengths longer than 175 nm, the D2 lamp has a flat continuum emission spectrum, as seen in Figure 1.12. Due to their stability, this flat spectrum at long wavelengths, and their compact size, these lamps are extensively used for calibration sources. Absolute calibration of the VUV metrology equipment in this thesis was performed with a calibrated deuterium lamp.

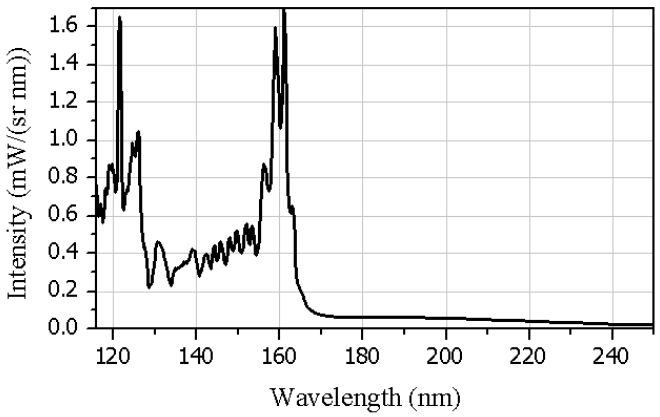

Figure 1.12: Measured Hamamatsu L9841 deuterium lamp spectrum

For many applications such as machining, VUV lithography, and microscopy, high brightness sources are required, with average powers greater than 100 watts. For this reason, many of the sources such as HHG, and D2 lamps are unsuitable. Excimers sources can provide hundreds of watts necessary for these applications; however, they are monochromatic and are not wavelength tunable. Laser plasma sources provide an ideal high power broadband tunable VUV source. These hot dense plasmas are formed when a laser heats a target material. The excited ions in the plasma emit photons in the VUV band as they relax to lower energies. The extent of the plasma is limited by the focal size of the laser which is on the order ten to several hundred microns. This small spot size allows for high radiance, which allows for efficient optical collection. Hundreds of watts of light can be collected from these plasma approaching kilowatt powers. [79] [80] These sources can provide high conversion efficiencies greater than 10%, and high average powers at hundreds of watts. [81] [82] [83]

VUV light has many applications both in scientific and commercial industries. One of these applications is spectroscopy, where materials are excited with VUV light causing secondary photon emission having spectral signatures depending on the properties of the material. The spectrum of the emitted light can be used to determine the molecular state, or chemical composition of the material. [84] [11] In addition to its uses in spectroscopy, the short wavelengths of VUV light have absorption depths in materials on the order of nanometers. This is a key advantage for surface micromachining and is used extensively for corrective eye surgery. [13] Also, it is used for micromachining silicon in the semiconductor industry. [6] [5] Currently the semiconductor industry uses wavelengths in the VUV band at 356 and 193 nm for

photolithography. [7] [8] [9] These short wavelength allows for resolutions down to 30 nm, and production of small feature sizes down to 6 nanometers to enable reduction in the size of computer transistors. Another application for VUV light is microscopy. The shorter wavelength of the VUV light allows for 2-6 times smaller resolution than UV or visible light, which allows4 imaging of features less than 100 nm. [14] In addition, microscopy of masks and wafers at VUV wavelengths are necessary to detect defects in manufacturing of a few nanometers in scale. [10] [6]

1.2.2 VUV Metrology

For metrology of physical structures on the nanometer scale, direct imaging can provide the most information. In order to fully resolve an object, the resolution of the system must be smaller than the smallest feature of interest. The resolution of an imaging system is limited by the Rayleigh criterion defined by, [85]

$$R = 0.61\frac{\lambda}{NA} \tag{1.12}$$

where $NA = n\sin\theta$ is the numerical aperture of the optical system, n is the refractive index of the of the material between the imaging system an d the object, θ is the half-angle, and λ is the wavelength. Here, a larger NA, or shorter wavelength results in resolution of smaller feature sizes. With free space optics typical numerical apertures are limited to NA=1 [86] due to physical constraints of the optics. However, when using higher index matching fluids between the objective and the object, numerical apertures as high as NA=1.7 are possible [86] yielding a

59 % reduction in resolution over free space. Lithography using 193 nm light has used this technique in immersion lithography, to increase resolution. [87] With this limiting factor, shorter wavelengths are required to resolve smaller features. For this reason, imaging in the shorter VUV wavelength region is often required. As discussed in Section 1.2.1, many applications involving imaging benefit from the smaller resolution, such as high volume semiconductor manufacturing, microscopy, nanoscale material processing. Therefore, developing new sources of VUV light will greatly benefit these industries.

In order to image an object, it must be effectively illuminated so that sufficient reflected, scattered, or refracted light is captured by the imaging system to provide enough radiant flux to the detector area. If the detected signal from the object has a low intensity, then the dynamic range of the captured image is reduced, which reduces the ability to resolve small features due to low contrast. An important consideration of illumination sources is radiance and etendue. Radiance is defined as the radiant flux emitted from or transmitted through a surface per unit solid angle per unit area. [88] Etendue is defined as the product of the area of the light source and the solid angle of the imaging system entrance pupil subtends as seen from the source. [85] Optical radiance is conserved in a non-absorbing optical system. Therefore, in order to illuminate an object with the same radiant flux, sources with a larger etendue, will require a higher NA collection optic, or a source with a higher radiant flux per solid angle than with a small source etendue. For metrology purposes, a source with a high radiance is preferable. It allows small NA optics to capture higher source power, and provides higher intensity in the illuminated area. For this reason, high radiance sources are required to meet metrology demands. Laser plasma sources are able provide compact high radiance sources.

1.3 Overview of Thesis

The work in this thesis, presents two experimental plasma sources within the XUV wavelength range, using several target materials. The High Power EUV Source Facility (HP-EUV-Facility) was developed for demonstrating a tin based, mass limited droplet, laser produced plasma source. The EUV spectrum in this facility is measured across a spectral range of 10.5 – 18 nm. Additionally, absolute energy measurements for the 13.5 +/- 2% (in-band) region, critical to EUV lithography sources for HVM semiconductor manufacture, were acquired.

The VUV Metrology Source Facility (VUV-MS-Facility) was constructed and developed for investigating broadband (22 – 250 nm) emission of VUV sources presented in this work. VUV sources using planar and gas jet targets were investigated. Gas jet plasmas included argon, krypton, and xenon. For planar targets investigated materials where magnesium, aluminum, silicon, copper, zinc, molybdenum, indium, tin, and tantalum. The laser plasmas produced were investigated using a number of spectrometers and an at wavelength spectrometer. The spectrometers captured spectrum covering wavelength range of 22 – 124, 115 – 170, and 140 – 250 nm. These spectrometers were absolutely calibrated for this work. Also, at wavelength imaging of these plasmas were performed to estimate plasma size.

The thesis is organized into several chapters. First the general physics of laser produce plasma is presented in CHAPTER 2. This section discusses laser light absorption, plasma emission, and hydrodynamic simulations of laser plasmas. The next chapter (CHAPTER 3) discusses several different laser plasma target geometries. It describes considerations such as laser alignment, target stability, and environmental conditions when using these different geometries. Additionally, the general physics governing these target geometries are also

discussed. CHAPTER 4 describes the different metrology devices used in the experimental studies presented in this thesis. The design and optical parameters of the spectrometers are presented, as well as the technique for their calibration. Also described is the optical design and calibration of an EUV energy meter. An imaging system used to capture at wavelength plasma images in the VUV band is also described. After this section the HP-EUV-Facility is thoroughly discussed. This chapter (CHAPTER 5) describes the design and construction of this facility as well as each of its integrated subsystems. It also describes metrological conditions, calibration, and presents emission spectra for liquid droplet targets. CHAPTER 6 discusses the VUV-MS-Facility in depth, including its necessary subsystems. It then presents the apparatus for gas jet targets and the experimental conditions for various targets, their absolute calibrated emission spectra, and the calculated conversion efficiency. This chapter then describes the target apparatus for planar targets, the absolute calibrated emission spectra for various targets, and their calculated conversion efficiency. Also presented, are wavelength imaging of selected targets. The final chapter (CHAPTER 7) of this thesis is the conclusion.

CHAPTER 2: LASER PRODUCED PLASMA PHYSICS

Due to plasma having properties dissimilar to solids, liquids, and gases, it is considered to be a fourth state of matter. A plasma is a system of ions and electrons, having a total neutral charge, which are coupled to each other via their self-consistent electric and magnetic fields. [89] With the invention of the laser, experimental and theoretical work regarding laser-plasma interactions quickly formed as a major field within plasma physics. Understanding the processes of laser absorption and the radiation emission of these plasmas are critical to physical understanding of plasma and its numerous applications. Laser produced plasma sources involving hot dense plasmas, are presented in this thesis. This section will present the necessary physics behind laser produced plasmas. It will start with the general conditions for laser light absorption, and the dominate process of absorption through inverse bremsstrahlung absorption (IBA). It is followed by a presentation of the radiation emission processes. This section finishes with an outline of the hydrodynamic code used to simulate the plasmas in this thesis.

2.1 Laser Light Absorption

There are many processes for the absorption of short wavelength laser light into a material; a few which are relevant to this work are photo-ionization, optical breakdown, and inverse bremsstrahlung. For materials irradiated with light with photon energies near 1 eV (1 μm) there is insufficient energy in a photon for direct ionization due to the higher ionization potential of the atoms. While individual photons can trigger the emission of electrons through the photoelectric effect, it is insufficient to generate a laser plasma. At laser radiation intensities typically greater than 10^8 W/cm^2, the electric field in the EM radiation is high enough to cause

optical breakdown of the target material. Above this intensity multi-photon ionization is initiated, creating free electrons. A hot plasma conversion layer, known as the corona, is formed on the surface of the target. The initial ionization occurs significantly faster than the typical pulse duration of the laser, allowing for the laser beam to couple to the corona. The resulting electron avalanche causes electrons to experience high accelerations, allowing collisions with ions in the plasma to release new electrons. In turn these new electrons experience the same process resulting in a growth in the plasmas electron density and temperature of the plasma, forming a charge neutral mix of electrons and ions. It is at this point in plasma formation, that most theoretical modeling of laser-plasmas begins.

As seen in the cartoon schematic Figure 2.1, the hot dense plasma formed at the surface of a target is confined to a small volume, and rapidly expands perpendicular to this surface. As it expands, it continues to absorb laser radiation until its plasma frequency reaches the critical density. At this point the laser radiation experiences total internal reflection (TIR).

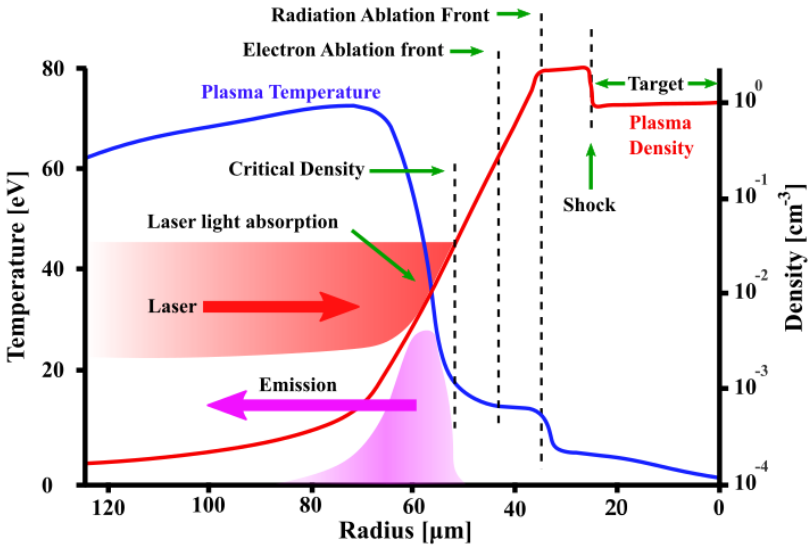

Figure 2.1: Cartoon of laser interaction with target surface leading to light emission

Near the critical density the large amplitude of the electromagnetic field, and the relatively high electron density, the highest absorption of laser energy occurs. This absorption region is where most of the X-ray, through VUV radiation, is produced. Target material past the critical density region is not directly ablated by laser light absorption, yet it is by the conduction of energy from the absorption region. [90] For the laser plasmas presented in this work, full laser absorption occurs before critical density is reached. These processes are thoroughly described in many texts including [89], [16] [91] [92] [93] [94] [95], and [42].

2.1.1 Critical Density

Laser light will propagate through a plasma until it reaches a region of critical electron density. The propagation of the laser light wave in the presence of free electrons in the plasma follow the dispersion relation,

$$\omega_L^2 = \omega_P^2 + k_L^2 c^2 \qquad (2.1)$$

where ω_L, and k_L is the angular frequency and wave number $(2\pi/\lambda)$ of the light respectively. The plasma frequency ω_P, which is the natural oscillation of the electron in a plasma, is defined as,

$$\omega_P = \sqrt{\frac{n_e e^2}{\epsilon_0 m_e}} \qquad (2.2)$$

where n_e, is the electron density, e is the charge of an electron (1.6022 x 10^{-19} C), ϵ_0 is the permittivity of vacuum (8.854 x 10^{-12} F/m), and m_e is the mass of an electron (9.1094 x 10^{-31} kg). Using equations (2.1) and (2.2) the index of refraction can be extracted as,

$$n(n_e, \omega_L) = \sqrt{1 - \frac{\omega_P^2}{\omega_L^2}} = \sqrt{1 - \frac{n_e e^2}{\epsilon_0 m_e \omega_L^2}} \qquad (2.3)$$

As the light propagates toward higher plasma electron densities with higher plasma frequencies (ω_P), the plasma frequency approaches the value of the laser frequency (ω_L). This results in the index of refraction approaching zero and TIR of the laser light occurs. In this condition the critical density can be derived from (2.3) as,

$$n_{cr} = \frac{\epsilon_0 m_e \omega_L^2}{e^2} \qquad (2.4)$$

For the laser-plasmas discussed in this thesis, irradiated with 1 μm wavelength light, the critical density is approximately 10^{21} cm^{-3}. By reducing the wavelength of the laser used to generate a plasma, absorption of the laser light can occur over a larger volume of the target material. This allows production of short wavelength photons such as those in the EUV band in denser parts of the plasma.

2.1.2 Inverse Bremsstrahlung

There are many processes involving photons and ions that contribute to the heating of laser-plasmas. The most significant and efficient absorption process is inverse Bremsstrahlung absorption (IBA). Bremsstrahlung ("braking radiation") is produced when a charged electron is decelerated when it is deflected by Coulomb attraction of an ion. The typical example is the deceleration of an electron by an atomic nucleus or ion, with the electron moving to a lower energy unbound state. This process can be defined as,

$$e^{-}(E) + ion \rightarrow e^{-}(E') + \hbar\omega + ion \quad (2.5)$$

where e^{-} is the electron, E is the energy of the electron, E' is the energy of the electron after the interaction, and $\hbar\omega$ is the energy of the emitted photon which is equivalent to $E' - E$.

Inverse Bremsstrahlung absorption (IBA), in the inverse process where photon is absorbed in the presence of an ion and an electron (Figure 2.2),

$$e^{-}(E) + \hbar\omega + ion \rightarrow e^{-}(E') + ion \quad (2.6)$$

where $\hbar\omega = E - E'$ is the absorbed photon energy.

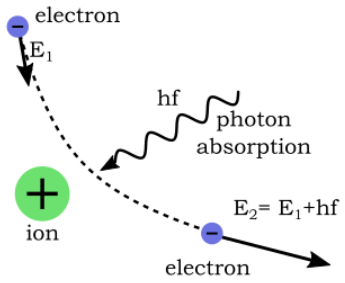

Figure 2.2: Photon absorption by inverse Bremsstrahlung absorption

In this process, electrons gain energy from the laser photons, accelerating them into collisions with ions in the plasma releasing more electrons. The collisions play a central role in heating the plasma, by creating more disorder in the plasma allowing for increased electron energy. The absorption coefficient for IBA is related to the intensity of the laser relation by, [92]

$$k_{IB} = 3.10 \times 10^{-7} \cdot \ln\Lambda \cdot \frac{Zn_e^2}{T_e^{3/2}} \cdot \frac{1}{\omega_L^2 \sqrt{1 - \left(\frac{\omega_p}{\omega_L}\right)^2}} \quad (2.7)$$

$$\ln\Lambda = \ln\left[\frac{3k_B T_e 4\pi\epsilon_0}{Ze^2}\sqrt{\frac{k_B T_e \epsilon_0}{e^2 n_e}}\right] \quad (2.8)$$

where $\ln\Lambda$ is the Coulomb logarithm (Equation (2.8)), Z is the ionization stated of the ions, n_e is the electron density, T_e is the electron temperature, ω_p is the plasma frequency, and ω_L is the angular frequency of the absorbed laser photon. The parameter Λ is related to the ratio of the maximum and minimum impact parameters. [92] The maximum impact parameter is the Debye length, beyond which charges are shielded by the presence of other mobile charges. The

minimum impact parameter is the distance of electron's closest approach to an ion. From Equation (2.7) the absorption is strongest for high electron densities and at low electron temperatures. The absorbed laser energy after traveling distance L is given as,

$$\alpha_{abs} = 1 - exp(-k_{ib} \cdot L) \qquad (2.9)$$

Here, L is the plasma scale length which is related to the plasma's expansion velocity and laser pulse duration. [89]

To determine if IBA dominates a laser-plasma, the specific intensity at which IBA is significantly diminished is defined as, [89]

$$I^* = 10^{12} \cdot \frac{Z L_\mu f}{\lambda^4} \qquad (2.10)$$

where Z is the ion charge state, L_μ is the plasma scale length in μm, f is the flux limit, and λ is the laser wavelength in μm. The above equation assumes that the plasma is an underdense plasma where the electron density is less than the critical density, and the plasma is isothermal. For conditions, where $I \gg I^*$, the plasma is less collisional and the energy absorbed from the incident laser light is defined as $\alpha_{abs} = \sqrt{I^*/I}$.

2.2 Plasma Emission

Equilibrium requirements are seldom met within a laser-plasma. As the thermal energy of the plasma increases then several electronic processes that define its emission spectrum are

present. These processes are classified in three categories: bound-bound, free-free, and free-bound. Bound-bound radiation gives rise to narrow line emission. Bound-bound radiation, and free-bound radiation, also known as Bremsstrahlung radiation, and recombination radiation, are predominantly responsible for the broad continuum emission.

2.2.1 Line Emission

Line emission arises from so called bound-bound transitions. It is an electronic transition from one discreet energy level to another within an ion. When an electron moves from one discreet energy level to a lower level, a photon of a specific wavelength is emitted (Figure 2.3) giving rise to an emission line with a bandwidth on the order of 10^{-8} eV.

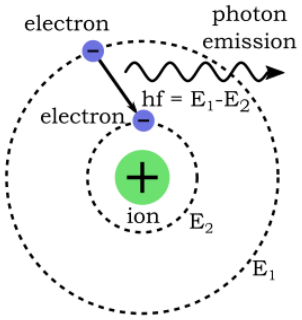

Figure 2.3: Bound-Bound electron transition photon emission

Bound-Bound transitions come from transitions between excited states, or resonance transitions, with the strongest effect from the latter. The emission rate for spectral line emission is defined by, [94]

$$P_{\zeta m' \to \zeta m} = \hbar\omega_{\zeta m' \to \zeta m} N_{im'} A(\zeta m' \to \zeta m) \quad (2.11)$$

where $\hbar\omega_{\zeta m' \to \zeta m}$ is the energy of the emitted photon, $N_{im'} A(\zeta m' \to \zeta m)$ is the number of transitions from the upper to the lower state per second per cubic centimeter. Interaction and motion of the liberated electron with other electrons and ions, will affect the plasma spectral shape, such as line broadening. In the case of high Z plasmas, there is a higher availability of electrons and possible bound transitions. Therefore, many more emission lines can exist in a narrow wavelength region. In addition, their line emission spacing can become smaller than the line width, causing overlapping line emission. Due to the high number and density of emission lines from these plasmas, determining the wavelengths of specific line transitions is difficult. In this case, the line emission as a group is called an unresolved transition array (UTA). [95] [96]

2.2.2 Continuum Emission

Continuum emission from laser-plasmas is predominantly formed from free-free, and free-bound transitions defined in detail below. This emission, forms a low continuous spectral emission separate from line emission. If the plasma is assumed to be in thermal equilibrium, the radiation emitted can be approximated as blackbody. Planck's blackbody radiation law gives the spectral distribution as,

$$I_B = \frac{2\pi hc^2}{\lambda^5 (e^{hc/\lambda k_B T} - 1)} \quad (2.12)$$

where h is Planck's constant, c is the speed of light, $k_B T$ is the plasma temperature, and λ is the wavelength. However, laser plasmas are rarely in equilibrium conditions, and the emitted radiation is instead dominated by Bremsstrahlung and recombination radiation.

2.2.2.1 Bremsstrahlung Radiation

As a free electron moves through the electric field of an ion, it can lose some or all of its kinetic energy to photon emission (Figure 2.4) while remaining unbound to an ion. The free-free transition, so called because the electron remains unbound to an ion during the transition, is also called Bremsstrahlung radiation. The German word, Bremsstrahlung, comes from "bremse" meaning breaking, and "strahlung" meaning radiation.

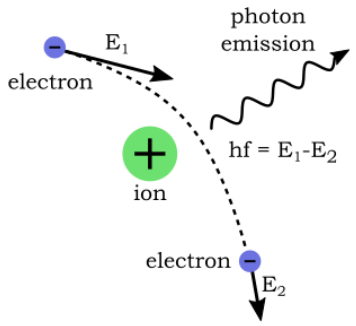

Figure 2.4: Free-Free electron transition resulting in Bremsstrahlung radiation

The collective radiation of many electrons within a plasma results in a continuum emission spectrum which is highly dependent on the electron density, ionic charge, and temperature. Taking into account the spectral intensity per wavelength, the spectral distribution is defined as, [92]

$$W_{ff}^{\lambda} = 2.0 \times 10^{-27} \frac{Z n_e^2 T_e^{1/2}}{\lambda^2} exp\left(-\frac{hc}{\lambda k_B T_e}\right) \quad (2.13)$$

where Z is the charge, n_e is the electron density, and $k_B T_e$ is the electron temperature. The emission profile is similar to blackbody radiation. However, the temperature for blackbody scales with T^4 where Bremsstrahlung scales with $T^{1/2}$. Peak wavelength of emission for Bremsstrahlung occurs at $\lambda_{max} = 250/T_e$ vs. $\lambda_{max} = 620/T_e$ for blackbody radiation. [92]

2.2.2.2 Recombination Radiation

The other main process contributing to continuum emission is free-bound emission, known as recombination radiation. In this process, a free unbound electron loses its kinetic energy and emits a photon (Figure 2.5), becoming bound to an ion.

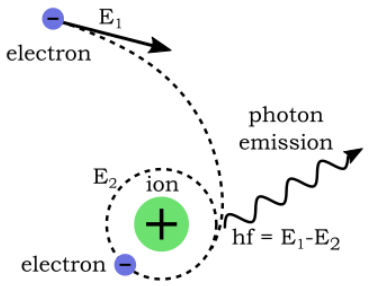

Figure 2.5: Free-Bound electron transition resulting in Bremsstrahlung radiation recombination radiation

The emission spectrum is shaped by the local kinetic energy distribution of the electron and the ionization potential energy, where the minimum photon energy is the ionization potential energy.

The spectral intensity of the continuum produced by recombination radiation is expressed in the ratio of the Bremsstrahlung continuum defined by, [92]

$$\frac{W_{fb}}{W_{ff}} = \frac{2Z^2 E_H}{k_B T_e} \sum_{n=1}^{\infty} \frac{1}{n^3} \approx 2.4 \frac{Z^2 E_H}{k_B T_e} \qquad (2.14)$$

where $E_H = 13.6eV$ is the hydrogen ionization energy. Plasmas with high temperatures and low charge will have higher Bremsstrahlung emission, which will overpower recombination emission.

2.2.3 Collisional Model

Radiation from a plasma depends on several physical processes, including atomic physics, collisional and radiative ionization, recombination, excitation, and de-excitation. These processes must be taken into account for many ionization stages and energy levels in order to determine the emission spectrum and the energy transport.

If the duration of the laser-produced plasma is significantly longer than the electron-ion relaxation time for the plasma, then a collisional-radiative equilibrium (CRE) model can be use. In the case of laser-plasmas the temperature and density of the plasma is high and the CRE model is the most effective model. [97] The model considers both radiative and collisional processes. The collisional ionization and excitation are balanced by radiative and three-body recombination. [98] However, there are several conditions that must be met. First the $\mathrm{Z}+1$ ion charge density during plasma evolution cannot change significantly while the ions of charge Z are reaching steady-state population distribution. Second, $k_B T_e$ must be greater than 10 eV.

Finally, due to its own radiation, the plasma must be optically thin. The CRE model has the form, for time dependent rates of population, [68]

$$\frac{dn(Z)}{dt} = n_e\left(-S(Z)n(Z) - \alpha_R(Z)n(Z) + S(Z-1)n(Z-1) + \alpha_R(Z+1)n(Z+1)\right) \quad (2.15)$$

where $S(Z)$ is the collisional ionization rate, $\alpha_R(Z) = \alpha_r(Z) + \beta_{3b}(Z)$ is the sum of radiative and three-body recombination rates, and n is the population. For two successive ionization stages in the plasma, the fractional ionic density of charge Z for the total ionic population in the plasma to be calculated by, [97]

$$\frac{n(Z+1)}{Z} = \frac{S(Z)}{\alpha_r(Z+1) + N_e\beta_{3b}(Z+1)} \quad (2.16)$$

An example of the CRE model shown in ion fraction distribution as a function of temperature is shown in Figure 2.6.

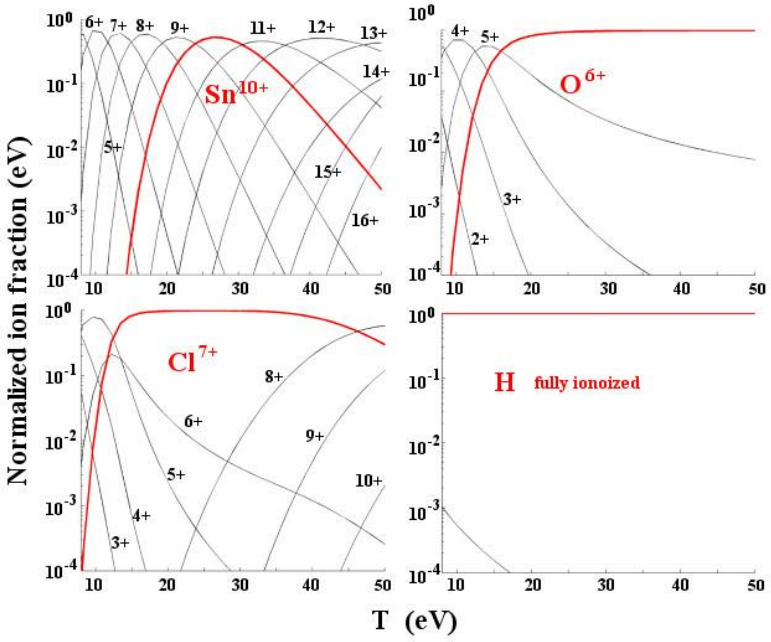

Figure 2.6: Calculation using CRE model for mass limited target components (tin, oxygen, chlorine, hydrogen) fractional ionic charge densities as a function of plasma temperature

By using well known atomic codes such as COWAN, HULLAC, and FAC to calculate atomic data and radiator strengths, and coupling this to the CRE fractional ionic charge densities, then emission spectra for each plasma temperature can be calculated. Applying these calculated spectra to the ion densities calculated by a hydrodynamic code like MED103 as discussed in Section 2.3, emission spectra can be predicted for different laser plasma conditions. Using this method, allows for predicting optimal plasma conditions to produce ideal charge states for produced desired emission spectra. [99] [100] [101] [102] [103]

2.3 Hydrodynamic Simulation

The properties of laser-plasma emission are determined by target and laser parameters. By modeling these conditions, optimal values for specific plasma emission can be determined. High density and high temperature plasmas, have rapid thermal expansion, steep density profiles,

and several non-linear processes. Describing the process mathematically is impractical to accomplish analytically. In order to predict and determine the optimal conditions for efficient radiation of a laser plasma source, a numerical solution can be used to approximate plasma expansion. The numerical solution treats the plasma as two fluids of electrons and ions. Within the Laser Plasma Laboratory, several simulation programs are used to simulate laser plasmas.

For hydrodynamic simulations at LPL, a one-dimensional, Lagrangian hydrodynamic code, called MED 103, is used to simulate the hydrodynamic expansion of the laser plasma. [101] [104] Med 103 was developed from an original MEDUSA fusion plasma code, designed for inertially confined fusion simulations of implosion and thermonuclear burn. [105] The code assumes that the target is uniformly irradiated and therefore emits isotopically. The plasma can then be reduced to one dimension for modeling. The plasma is divided into cells which have initial electron and ion densities, temperatures, average ion states, and many other parameters. It then calculates the energy balance transport from cell to cell for a time step, based on plasma coupling physics, electron and radiation transport. Then the resultant cell parameters, are determined and the process is repeated for a series of time steps in s self-consistent sequence. Med 103 considers the ions to have a perfect gas equation of state, with the electron density obtained by the Fermi-Dirac distribution.

Within Med 103 the plasma is described by the variables, ρ for density, u for velocity, T_i for ion temperature, and T_e for electron temperature. These variables are all functions of a space variable (r), and time (t). These parameters can be specified by the user for initial conditions, as well as chemical composition of the plasma by relative fractions of ionic species. The code uses a Lagrangian difference mesh with an integration scheme specific for hydrodynamics, and the heat conduction equations, which use the Crank-Nicholson scheme with the Gauss elimination

method. For each time step several iterations of the code are performed to account for non-linear dependence of the physical parameters on the temperature and density of each cell. [105]

The model implemented in MED103, as described in, [105] assumes a charge neutral mix of two fluids. These are an electron fluid with a density of n_e, and an ion fluid with a density of n_i. They are related by the average ion charge state Z in the flowing equation.

$$n_e = Zn_i \tag{2.17}$$

The mass density is defined by,

$$\rho = n_i M m_H = 1/V \tag{2.18}$$

where M is the average ion mass number, m_H is the proton mass, and V is the specific volume. Ions in laser plasmas are assumed to act as a perfect gas, where the electrons are described by an ideal gas or a Thomas-Fermi equation of state. To satisfy the charge neutrality of the plasma, the electron and ion fluids must have the same velocity, and the plasma motion can be described by the Navier-Stokes equation,

$$\rho \frac{du}{dt} = -\nabla p \tag{2.19}$$

where the velocity (u) is the motion of the Lagrangian coordinates $du/dt = u(r,t)$, and the hydrodynamics pressure p is defined as the sum of ion (p_i) and electron (p_e) pressure. Internal energies per unit of mass for each subsystem are defined by,

$$\mathrm{U} = \frac{\rho V}{\gamma - 1} \tag{2.20}$$

The energy equation that partitions the absorbed laser energy into thermodynamic and kinetic states is given by,

$$S = C_v \frac{dT}{dt} + B_T \frac{d\rho}{dt} + \mathrm{p} \frac{dV}{dt} \tag{2.21}$$

where T is the temperature, C_v is the specific heat per volume (Equation (2.22)), B_T is the variation of the internal energy of the subsystem due to particle interaction (Equation (2.23)), and S is the rate of input energy per mass.

$$C_v = \left(\frac{dU}{dT}\right)_\rho \tag{2.22}$$

$$B_T = \left(\frac{dU}{d\rho}\right)_T \tag{2.23}$$

Equation (2.25) and (2.24) define the terms for electrons and ions respectively, where the energy exchange rates arise from, the thermal conduction rate (H), electro-ion collisions (Q), thermonuclear energy release (K), viscous shock heating (Y), Bremsstrahlung emission (J), and inverse Bremsstrahlung absorption of the laser light (X).

$$S_e = H_e - K + Y_e + \mathrm{J} + X \tag{2.24}$$

$$S_i = H_i - K + Y_i + Q \tag{2.25}$$

The heat conduction term H, is defined by,

$$H = \frac{1}{\rho}\nabla \cdot \kappa \nabla T \tag{2.26}$$

where κ is the thermal conductivity and is defined for electrons and ions in Equation (2.27) and Equation (2.28) respectively, where Λ is the Coulomb Logarithm defined by Equation (2.29).

$$\kappa_e = 1.83 \times 10^{-10} \frac{T_i^{5/2Z}}{\log \Lambda} \frac{1}{Z^2} \tag{2.27}$$

$$\kappa_i = 4.3 \times 10^{-12} \frac{T_i^{5/2}}{M^{1/2} Z^2 \log \Lambda} \frac{1}{Z^2} \tag{2.28}$$

$$\Lambda = 1.24 \times 10^{6} \frac{T_e^{3/2}}{\mathrm{n}_e^{1/2} Z} \tag{2.29}$$

The absorption of laser light in Equation (2.24) is assumed to be dominated by inverse Bremsstrahlung when densities are below the critical density, and therefore model using the equations in Section 2.1.2.

Steep density and temperature gradients are characteristic of laser plasmas. Due to this, the electron heat flux which is defined by [105] as,

$$F_e = K_e \nabla T_e \tag{2.30}$$

where K_e is the Spitzer-Härm conductivity, is no longer valid because the Spitzer-Härm conductivity is only valid for low electron temperature gradients. To resolve this, a "free streaming limit" was included into the electron heat flux defined as,

$$F_{e,limit} = \left(\frac{1}{F_e} + \frac{1}{f v_e n_e k_B T_e}\right)^{-1} \quad (2.31)$$

where f which is less than one, is the flux limiting parameter adjusted by the user to match experimental results.

CHAPTER 3: LASER PRODUCED PLASMA SOURCE TARGET TYPE

There are many target types that can be considered for a laser produced plasma. These targets can be divided into three main groups: solid planar targets, liquid droplet targets, and gas jet targets. The following section will discuss the target types relevant to this thesis. First planar solid type targets will be discussed, including their characteristics and laser absorption, and the characteristics of the associated laser-plasmas. In addition, considerations for target motion and laser alignment will be discussed. Next, the characteristics of liquid droplet targets will be discussed. Furthermore, the fluid dynamic and stability considerations for providing a droplet target will be presented. The positioning technology necessary for providing repeatable targets will be discussed. Additionally, gas jet targets will be presented along with gas diffusion parameters, and physical properties of various gas targets. Lastly, the target environment considerations will be presented for this target geometry.

3.1 Planar Solid Target

The main advantages of solid targets are their high ion density and high opacity to the laser. The density of atomic solids ranges from $10^{21} – 10^{23}$ atoms/cm^3, and electron densities on the order of $10^{23} – 10^{24}$ e/cm^3. [106] With solid targets, several geometries can be used such as wire, foil, and bulk planar. Bulk planar targets typically have a surface volume ablated, while wire and foil targets can have the full thickness to be ablated by the laser across their full thickness. Because of this, laser irradiation can pass through the plasmas formed from wire or foil if the pulse width is longer than the plasma lifetime. With bulk planar targets the laser energy is confined to the surface of the target, and plasma emission is only radiated in a 2π sr solid

angle. As readily available collection optics have a collection solid angle of 2π sr or less, bulk planar targets can have a better collection efficiency. The distribution of the emission from the source can be approximated with Lambert's cosine law (Equation (3.1)), where I is the maximum luminous intensity normal to the surface, and I_o the luminous intensity at an angle θ from the normal of the surface. [85]

$$I_o = I\cos(\theta) \tag{3.1}$$

When a planar target is irradiated with a laser, the light is absorbed on the surface of the material by linear absorption, avalanche ionization, and photo-ionization. In the case of materials with high absorption, the linear absorption process dominates. [107] In this regime, the penetration depth of the laser can be determined using the Beer-Lambert Law,

$$z = -\frac{\ln\left(\frac{I_z}{I_0}\right)}{a} \tag{3.2}$$

where I_z is the intensity of laser light at depth z, I_0 is the initial laser intensity, and a is the attenuation coefficient. [108] The laser energy is absorbed into the electron subsystem of a solid at femtosecond time scales and in to the solids crystal lattice at nanosecond time scales. These two fluids can be described by two temperatures in the Two-Temperature Model of energy transfer [109]. Here they can be described as,

$$C_e\frac{\partial T_e}{\partial t} = -\frac{\partial Q(z)}{\partial z} - \gamma(T_e - T_i) + S$$

$$C_i \frac{\partial T_e}{\partial t} = \gamma (T_e - T_i) \tag{3.3}$$

$$\tag{3.4}$$

where T_e and T_i are the electron and lattice temperatures respectively, C_e and C_i are the electron and lattice heat capacities respectively, z is the distance of the laser propagation, γ is the electron lattice coupling, $Q(z)$ is the heat flux, and S is the source laser heating term. They are defined as,

$$Q(z) = -k_e \frac{\partial T_e}{\partial z} \tag{3.5}$$

$$S = I(t) \cdot A \cdot \alpha e^{-\alpha z} \tag{3.6}$$

where $k_e$is the electron thermal conductivity, $A = 1 - R$ is the surface interface transmission, and a is the material absorption coefficient. The electron and lattice cooling time can be defined as $\tau_e = C_e/\gamma$ and $\tau_e = C_e/\gamma$ respectively, where $\tau_e \ll \tau_i$. For the plasma source described here the laser pulses width (τ_L) is on the nanosecond scale, and therefore $\tau_i \ll \tau_L$. With this assumption, the lattice and electron temperatures can be considered semi-equal because the thermal transfer occurs significantly faster than the pulse duration. Therefore, the model can be simplified to

$$C_i \frac{\partial T_e}{\partial t} = k_e \frac{\partial T_e}{\partial z} + I_\alpha \alpha e^{-\alpha z} \tag{3.7}$$

Here a significant portion of the laser energy is transferred by conduction to the bulk material creating a melt region.

As seen in Figure 3.1, the thin area of liquid target material between the bulk medium and the plasma is called the melt region. [110] This region does not receive enough energy to be vaporized. Instead it is melted, and the shock of the plasma front pushes on the melt region near the surface, which subsequently ejects material. The melted material, when cooled, creates nano-scale particulate matter that travels at high velocities (>100 m/s) and can coat optics in proximity to the plasma source. [111] Once the surface of the planar target has been irradiated a heat affected zone is formed and the surface becomes irregular. In addition, the melt zone remains liquid on microsecond time scale, [110] long after the laser pulse has acted as a heat source. These changes in target conditions can result in significant changes in plasma emission. If the previously irradiated area is irradiated again while the target is still in the liquid phase, then the amount of material vaporized will increase and causes an increase in the initial plasma density. To prevent changes in plasma emission caused by changes in the target properties, a fresh target surface is required for each laser pulse.

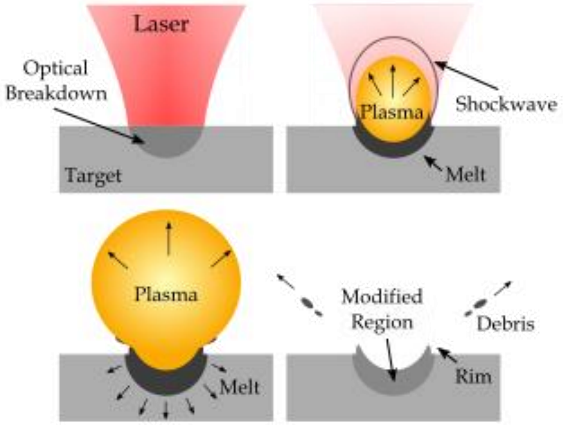

Figure 3.1: Ablation process of solid planar targets [110]

3.1.1 Position Control

Solid planar targets require continuous motion of the target surface, to provide a new surface for laser irradiation. There are several methods of obtaining this. For low laser pulse repetition rates on the order of 10 Hz and lower, a linear stage can be used to translate the target across the plasma position. Using two orthogonal stages allows for the whole surface of the target to be used; however, linear stages have to slow their travel in order to change directions. This results in an overlap of ablated material with higher repetition rate pulses. The change of the target geometry changes the irradiance conditions, from a non-overlapping condition. This results in an unstable plasma emission. Another technique is a tape or wire feed system. A flat target ribbon or a wire is transferred from a supply spool to a collection spool. While this method can yield long term operation and can operate at very high repetition rates, acquiring some target materials in this geometry can be challenging. If the material has a high malleability or ductility, then it can deform during dispensing; if it is hard or brittle then it can fracture. To alleviate these issues associated with the above techniques, translation of the target in a cylindrical coordinate system results in a smoother motion and eases the requirements of the motion stages. Additionally, the targets in the cylindrical geometry plate are readily available.

In the cylindrical translation scheme, shown in Figure 3.2, the target plate is rotated about the Z-axis, with a varying angular velocity while translated linearly with a varying velocity. With this scheme, a target can have a thickness on the scale of the laser ablation depth, and the diameter is only limited by the linear stage and the area inside of the plasma chamber. It is advantageous because that most metals are readily available in flat thin sheets which can be cut

to the target geometry. Furthermore, the larger surface to volume ratio of this target geometry allows for efficient cooling of the target. This is the method and geometry utilized in this work.

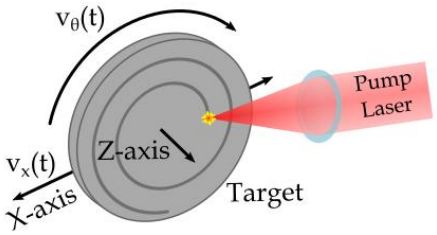

Figure 3.2: Cylindrical targeting scheme for solid planar target

The limitations in maximum repetition rate of the plasma and total source time is limited by the maximum angular velocity and the target diameter. With a rotating target, the angular velocity is critical to optimize use of the target. If it rotates too slowly then the laser will overlap pervious laser ablation craters. Rotating too fast will reduce the total target time and leave unused target material. When the target it rotated so that the edge of the irradiated spot is overlapped with edge of the previous spot. The angle of rotation is calculated as,

$$\theta_{rot} = 2 \cdot \tan^{-1}\left(\frac{r_{laser}}{R}\right) \quad (3.8)$$

where r_{laser} is the spot size radius of the laser on the target, and R is the distance from the center of rotation. By multiplying this angle by the repetition rate of the laser f_{laser}, the optimal target rotation speed is derived as,

$$\omega_{stage} = 2 \cdot f_{laser} \cdot \tan^{-1}\left(\frac{r_{laser}}{R}\right). \quad (3.9)$$

While the maximum target radius is only limited by the space available, the minimum target radius (Equation (3.10)) is limited by the maximum angular velocity ω_{max} and the size of the laser spot radius.

$$R_{min} = \frac{r_{laser}}{\tan[\omega_{max}/(2 \cdot f_{laser})]} \quad (3.10)$$

Here a larger spot size or a faster repetition rate allows for an increase in shots per target. Lastly, the velocity of the linear stage (v_{stage}) is defined by the time necessary for the rotation stage to complete one revolution, as shown below,

$$v_{stage} = \frac{\omega_{stage} \cdot r_{laser}}{\pi} \quad (3.11)$$

3.1.2 Laser Alignment

Aligning the laser to the surface of the planar target is important for achieving accurate irradiance conditions. It is critical for the surface of the target material to maintain its distance from the optics of the laser to maintain the plasma size and temperature. Small changes in this distance on the scale of tens of microns can significantly change the irradiance conditions, which change the temperature of the plasma. Plasma emission is directly dependent on the plasma temperature; it is affected by laser alignment.

In order to align the laser's focus to the plasma position, a polished metal sphere is centered at the desired plasma position. As seen in Figure 3.3, when the laser focuses onto the metal sphere the light is reflected back along the incident beam through the focusing lens. A

small alignment error will cause the reflected beam's divergence to change. If the angles are assumed to be small, then ABCD ray transfer matrices for paraxial approximation can be used. The equation for the optical ray path is defined as,

$$\begin{bmatrix}\omega_o\\ \theta_o\end{bmatrix} = \begin{bmatrix}1 & d_1\\ 0 & 1\end{bmatrix}\begin{bmatrix}1 & 0\\ -1/f & 1\end{bmatrix}\begin{bmatrix}1 & d_2\\ 0 & 1\end{bmatrix}\begin{bmatrix}1 & 0\\ 4/D & 1\end{bmatrix}\begin{bmatrix}1 & d_2\\ 0 & 1\end{bmatrix}\begin{bmatrix}1 & 0\\ -1/f & 1\end{bmatrix}\begin{bmatrix}1 & d_1\\ 0 & 1\end{bmatrix}\begin{bmatrix}\omega_i\\ \theta_i\end{bmatrix} \quad (3.12)$$

where ω_i and θ_i are the incident beam radius and divergence, d_1 is the distance to the lens, f is the lens's focal length, D is the diameter of the reflective sphere, d_2 is the distance between the focal lens and the reflective sphere, and ω_o and θ_o is the reflected beam radius and divergence, at distance d_1 from the focal lens.

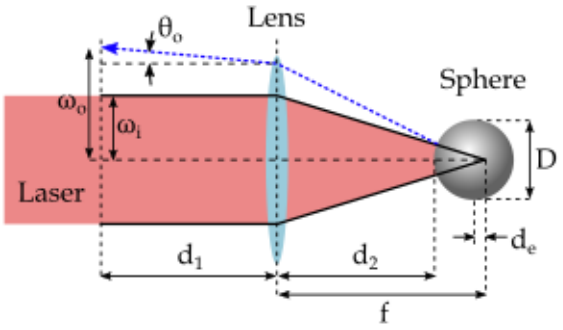

Figure 3.3: Schematic of laser alignemnt techique

If the divergence of the incident beam is assumed to be $\theta_i = 0$, and $d_2 = f + d_e - D/2$, then the change in the reflected beam radius $w_d = \omega_0 - \omega_i$ is,

$$w_d = \frac{-\omega_i[d_e^2 4(D - d_1) + d_e 2(2f^2 - fD + d_1 D)]}{f^2 D} \quad (3.13)$$

The change in d_e has a quadratic relation to w_d, which leads to large changes in the reflected beam diameter for small changes in the distance between lens and plasma position. Also, a smaller sphere, or longer distance d_1, will provide a larger change in w_d with respect to d_e. The laser is aligned to the reflective sphere while the diameter of the reflected beam is measured. Once the incident and reflected laser beams are aligned and have the same beam radius at d_1, then the laser is aligned to the plasma position.

In addition to the laser alignment, two alignment beams orthogonal to each other are aligned to the sphere using the same technique. These are low power visible wavelength CW lasers, which provide an addition visible reference point where their beams cross to aid in the alignment of targets and metrological devices. This then establishes the focus position in three dimensional space, independent of other parameters. The planar target stage is loaded with a high reflectivity dummy target, which as an optical quality finish. The stage is aligned until incident guide beams overlap on the target, and the reflected beams counter propagate with each other. The dummy target is then replaced with the laser plasma target. In this condition, the planar target's surface is aligned to the focal spot of the laser. When atmospheric gas is evacuated from the chamber, the refractive index reduces by ~.00027. [112] The effect of this change, is a small increase of the focal length (~0.09%), which can be estimated using the thick lens formula (Equation (3.14)), with the refractive index $n = n_{lens}/n_{chamber}$. [85]

$$\frac{1}{f} = (n-1)\left[\frac{1}{R_1} - \frac{1}{R_2} + \frac{(n-1)d}{nR_1R_2}\right] \qquad (3.14)$$

After alignment, the change in focus is compensated by translating the lens away from the target.

3.2 Liquid Droplet Target

Liquid droplet geometries have several advantages over solid target geometries. Their atomic densities are on the order of $10^{22} – 10^{23}$ ions/cm^3, which is similar to solids, and have similar plasma formation properties to solids. However, they allow a controlled volume of material that, under the optimal conditions, can be fully ionized by the laser. Fully ionizing the target reduces the formation of large particles during ablation, therefore significantly reducing debris. [41] Additionally, liquid droplets allow for accurate control of the number of ions which contribute to the emission. Another significant advantage over solid targets is the continuous supply of new targets. The number of shots that a solid target can provide is limited, requiring the target to be replaced afterwards. With liquid droplet targets, a continuous supply of targets can be provided, only limited by the size of the supply reservoir. It is these advantages that have motivated the current high volume manufacturing using EUVL to select liquid droplet based targets as, for their primary laser target. [113]

Typical droplet generation is performed with a jet of liquid forced with high pressure through a capillary, which then breaks into a stream of droplets. The breakup of the droplets is typically triggered using a mechanical perturbation. When dispensing droplet targets, the parameters of the capillary and of the fluid droplet formation must be considered. The droplet chemistry affects the physical parameters such as viscosity and surface tension, which control how a droplet forms. Significant changes in droplet chemistry requires changes in the dispensing parameters. In addition, the droplet stability is significantly affected by mechanical, and environmental perturbations, and by neighboring electric charges. The effects of these factors create random positioning and timing errors of the droplets and long term drifting of position. To

provide a reliable laser target, it is necessary to have adaptive positioning and timing control. [114]

3.2.1 Fluid Dynamics

Formation of a droplet starts when a liquid is forced through an orifice creating a liquid jet. The jet has inherent instabilities, which exponentially grow, causing the eventual breakup into droplets due to the Plateau–Rayleigh instability. For an idealized jet, the distance from the orifice at which this breakup occurs is defined by, [115]

$$l = v \cdot \ln\left(\frac{d_{jet}}{2\delta_0}\right)\left(\sqrt{\frac{\rho {d_{jet}}^3}{\sigma}} + \frac{3\eta d_{jet}}{\sigma}\right) \quad (3.15)$$

where v is the jet's velocity, d_{jet} is the jet's diameter, δ_0 is the initial disturbance, ρ is the fluid density, σ is the surface tension, and η is the viscosity. The distance l, sets the minimum distance that a capillary can be located from plasma the target position. Initial disturbances cause random perturbations in the droplet stream which become sinusoidal. These can grow to dominate the other components. This frequency ultimately defines the droplet frequency. To prevent a random droplet frequency from forming, a stronger induced perturbation will override the random perturbations providing a controlled droplet stream. With regular perturbations at frequency f on a liquid jet with a diameter d_{jet}, and flow velocity of v, the volume of fluid between perturbations can be calculated with Equation (3.16).

$$V_{jet} = \frac{v}{f}\pi\left(\frac{d_{jet}}{2}\right)^2 \tag{3.16}$$

As the fluid continues to flow the perturbations form regular droplets of with a volume defined by Equation (3.17)

$$V_{droplet} = \frac{4\pi}{3}\left(\frac{d_{droplet}}{2}\right)^3 \tag{3.17}$$

By equating the volume V_{jet} with the droplet volume $V_{droplet}$ the droplet diameter $d_{droplet}$, (Equation (3.18)) can be derived.

$$d_{droplet} = 1.145\left(\frac{v \cdot {d_{jet}}^2}{f}\right)^{1/3} \tag{3.18}$$

The on center distance between droplets can be determined using the following equation.

$$\frac{v}{f} = d_{distance} \tag{3.19}$$

By specifying the velocity of the jet in conjunction with the droplet frequency and jet diameter, the droplet size can be selected.

3.2.2 Droplet Stability

Droplets are highly susceptible to environmental factors such as mechanical vibration. Vibration causes changes in pressure in the fluid dispensing system, which causes a change in the fluid jet velocity. From Equation (3.15), the start of the droplets formation is dependent on the velocity of the jet and the initial disturbance. The change in position causes the relative phase of the droplets to shift. As these targets are synchronized with the laser pulses, this phase shift acts as a linear translation of the droplet from the target position, contributing to error in targeting. These phase shifts occur randomly due to vibrations in the liquid droplet dispenser system, and localized pressure variations within the liquid stream due to turbulence. To improve the phase stability of the droplets, vibrational isolation of the target reservoir, fluid feed lines and capillary are necessary. In addition to mechanical stability errors, the droplet capillary is susceptible to electrical timing errors.

When a droplet is ionized into a plasma, the expanding material cools into gas, aerosols, and particulate matter. The resulting material expands outward and collides with fresh incoming targets. The momentum of the material is transferred to the droplet, which changes its velocity. The applied force is uneven due to turbulence in the expanding material which creates random acceleration of the droplet orthogonal to the droplet stream, which results in random horizontal shifts in the target position. Horizontal shifts are typically small fractions of the droplet diameter, and typical average over time. However, they can accumulate into a larger drift over several seconds. In addition to shifts, the droplet's velocity toward the target position is reduced by the expanding material causing a delay in droplet timing. These delays cause uneven ionization of the target, which results in a change in the distribution of condensed material, which in turn

causes a change in the forces imparted on the fresh target droplets. In many cases, a feedback loop is formed causing oscillation of the droplet position from drop to drop, or a continuous drift in one direction. An example of this effect, is when a delay in the droplet phase causes the laser to target a droplet on its lower half. As seen in Figure 3.4, the lower part of the droplet vaporizes and is ionized first, creating a shockwave that travels upward through the rest of the droplet. This creates a wave of dense gas and aerosols that propagates preferentially toward fresh incoming droplets, slowing them further causing further phase delay.

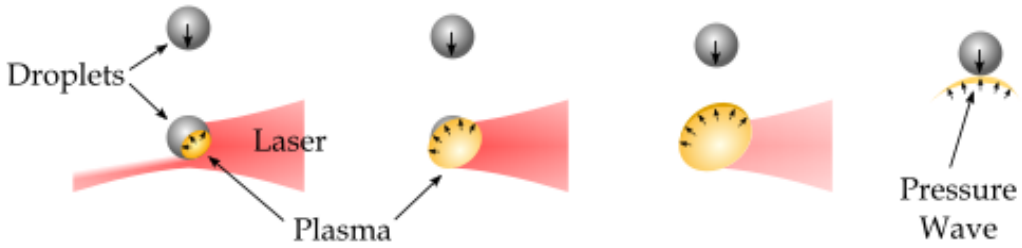

Figure 3.4: Propagation of plasma and pressure wave due to misaligned laser on target

If the droplet drifts too far out of the focal positon, then the forces on the incoming droplets subsides momentarily and can start an oscillation in the droplet position. The initial errors in alignment from mechanical vibrations above can trigger vapor driven oscillations on the order of a few Hz or long term drift over the diameter of a droplet over several seconds. Additionally, droplet stability is affected by fluctuations of laser intensity which cause changes in the debris constituents and momentum. To ensure high stability of the ionized target material, careful alignment of the droplet with the laser, and a stable laser are critical. While many of the instabilities inherent to a droplet based target system are difficult to predict and control, many average to form small changes in droplet position on the order of tenths of the droplet diameter. Some of these effects can be mitigated by increasing the ratio of laser spot size to droplet

diameter. By using this technique, a small perturbation of the droplet will not push the droplet out of the irradiation area. Another technique to improve droplet stability is to increase the distance between droplets or reduce the droplet frequency. This allows more space and time for vaporized target material to dissipate before interacting with the next droplet. For the experiments described in this work the droplet frequency was increased to an integer multiplier of the laser frequency so that every Nth droplet was irradiated. The non-irradiated droplets provide a shield for the incoming droplets from the irradiated droplets, and significantly reduced the instabilities of the droplet system. The remaining long term instabilities of the droplet position with the laser are manageable with a continuous active position control system, which will be described in the following section.

3.2.3 Position Control (ADaPTS)

Changes in the droplet position as described above require an adaptive position control system. Two separate positioning techniques are required for horizontal and vertical positioning of the droplets at the plasma position. Horizontal positioning of the droplets can be performed with linear motion stages. However, for vertical positioning a linear stage is impractical due the fast nature of vertical droplet motion as compared to standard linear stages. In this case, the phase of the droplet is changed with respect to the laser pulse. Based on Equation (3.19) the relative vertical shift in droplet position with respect to the laser pulse at the plasma position is defined as,

$$d_{phase} = \frac{v \cdot \varphi}{2\pi f} \qquad (3.20)$$

where φ is the phase shift of the droplets. The total range of linear shift of the droplet is equivalent to the droplet spacing as defined in Equation (3.18), at which point the neighboring target moves into the target position. The phase of the droplets is controlled by adding a phase shift into the clock driving the droplet generator.

In order to correct the position of the droplet targets, the ADaPTS (Advanced Droplet and Plasma Targeting System) is used. [114] This system requires two or more imaging systems, which capture imagines of the current droplet target. These images are analyzed to determine the position of the droplet. The position is then compared with a user defined droplet position, and an error is calculated. If this error is within a pre-determined tolerance, then ADaPTS acquires new images of the droplet. If the error is outside of tolerance, then the system moves the linear stages for horizontal motion orthogonal to the droplet dispensing direction and adjusts phase of the electrical signal driving the droplet dispenser for vertical positioning. Once the target is moved ADaPTS starts the process again to recheck the droplet position. With this continuous adaptive control, significant perturbations to the droplets position and long term drifting of position are effectively eliminated, providing stable and repeatable droplet targets.

3.3 Gas Jet Target

Gas, as a laser plasma target, has several key advantages over other target materials. The main benefit is that these targets do not generate debris from the plasma, making them optimal for debris sensitive applications. Another advantage is that there are many noble gases and diatomic gases that can be used. Noble gases are single unbound atoms while, diatomic gases recombine when they lose their energy to radiation, allowing these target materials to be reused in a gas laser plasma source. A distinct disadvantage with gas targets is the low atomic density.

At atmospheric pressure gases have a typical atomic density on the order of 10^{19} atoms/cm^3 and electron densities on the order of $10^{19} – 10^{21}$ e/cm^3 at atmospheric pressures. Lower initial absorption of laser light due to the low densities, can make formation of a plasma difficult. To increase the ion density and laser absorption, higher gas pressures are required. With bulk gas sources, the density of the target gas is limited by the pressure handling capabilities of the target chamber. Furthermore, the higher density gas surrounding the plasma can reabsorb the emitted radiation, reducing the overall emission from the gas chamber. Gas jets overcome the limitations of bulk gas targets by providing high density over a small volume, thereby reducing reabsorption.

As seen in Figure 3.5, gas jet targets are produced by the flow of high pressure gas through a nozzle into a lower pressure environment. The laser interacts with the gas jet in close proximity to the nozzle where the density of the gas is highest. The nozzle geometry determines the extent of the gas at the plasma position, which is on the same order as the of nozzle's diameter. Due to the limited extent of the target material at this position, the size of the plasma can be controlled. Also, the irradiance conditions can be changed by translating the position of the gas jet along the optical axis of the focused laser. Alignment of the gas jet with the target is performed with a 3-axis linear stage.

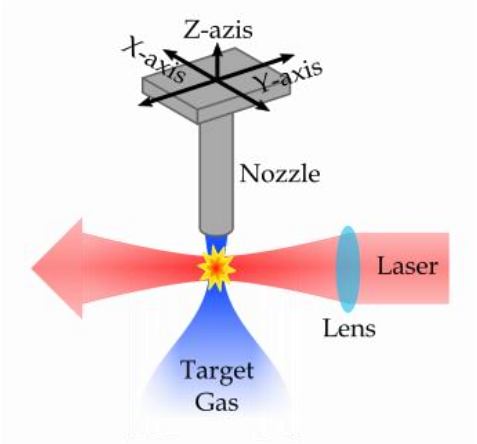

Figure 3.5: Layout of gas jet laser pasma source target

3.3.1 Gas Flow

The flow of gas out of a nozzle is a complex process involving fluid dynamics. A full discussion of gas flow mechanics is outside the scope of this work and is described further in [116], and [117]. However, this section will discuss flow conditions for producing "choked" gas jets, and the expansion of these jets into the target chamber. When a compressible fluid or gas flows from a high pressure through an orifice to a lower pressure, then the gas reaches sonic flow velocity at the orifice. Increasing the pressure will only increase the mass flow; however, the velocity downstream from the orifice will remained fixed. This condition is known as choked flow and is satisfied when the ratio of the upstream (P_0) to downstream (P_c) pressure satisfies, [116]

$$\frac{P_c}{P_0} \leq \left(\frac{2}{k+1}\right)^{\frac{k}{k-1}} \qquad (3.21)$$

where $k = c_p/c_v$ is the heat capacity ratio. Typical values of k for common gases fall between 1.05 – 1.67. [118] Using these values, choked flow occurs at pressure ratios of 0.6 – 0.49. The mass flow rate under these conditions is shown as, [118]

$$Q_m = C_d A \sqrt{k \rho_0 P_0 \left(\frac{2}{k+1}\right)^{\frac{k+1}{k-1}}} \quad (3.22)$$

where C_d is the discharge coefficient, A is the area of the orifice, k is the heat capacity ratio, and ρ_0 is the density of the gas upstream from the orifice. [119] It is important to note that the mass flow is independent from the downstream pressure. For a given orifice size, the gas density of the downstream jet can be set by the applied pressure upstream from the nozzle.

3.3.2 Target Chamber Evacuation

With the influx of target gas from the gas jet into the target chamber, the pressure of the target environment will quickly rise. The chamber pressure as a function of time is estimated using a derivation of the ideal gas law as, [117]

$$P_c(t) = P_{jet} \frac{T_c}{T_{jet}} \frac{Q_{jet} \cdot t}{V_c} + P_i \frac{T_c}{T_i} \quad (3.23)$$

where P_{jet} is the pressure of the gas jet, $T_c(t)$ is the temperature of gas in the chamber, T_{jet} is the temperature of the gas jet, Q_{jet} is the volumetric flow rate of the gas jet, V_c is the volume of the chamber, P_i is the initial pressure of the chamber, and T_i is the initial temperature of the

chamber. If the temperature of the chamber and jet is maintained at the initial chamber temperature, then Equation (3.23) reduces to,

$$P_c(t) = P_{jet}\frac{Q_{jet} \cdot t}{V_c} + P_i \qquad (3.24)$$

As the pressure in the chamber increases, absorption increases for some wavelengths of the emitted plasma light. If there is a required absorption limit for a particular wavelength, then by substituting the maximum pressure (P_{max}) for $P_c(t)$ in Equation (3.24), and solving for t, the maximum time (t_{max}) that the gas jet can operate is,

$$t_{max} = \frac{(P_{max} - P_i)}{P_{jet}}\frac{V_c}{Q_{jet}} \qquad (3.25)$$

As the gas from the jet is ionized by the absorbed laser energy and reabsorbed emission light, the temperature within the target chamber begins to rise, causing the pressure to further increase.

To maintain the surrounding environment of the gas-jet plasma below a predefined pressure, a system for removing the gas is required. For applications where the pressure is greater or equal to atmospheric pressure, a valve that opens at a predefined pressure can be used to vent the excess gas. When the environmental pressure is lower than the atmospheric pressure a pumping system is required. For lower pressures above 10^{-3} Torr, a simple roughing pump can be used. If lower pressures are required, then a turbomolecular pump is required. The pumping capacity of the pumps should be greater than the flow rate of the gas jet.

CHAPTER 4: SOURCE RADIATION METROLOGY

In order to measure and characterize laser-plasmas, a wide variety of metrological equipment is necessary. Radiation metrology can be classified into two categories, laser light metrology and plasma source light metrology. Measurements of the laser are required to determine the initial plasma conditions such as light intensity, target irradiation area, and temperature. These measurements also allow for optimization of the target irradiation and subsequent plasma. Source metrology is required to determine the plasma emission's spectral content, and to determine the irradiance. In addition, imaging of the plasma source provides measurements of plasma size, and its etendue, providing estimates on optical collectability of plasma radiation. The following sections will discuss these metrology systems. The description and design of the spectrometers used in these experiments will be discussed. This is followed by the design specification of a calibrated in-band energy meter, specific to 13.5 nm EUV light. Finally, a gated imaging system is described which provides several nanosecond resolution imaging within the VUV band.

4.1 Plasma Source Spectral Measurement

Spectral measurement of plasma emission of the plasma sources discussed in this thesis were performed using several spectrometers. For the VUV-MS-Facility, four spectrometers were used to capture light in a spectral range of 5 – 250 nm, as seen in Figure 4.1. An Ocean Optics Maya 2000 spectrometer was used to measure light with wavelengths from 140 – 250 nm. For the wavelength range from 115 – 170 nm, a modified McPherson 234/302 spectrometer with an image intensifier was used. For the 22 – 124 nm wavelength range a custom-built VUV Harada

style grazing incidence spectrometers was used. A similar EUV Harada style spectrometer was used for the 5 –20 nm spectral range. These spectrometers were absolutely calibrated for irradiance across the spectral range of 120 – 250 nm using a calibrated NIST traceable Deuterium lamp.

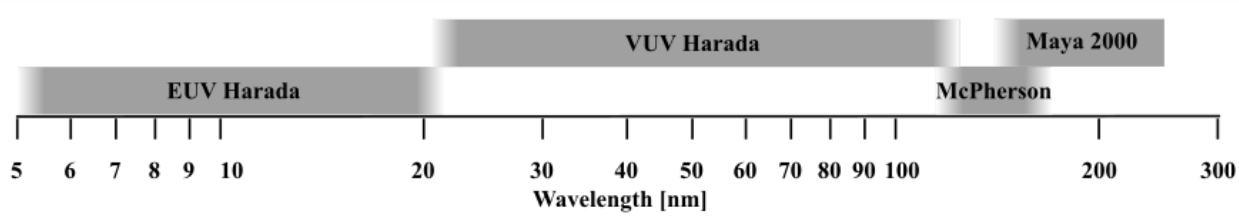

Figure 4.1: Wavelength range of VUV-MS-Facility spectrometers

For the HP-EUV-Facility measurement of a narrow band of wavelengths is required around the 13.5 nm spectral peak. For this source, a Harada style grazing incident spectrometer measures a wavelength range of 10.5 – 17.5 nm. These spectrometers are discussed in detail in the following sections.

4.1.1 Seya-Namioka Style Intensified Spectrometer

Measurements in the 115 – 170 nm range were performed with a modified McPherson 234/302 aberration corrected Seya-Namioka style monochromator. The monochromator has a 10 µm slit with a 0.11 NA with a magnesium fluoride MgF_2 window. The grating is a variable magnesium fluoride coated variable groove spacing grating with a nominal 1200 grooves/mm.

The monochromator only provides a single wavelength at a time for measurement and was thus modified to capture a single spectrum, as seen in Figure 4.2. A fiber face plate intensifier was added at the focal plane of the grating. The intensifier is comprised of cesium

iodide (CsI) coated Galileo 25mm diameter micro-channel plate (MCP) with a maximum gain of 10^6, coupled to a P20 phosphor and bonded to a fiber optic face plate. In contact with the fiber optic faceplate is a Princeton Instruments PIXIS-XF:1024B back-illuminated charge coupled device (CCD). The imaging area of the CCD is 13.3 x13.3 mm with 13x13 µm pixels. The CCD is able to capture ~105 nm of spectrum per acquisition. The MCP has low sensitivity to higher wavelengths, and has a wavelength cut off of at wavelengths greater than ~180nm due to the lack of sensitivity of CsI photocathode. Additionally, the MgF_2 window prevents shorter wavelengths from reaching the detector and has a cutoff of 110 nm. With these two cutoffs, the useful range of the spectrometer is 115 – 170 nm. The grating on the spectrometer can be rotated through a built-in rotational stage to shift the spectrum incident on the detector.

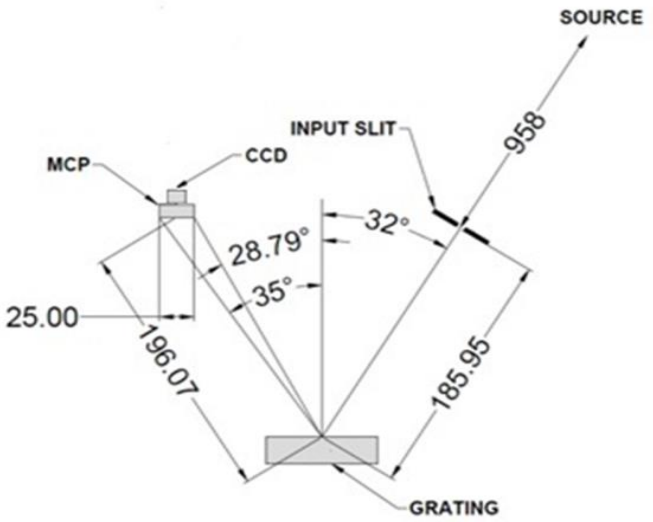

Figure 4.2: Schematic diagram of modified McPherson monochromator showing, input slit, gratin, MCP, and CCD

Calibration of the spectrometer was performed by setting the grating so that central wavelength captured was fixed at 115, 145, and 160 nm, and then capturing the spectrum of an

NIST traceable calibrated Hamamatsu L9841 Deuterium lamp DUV source. The source was placed at 500 mm from the spectrometer. To correct for the difference in distance between the spectrometer and the calibration lamp (500 mm), and the spectrometer and the plasma source (958 mm), the following function was used on the calibrated D2 spectrum.

$$E2 = E1 \times \left(\frac{500\ mm}{958\ mm}\right)^2 \qquad (4.1)$$

With this measurement, the irradiance transfer function was obtained. The deuterium lamp source spectrum has several peaks due to line emission (Figure 1.12). This can result in calibration errors when applying the transfer function to obtained spectrum. To reduce these effects, the spectrum was smoothed with a moving average function to produce a smoothed transfer function (Figure 4.3).

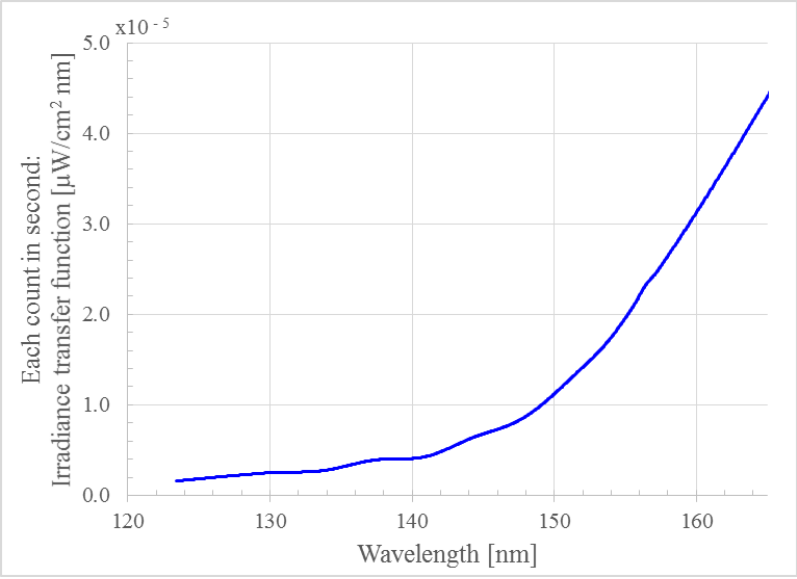

Figure 4.3: Irradiance transfer function of modified McPherson spectrometer with smoothed irradiance transfer function for 123 – 165 nm

4.1.2 Grazing Incident Harada Style Spectrometer

For short wavelengths (<120 nm) the efficiency of gratings is reduced. [120] In order to improve efficiency a grazing incidence grating is used in a Harada style spectrometer These gratings use a toroidal shape and a variable groove spacing defined by a 4th order polynomial that provide aberration correction and a flat focal plane. [121] The flat focal plane allows for the use of flat electro-optical detectors such as CCDs. Spectrometers for these wavelength regions require the use of sealed vacuum systems due to the complete absorption of most wavelengths by the main components of air (oxygen, nitrogen, and argon). [73] For these spectrometers their environment was maintained at 10^{-4} Torr using turbo molecular pumps.

4.1.2.1 VUV Harada

For the 22 – 124 nm range a spectrometer with a 600 nominal groove/mm Hitachi 001-0639 grating was custom-built. It has a grating area of 30x50 mm, a blaze wavelength of 31 nm, a 3.7 º blaze angle, and a radius of curvature of 5649 mm. As seen in Figure 4.4, the spectrometer has an input slit to output slit distance of ~819 mm. The spectrometer has a dispersion of ~0.93 nm/mm which results in a spectral plane has a length of 110.16 mm.

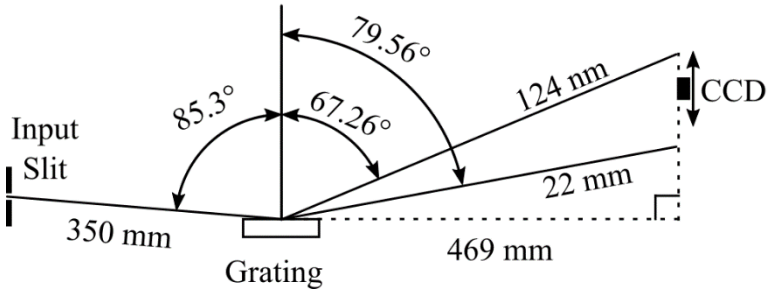

Figure 4.4: Schematic layout of VUV Harada spectrometer, showing input slit, grating, and output image plane with relevant dimensions and angles (not to scale)

The focal points for each wavelength were calculated in the image plane using the grating equation,

$$m \cdot \lambda = d(\sin\theta_i + \sin\theta_r) \tag{4.2}$$

where m is the diffraction order, λ is the wavelengths, d is the groove spacing, θ_i and θ_r are the incident and reflected angle of light with respect to the grating normal. As seen in Figure 4.5, the wavelength focus for wavelengths longer than 85 nm diverge from the CCD focal plane. To determine the spectrometer dispersion at the CCD focal plane projections of the wavelength focus to the detector plane were calculated (Figure 4.5 in red). The aberrations due to this divergence, cause a reduction in spectral resolution at longer wavelengths.

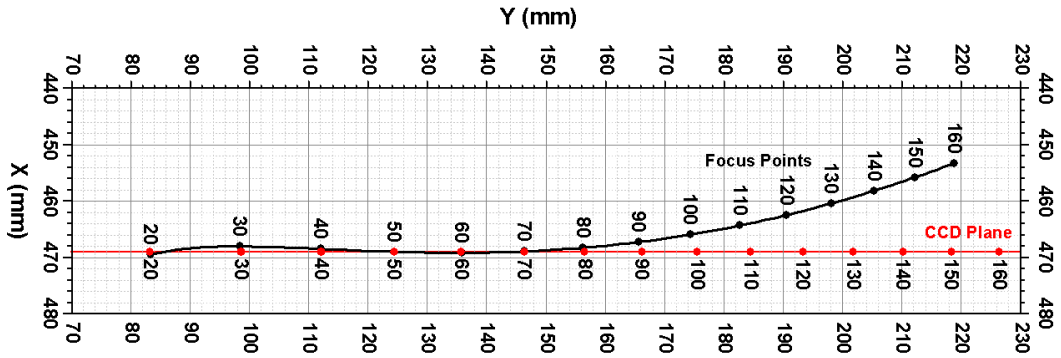

Figure 4.5: Calculated VUV spectrometer grating focal points, and central incident point on CCD detector with respect to wavelength.

The detector in this spectrometer was a Princeton Instruments PIXIS-XO:100B back-illuminated charge coupled device (CCD). The imaging area of the CCD is 26.8x2 mm with 20x20 µm pixels. Due to the limited size of the detector the spectrometer can only capture 24.8 nm of spectral bandwidth at one time. The input slit is an adjustable width slit set at 10 microns. The measured spectral resolution of this spectrometer is 0.1 nm.

In order to capture different spectral ranges within the full spectral bandwidth, the CCD is mounted on a translation stage that translates it across the image plane (Figure 4.6). The CCD translation stage consists of a sliding plate with a vacuum seal. The plate is translated with position encoded motor.

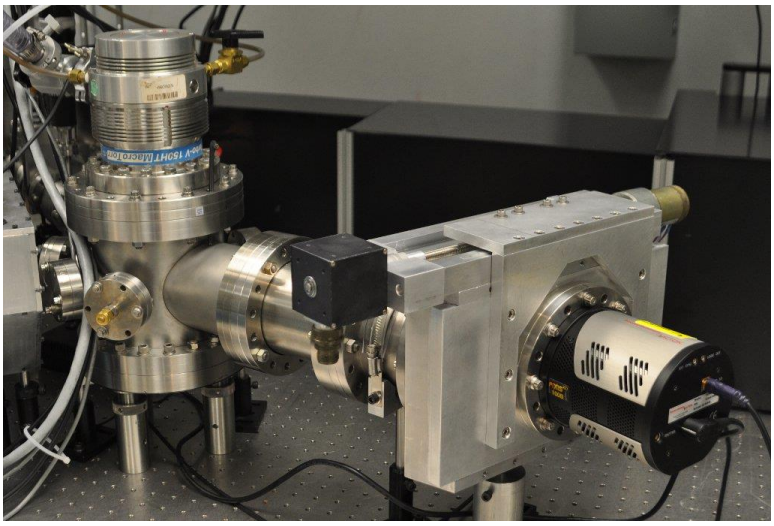

Figure 4.6: VUV Harada spectrometer showing grating vacuum chamber, turbomolecular pump, and CCD translation stage

4.1.2.2 EUV Harada

For the 5 – 20 nm range a spectrometer with a 1200 nominal groove/mm Hitachi 001-0437 grating was used. It has a grating area of 30x50 mm, a blaze wavelength of 10 nm, a 3.2 º blaze angle, a radius of curvature of 5649 mm. As seen in Figure 4.7, the spectrometer has an input slit to output slit distance of ~472 mm. The spectrometer has a dispersion of ~0.59 nm/mm which results in a spectral plane has a length of 25.3 mm.

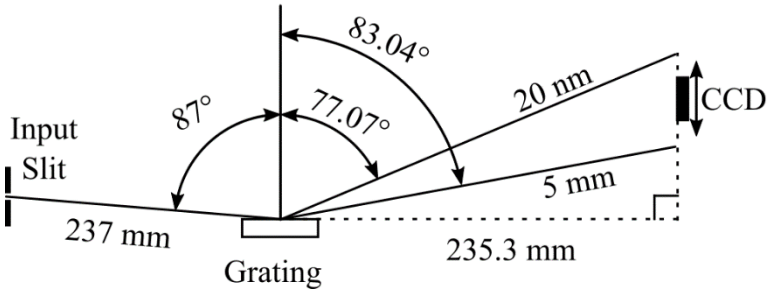

Figure 4.7: Schematic layout of EUV Harada spectrometer, showing input slit, grating, and output image plane with relevant dimensions and angles (not to scale)

The focal points for each wavelength were calculated in the image plane using the grating Equation (4.4). As seen in Figure 4.8, the wavelength focus for wavelengths shorter than 7 nm diverge from the CCD focal plane. To determine the spectrometer's wavelength spacing at the CCD focal plane, projections of the wavelength focus to the detector plane were calculated (Figure 4.8 in red). The aberrations due to this divergence, causes a reduction in spectral resolution at shorter wavelengths.

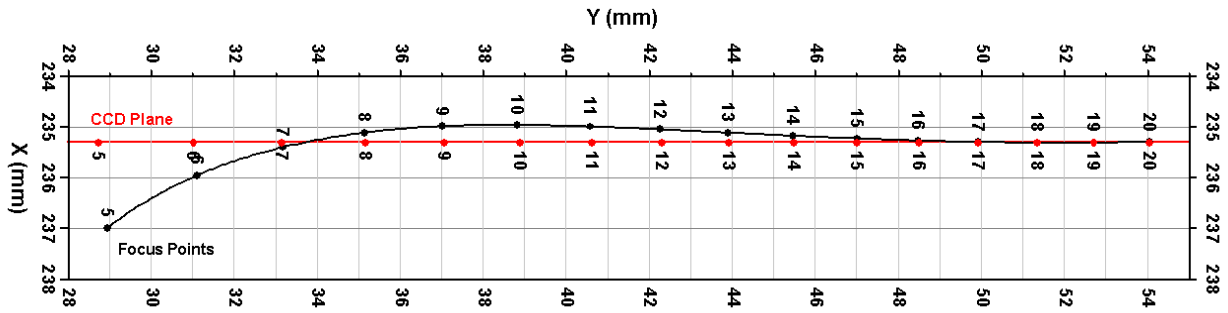

Figure 4.8: Calculated EUV spectrometer grating focal points, and central incident point on CCD detector with respect to wavelength.

The detector in this spectrometer, is a Princeton Instruments PIXIS:512 back-illuminated charge coupled device (CCD). The imaging area of the CCD is 12.3x12.3 mm with 24x24 µm pixels. Due to the limited size of the detector the spectrometer can only capture 7.28 nm of spectral bandwidth at one time. The input slit is an adjustable width slit set at 10 microns. The measured spectral resolution of this spectrometer is 0.04 nm.

In order to capture different spectral ranges within the full spectral bandwidth, the CCD was mounted on a vacuum bellow on a translation stage. The stage translates the CCD across the image plane (Figure 4.7). An identical spectrometer was used for the mass–limited EUV plasma sources, and VUV laser plasma sources. However, for the HP-EUV-Facility only capturing a

narrow wavelength region, transmitted by EUV multi-layer optics, is required for optimizing plasma conditions. The spectrometer (Figure 4.9) used in these experiments was fixed at a central wavelength of 13.5 nm, covering an approximate wavelength range of 9.8 – 17.1 nm.

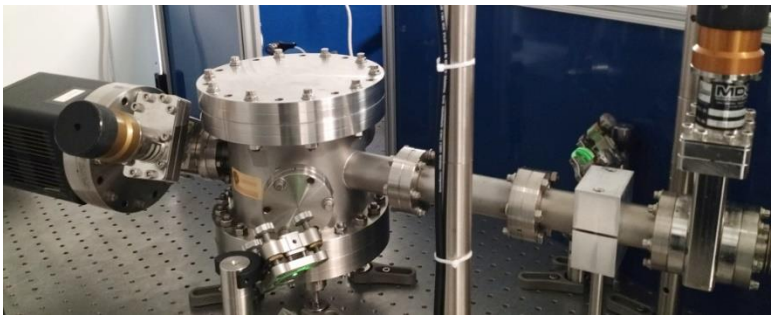

Figure 4.9: EUV Harada spectrometer showing grating vacuum chamber, and fixed CCD

4.1.3 Maya2000 Pro UV Spectrometer

To measure the wavelength range from 140 – 250 nm, an Ocean Optics Maya2000 Pro spectrometer was used. This spectrometer has a crossed Czerny-Turner design. As seen in Figure 4.10, the spectrometer consists of a 25 µm input slit mounted on an optical SMA connector, followed by a collimating mirror which collects the input light at a 0.127 NA, and illuminates the grating. The grating has 1200 grooves/mm and is optimized for the DUV range. The light reflected from the grating is the focused onto a Hamamatsu S10420 line CCD with 2068x64 pixels, 14x14 µm and pixel size.

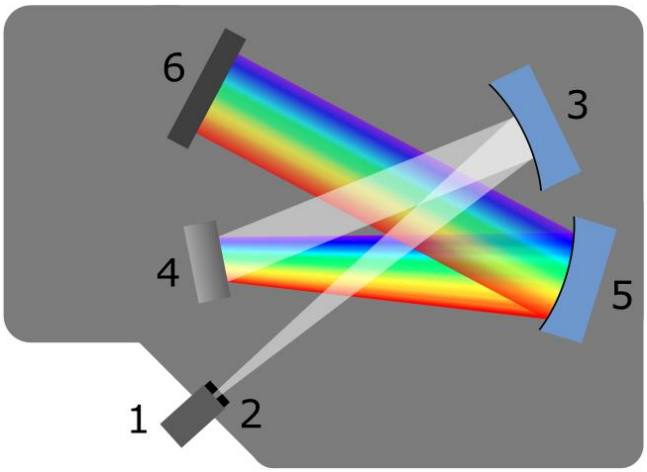

Figure 4.10: Layout of Maya2000 Pro spectrometer showing, 1) SMA mount, 2) 25 um input slit, 3) collimating lens, 4) 1200 groove/mm grating, 5) focusing lens, 6) line CCD [122]

To maximize the collected light to the spectrometer an optics assembly was designed (Figure 4.11) and installed onto the spectrometers SMA input connector. This simple telescope is made of two calcium fluoride plano-convex lenses. These optics have relatively flat transmission that over 90% at wavelengths longer than 200 nm, and drops to 65% at 140 nm. The two 25.4 mm diameter lenses in the system, are 75 mm and 100 mm focal length, with the 100 mm focal length lens located at 100 mm from the input slit, and the 75 mm lens set 25 mm from the 100 mm lens. Angular misalignments on this system can greatly affect the calibration of this spectrometer. To reduce these effects, a calcium fluoride diffuser was placed behind a 10 mm diameter input aperture from the plasma. The diffuser assembly was placed offset (31 mm) from the focus of the spectrometer telescope, to prevent imaging the surface roughness features of the diffuser onto the grating. The May2000Pro and optics assembly was then aligned to the plasma position with the input aperture 800 mm from the plasma. Oxygen has a high absorption in the spectral range of this spectrometer. To eliminate this in the spectrometer, the entire optical path of the spectrometer was purged with nitrogen.

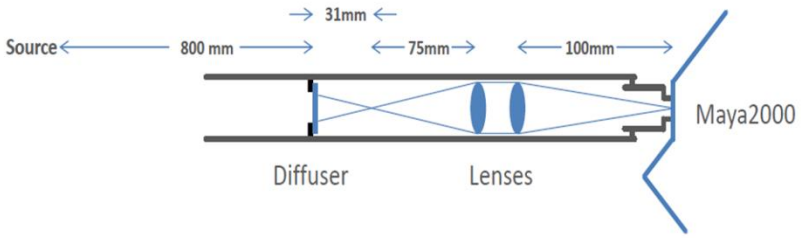

Figure 4.11: Optical layout of collection optics installed on Maya2000 Pro spectrometer

In order to calibrate the spectrometer, a 6 second integrated spectrum was captured of spectral output of a NIST traceable calibrated Hamamatsu L9841 Deuterium lamp DUV source. The lamp was placed at 500 mm from the spectrometer. To correct for the difference in distance between the spectrometer and the calibration lamp (500 mm), and the spectrometer and the plasma source (800 mm), the following function was used on the calibrated D2 spectrum.

$$E2 = E1 \times \left(\frac{500\ mm}{800\ mm}\right)^2 \qquad (4.3)$$

Using this measurement, the irradiance transfer function in Figure 4.12 was obtained. It can be seen that at wavelengths lower than 150 nm there is significant loss of signal and effects due to the low signal to noise ratio. To reduce the effect of noise a moving average function was applied to the spectrum to produce the smoothed transfer function in Figure 4.12. The smoothed transfer functions error significantly increases below 150 nm.

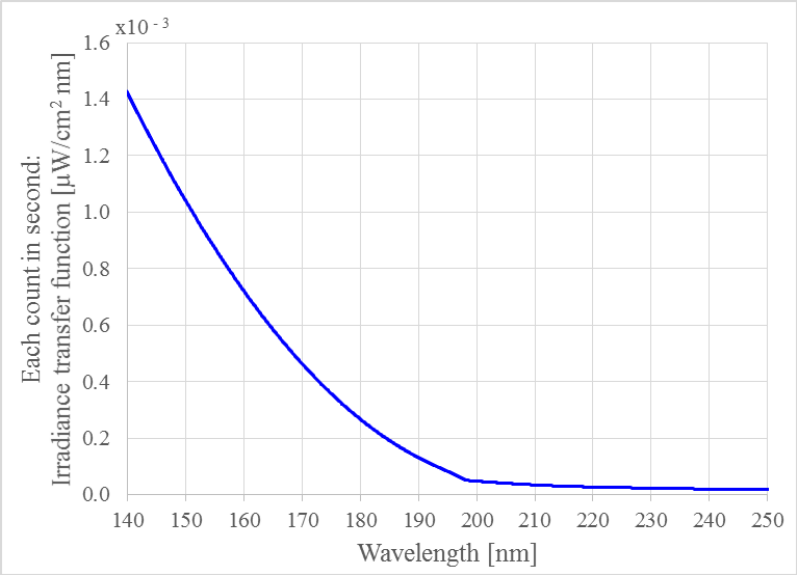

Figure 4.12: Irradiance transfer function of May2000Pro and optics assembly for 140 – 250 nm

4.2 Plasma Source Energy Measurement

For many applications a select wavelength band is desired for an application. In order to monitor the efficiency and total optical power radiated in a band, absolute calibrated wavelength measurements must be performed. While an absolutely calibrated spectrometer can perform these measurements, there are often limitations. For EUV light, absolutely calibrated sources are limited to synchrotron emission sources. Calibration of a spectrometer with these sources can not only be technically challenging, but also cost prohibitive.

In order to effectively measure absolute in-band radiation, an absolutely calibrated energy meter was used. As seen in Figure 4.13, this energy meter is composed of an aperture, a band pass filter, a narrow band reflectivity mirror, and a photodiode. The aperture limits collected light to a known area at a measured distance from the plasma, allowing for a known solid angle of radiation collected from the source. The band pass filter in addition to the narrow band filter limits the collected radiation to the in-band wavelength region to be measured. The

photodiode converts the collected photons to an electric signal that can be measured. Each of these elements will be discussed further in Sections 4.2.1 – 4.2.3. Calibration of this energy meter will be described in Section 4.2.4.

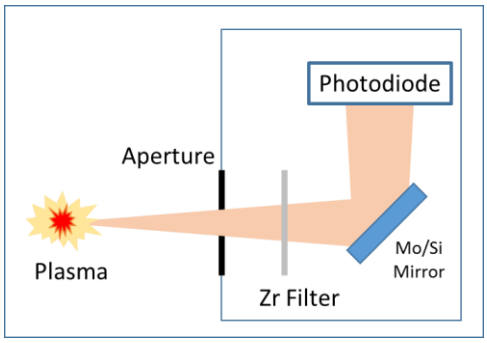

Figure 4.13: Schematic of and EUV in-band energy meter showing an EUV plasma, input aperture, zirconium foil band pass filter, a Mo/Si multilayer mirror, an EUV photodiode

4.2.1 Multi-Layer Mirror

For the EUV region of 13.5nm multilayer mirrors, as discussed in Section 1.1.1 are used to collect light from the source. These mirrors are planar 1 inch diameter by 6.25 mm Mo/Si multilayer mirrors designed for an incidence angle of 45 º. The mirror consists of 31 Mo/Si layer pairs coated on single crystal substrate, starting with the molybdenum layer, and then coated with a 3.2 nm ruthenium capping layer. The capping layer protects the layer pairs from chemically reacting with environmental oxygen. The Mo/Si pairs have a period of 10.115 nm with a molybdenum to silicon ratio of 0.39. Peak measured reflectivity of the mirror for p polarization was 63.8%. Figure 4.14 shows the measured reflectivity by NIST for a polarization factor of 0.838 and the calculated reflectivity for un-polarized light. [67]

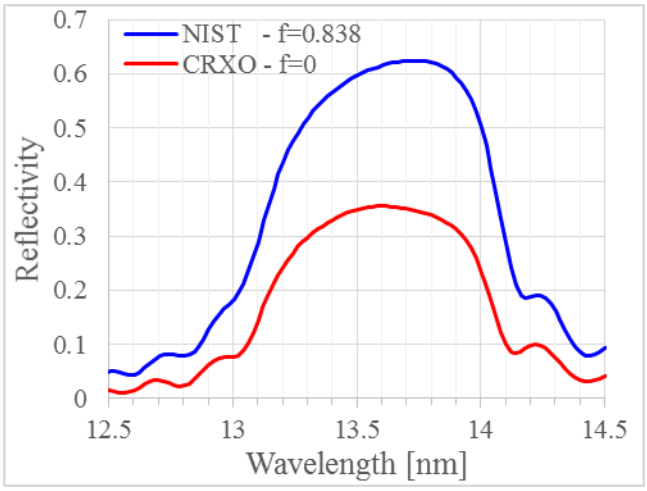

Figure 4.14: Reflectivity measurement of Mo/Si mirror for polarization factor of 0.838 calculated reflectivity for polarization factor of 0 [67]

A significant consideration in multilayer mirrors providing correct reflectivity is the incident angle. If the numerical aperture (NA) of the collected light from a point source plasma is high, then the reflectivity of the mirror can change significantly across the reflected surface. As seen in Figure 4.15 an incident angle change of plus or minus 1 º (NA=0.18) can produce significant spectral shifts in the reflectivity, with the central wavelength shifting by 0.24 nm. To reduce the effect of incident angle the EUV in-band energy meter needs to limit its NA by reducing the size of the input aperture and by placing the meter further away from the plasma source.

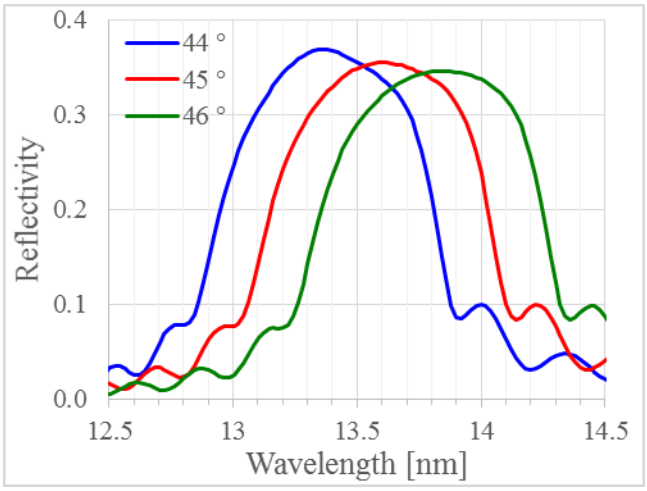

Figure 4.15: Reflectivity of Mo/Si multilayer mirror as a function of incident angle [67]

4.2.2 Photo Diode

The photodiode used in the EUV energy meter is a silicon based X-ray photo diode. Typical photodiodes have a doped region at the surface that collects free carriers produced by the photon. Photons in the EUV region are absorbed into this layer and the free carriers are lost to recombination resulting in low quantum efficiency. By moving this region to the periphery of the active area, the recombination is eliminated yielding a quantum yield of approximately 25 electron-hole pairs per photon for the wavelength of 13.5 nm. [123]

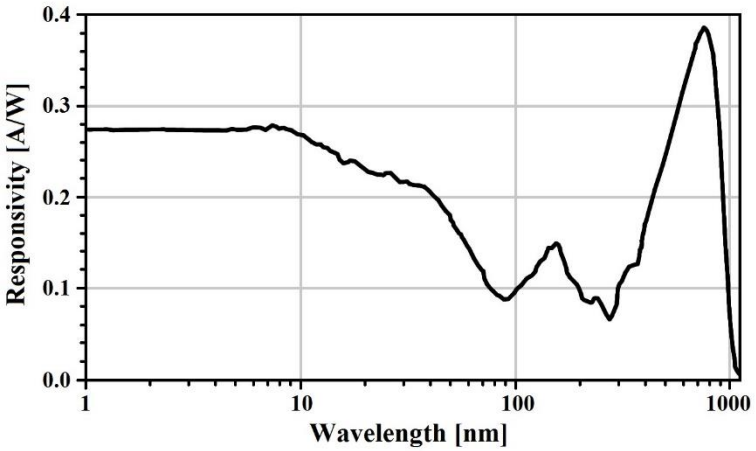

Figure 4.16: Typical responsivity of AXUV-100G photodiode for 1-1000 nm [123]

Optodiode AXUV-100G photodiodes were used in this project. It has an active area of 10 x 10 mm, that is sensitive to wavelengths from 0.0124 – 1100 nm as seen in Figure 4.16. The photodiode has a capacitance of 20 nF, a shunt resistance of 100 Mohm and a typical rise time of 10 microseconds at 0V bias. Photo emission current can contribute to the photo generated current of the photodiode. To remove this effect, the cathode of the photodiode was grounded and the signal was measured from the anode. In addition, the photodiode was biased on the anode to increase its frequency response by reducing its capacitance, and to increase the linear range of the photodiode. The signal from the photodiode was recorded with an oscilloscope. The photodiode responsivity was calibrated by NIST for 5-50 nm as seen in Figure 4.17.

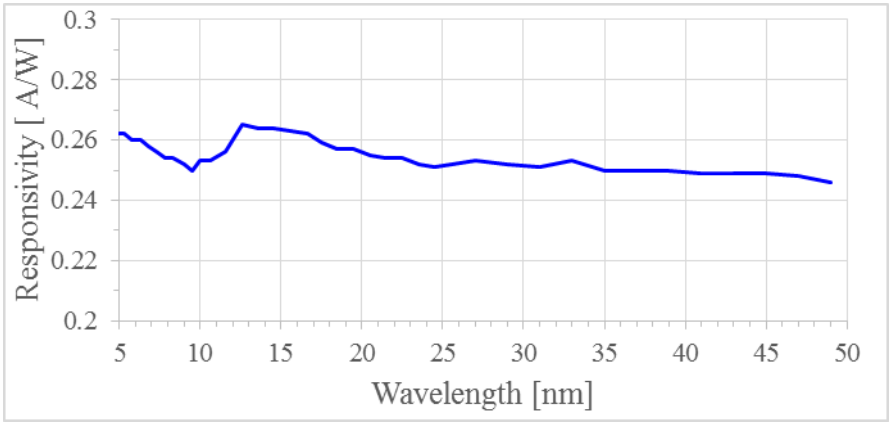

Figure 4.17: NIST calibrated responsivity of AXUV-100G photodiode

4.2.3 Filters

The silicon or ruthenium capped multilayer mirrors for 13.5 nm EUV light have high reflectivity >10% at wavelengths longer than 60 nm. [124] Additionally, the sensitivity of the AXUV-100G photodiode is significant at these wavelengths (Figure 4.13). In order to limit out-of-band radiation a band pass filter must be used. For EUV suspended metal foil filters are the only transmissive filters readily available. These filters consist of a metal foil with a thickness of less than 1 μm, suspended over an aperture. For the studies of 13.5 nm, a zirconium metal foil with at thickness of 0.5 μm, suspended over a 10 mm diameter circular aperture was used. Due to their thickness, special care is required when using these filters as small pressure changes can cause the filter to tear. The transmission, shown in Figure 4.18, limits the collected photons to 5-23 nm. Longer wavelengths are effectively blocked, being reflected by the multi-layer mirror toward the photodiode, as described in Section 4.2.1.

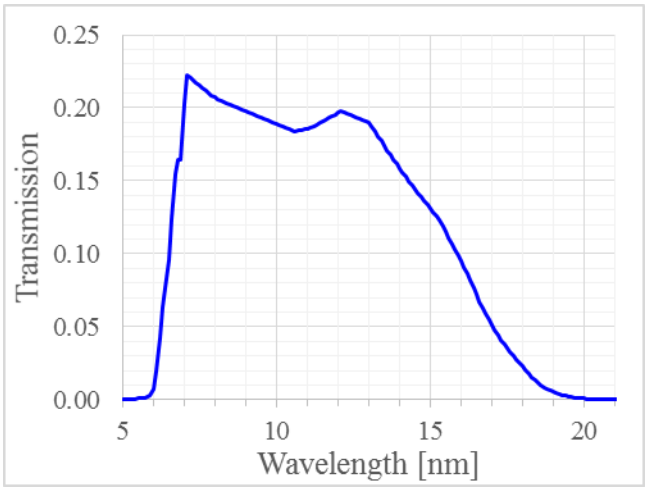

Figure 4.18: Transmission spectrum of 0.5 um zirconium metal foil filter for 5 – 21 nm [67]

4.2.4 Calibration

With each element of the energy meter calibrated the full calibrated transfer function of the optics is known, and the instruments responsivity can be calculated using the following equation,

$$\eta_{Meter} = R_{mirror}(\lambda)\eta_{diode}(\lambda)T_{filter}(\lambda) \quad (4.4)$$

where $R_{mirror}(\lambda)$ is the reflectivity of the multi-layer mirror (Figure 4.14), $\eta_{diode}(\lambda)$ is the responsivity (Figure 4.17), and $T_{filter}(\lambda)$ is the transmission of the zirconium filter (Figure 4.18). The resulting responsivity (η_{Meter}) is shown in Figure 4.19.

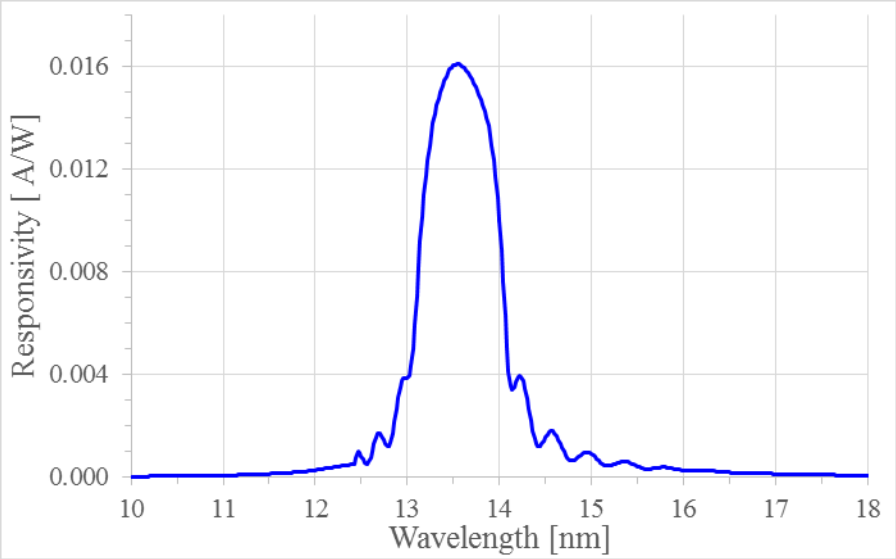

Figure 4.19: Calibrated reponsivity of the EUV energy meter from 10 – 18 nm

4.3 Gated Nanosecond Imaging

Imaging laser plasma emission at specific wavelengths provides information on the plasma shape, ionization levels, and temperature; therefore, it can be used to determine the conditions within the plasma. Furthermore, these measurements are necessary to determine the spatial extent of the plasmas emission. The plasma area measurements are critical to understanding the radiance of the source. Radiance is defined as the radiant flux emitted per solid angle per projected area. By imaging a plasma, the projected area can be determined. In this instance, the projected area can be determined by imaging the source.

In our studies of VUV laser plasma sources, a Schwarzschild optics-based, gated plasma imager was used. This imager was designed and constructed by Yuseong Jang as part of Master's Thesis [125] within the EUV program in LPL. The design of the imager, as seen in Figure 4.20, consists of a 50.8 mm diameter primary mirror with a focal length of 206.6 mm, a 12.7 mm diameter secondary mirror with a -103 mm focal length, magnesium fluoride window to support

the secondary mirror, an additional magnesium fluoride window for separating the target environment from the detector, a selectable band pass filter, and a gated intensified CCD as a detector. [125]

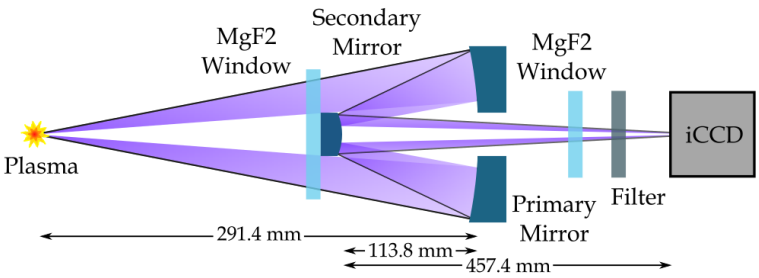

Figure 4.20: Layout of plasma imaging system

The detector in this system is a Princeton Instruments Pi-MAX3:1024i intensified CCD. The CCD provides an electronic image intensifier that allows for a signal gain of 208, and gating of the image in the nanosecond scale. The imaging system with the detector provide a plasma imaging spatial resolution of 5.52 µm. In order to select the wavelength band for imaging two interchangeable filters centered on 172 and 194 nm wavelengths were used. Calculated quantum efficiency (QE) of these filters including the transmission of the optical system and the QE of the intensified CCD is shown in Figure 4.21.

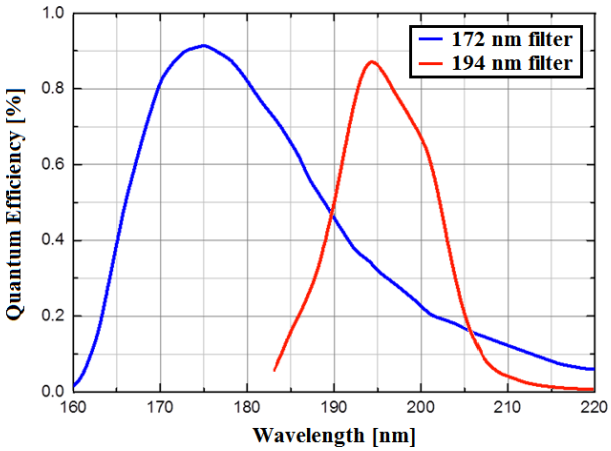

Figure 4.21: Quantum efficiency of imaging system for filters with peak wavelength of 172 nm and 194 nm

CHAPTER 5: HIGH POWER EUV SOURCE FACILITY

In order to demonstrate and investigate the characteristics of high power laser-plasmas using mass limited droplets for EUV production, a comprehensive experimental facility was developed (Figure 5.1). The main purpose of this system is to provide a stable experimental environment to measure the emission spectrum and energy of a high power, tin based, mass limited plasma source. This experimental facility, referred to as the "High Power EUV Source Facility" (HP-EUV-Facility), is composed of many integrated sub-systems. These include the following: an experimental chamber, a target delivery, high power pulsed laser, radiation focusing, and target alignment system. The systems are discussed in detail in the following sections. First the target chamber will be described including vacuum systems, laser light focusing and management. Then the target properties and delivery system will be described, including the preparation of the target solution. It is followed by a section describing the target alignment systems imaging and motion control. Next the irradiation laser and its output properties will be described. The final section will describe the attached metrology systems and their calibration.

5.1 Target Chamber

A critical component in generating EUV light, is the use of a target chamber. Since EUV radiation is absorbed in a few nanometers in atmospheric air, a vacuum environment of 10-4 Torr is required. For a high repetition rate source involving the vaporization of mass limited targets, there is a high flux of vaporized material that needs to be removed from the environment. In addition, untargeted water based droplets will boil and sublime into the environment. These by-

products all can contribute to a reduction of the collectible EUV light. A large experimental environment is required to allow for the addition of various metrological systems. In addition, the large distances (>100 cm) allow the high power plasma emission generated by the source to fall incident over the large surface area of the chamber. The heating caused by the source is effectively conducted through the chamber walls into the surrounding environment. The chamber employed in this facility is a cylindrical chamber, 1486 mm long with an inner diameter of 603 mm. It has two side ports with an inner diameter of 451 mm, which extend 393 mm from the center of the chamber. The internal volume of the chamber is ~444 liter. The following section will discuss the target chamber and systems used to maintain the vacuum environment.

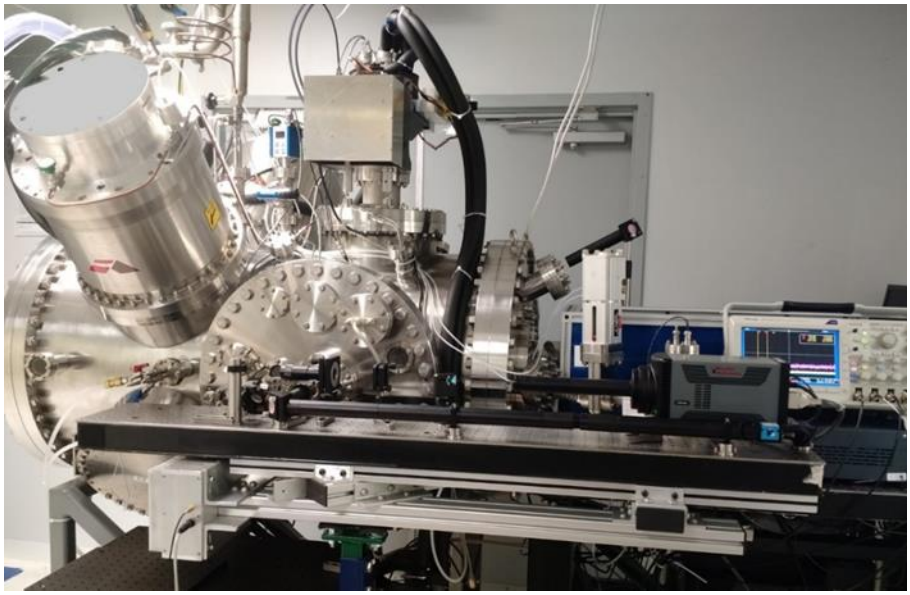

Figure 5.1: Mass limited droplet HP-EUV-Facility

5.1.1 Vacuum Systems

The environment within the target chamber is maintained at 10^{-4} Torr. The vacuum is maintained with two Osaka TG3213EMCW turbomolecular pumps, with an Alcatel ADS-1202P

Roots-type pump as a backing pump. The turbomolecular pumps were operated in parallel with their exhaust connected to the backing pumps. The Roots pump has an ultimate pressure of $3.7x10^{-4}$ Torr, with a nominal flow rate of 19167 L/min. In order to protect the pump from corrosive environmental gases the pump is purged with 35 slm nitrogen and is cooled with water at 80 L/hour. The turbomolecular pumps can provide up to 53.3 L/min each at $7.5x10^{-9}$ Torr. In order to protect theses pumps from corrosive gases, the pump is purged with 20 sccm of nitrogen gas. It is also cooled with 60 L/min of water. The nitrogen purge from the turbomolecular pump was maintained with a mass flow controller. At the exhaust port of each of the turbomolecular pumps, is a two stage valve. Each valve consists of a small valve with a flow restricting orifice, and a larger valve designed to maximize flow. When evacuating the atmospheric pressure gases from the chamber, the small restrictive valve opens starting the chamber evacuation at a flow rate under the pumping capacity of the Roots pump. After the pressure reaches $5x10^{-2}$ Torr, the larger valve opens to maximize flow at lower pressures. A schematic of the vacuum and purge systems is shown in Figure 5.2, showing the vacuum pumps, valves and control systems

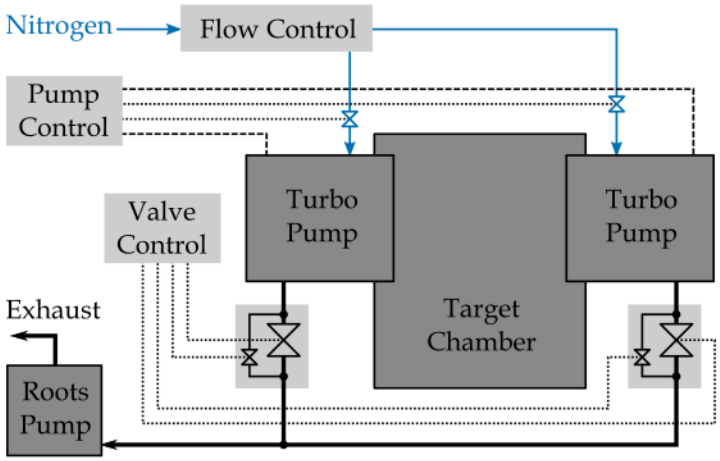

Figure 5.2 : Schematic of EUV target chamber vacuum and purge system

5.1.2 Waste Target Management

Due to the limitation of the target dispensing system (Section 5.2.2), generation of targets occurs at a faster rate than the laser pulses repetition rate. As a consequence, many of the droplets are not used for plasma formation. These mass limited targets are composed of ~86% water. At pressures lower than ~1.5x10^{1} Torr and at ambient temperature of 20 ºC, water transitions to a vapor. [126] An estimate of the pressure change per second due to vaporized droplets can be calculated using Equation (5.1), derived from the ideal gas law and the droplet target parameters. [117]

$$\Delta P_{rate} = \frac{\left[\frac{V_{droplet} \cdot \rho_{droplet}(T)}{M_{droplet}}\right] \cdot R_u \cdot T_{droplet}}{V_{chamber}} \cdot f_{droplet} \cdot p_{h2o} \qquad (5.1)$$

Here $V_{droplet}$ is the volume, $\rho_{droplet}(T)$ is the temperature dependent density, $M_{droplet}$ is the molar mass, and $f_{droplet}$ is the frequency, and $T_{droplet}$ is the temperature of the droplet target. $R_u = 62.364\ \text{Torr} \cdot \text{L/mol/K}$ is the universal gas constant, [117] p_{h2o} is the molar percentage of water in the droplet, and $V_{chamber}$ is the volume of the target chamber. Using a droplet diameter of 40 µm, a droplet temperature of 20 ºC, and a droplet frequency of 80 kHz, the rate of pressure increase (ΔP_{rate}) is 5.3x10^{-3} Torr/s. Given this rate, over time the increase in pressure can cause significant attenuation of the source emissions.

In order to prevent the rise in pressure in the chamber, a waste target collection system was developed. At a pressure of 10^{-4} Torr temperatures below -88.15 ºC water will freeze and remains solid. [126] The collection system, as seen in Figure 5.3, is cryogenically cooled to ~ -

196 °C with liquid nitrogen flowing within a cold finger. Waste droplets freeze on contact with the collection system. However, the waste targets freeze on top of one another, to form a structure similar to a stalactite. To prevent the formation from growing up to the plasma position or the dispenser, a rotary wheel was used to mechanically break the ice into the collection reservoir. The waste target material is collected in the reservoir while the chamber is under vacuum.

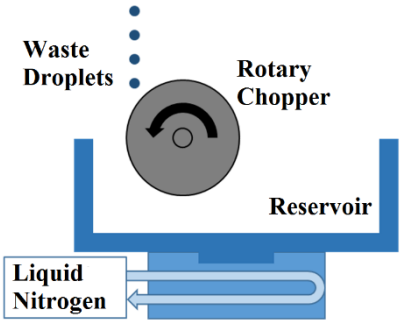

Figure 5.3: Cryogenic waste droplet collection system

5.1.3 High Power Pulsed Laser Management

The optics for managing the high power laser in the target chamber falls into two categories, focusing optics and beam dump optics as seen in Figure 5.4. In order to obtain the correct laser intensity on the target, a high numerical aperture focusing optics was required. Once the laser light passes the target position, either by transmission through the target, or by missing the target, the beam dump optics collect and disperse the energy.

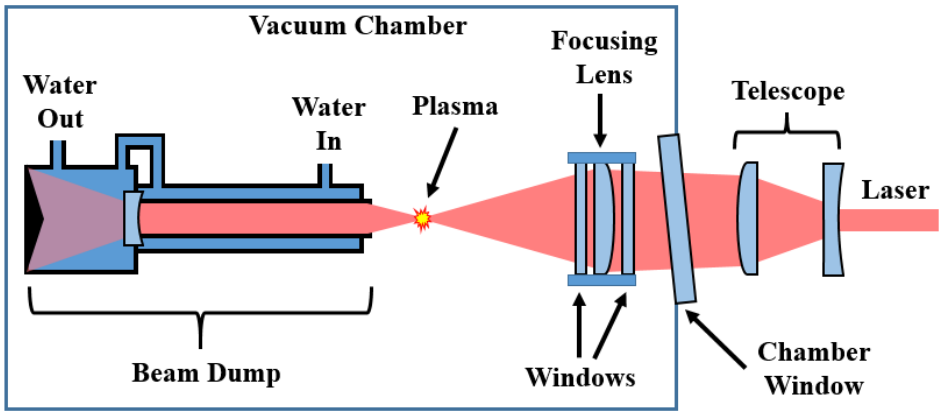

Figure 5.4: High power laser management system showing high power laser focusing optics and beam dump optics.

5.1.3.1 Focusing

Prior to entering the chamber, a Galilean telescope (Figure 5.4) expands the laser light beam with a magnification of 2.0. It is composed of a f = -150 mm plano-concave lens, and a f = 300 mm plano-convex lens separated by 150mm. Both lens 50 mm in diameter and made of UV-grade fused silica, and anti-reflective (AR) coated for 1030 nm wavelength. After the telescope is a 76.2 mm diameter by 17.7 thick, AR coated (1030 nm) window. It is tilted at 3 º to prevent the fraction of light from reflecting back to the laser.

Mounted inside of the chamber is the focusing assembly. Due to the possibility of target debris contaminating high cost focusing lenses, a sealed housing (Figure 5.4) was designed to protect the focusing lens between two lower cost planar windows. The lens is a 52 mm diameter, f = 70 mm aspherical lens. Its sealed housing holds two 50.8 mm diameter, 6.35 mm thick AR coated (1030 nm) UV-fused silica windows on either side of the focusing lens. The input window is ~7mm from the surface of the lens and the output window is ~3.1 mm from the opposite surface of the lens. The clear aperture of the housing is 44 mm. Inside of the housing

the spaces between the windows and lens is filled with air. The air in this assembly provides conduction of heat from the surface of the optics into the surrounding lens housing, thereby reducing thermal lensing. The numerical aperture of the lens assembly is 0.314.

The focusing assembly was mounted on a compact 5-axis stage, which was mounted on a motorized linear stage. Manual adjustment of the linear position perpendicular to the optical axis, and 3 rotational axes was performed with the 5-axis stage. The linear translation along the optical axis was performed with the motorized stage, providing 25.4 mm of travel along the optical axis. By having travel along the optical axis motorized, scanning of the focal point through the target is possible while the source is operational.

5.1.3.2 Beam Dump

Significant energy is deposited into the targets during the operation of the HP-EUV-Facility. Prior to alignment of the high power laser to the target, or in the event of a misalignment of the target, the full power of the laser is propagated down range from the target. If this energy is not collected safely, then scattered high power laser light will quickly heat the chamber, and can cause damage. After the target the laser light quickly expands due to the high NA. In addition, significant target debris travel down range during alignment of the source. If small diameter optics were used to collect the wasted energy, then they would quickly become coated with target debris. The accumulation of debris damages the collection optic and scatters laser light into the chamber.

To overcome the limitations of a typical designs a custom beam dump was developed. As seen in Figure 5.4 , the beam dump uses a long copper tube to reflect laser light down range

towards a diverging lens. The lens diverges the light through a water cavity onto a scatter plate. The plate scatters the light inside of the water cavity where it is absorbed. Due to the length of the copper tube the debris incident onto the diverging lens is reduced to a negligible level. Up to 4% of the laser light can be absorbed into the copper per reflection. Therefore, a significant portion of the laser energy is absorbed into the copper tube, and can melt the surface of the copper. To prevent this, a double wall was added to the copper tube to provide a jacket for cooling water to pass through.

5.2 Droplet Target

Critical to the HP-EUV-Facility is the mass-limited droplet target. Droplets are dispensed at a rate of 35 kHz. Each droplet is ~40 µm in diameter with a target-to-target spacing of ~430 um. Composed of a solution of Tin (II) chloride ($SnCl_2$), water and Hydrochloric Acid (HCl), these targets are fully ionized and therefore contribute little debris. [127] The following sections will discuss the target chemical preparation, the target dispenser, and the target temperature control.

5.2.1 Chemical Preparation

Tin (Sn) is the primary ion in producing 13.5 nm light. In order to reduce the overall mass in droplet targets, a Tin salt solution with water was developed. $SnCl_2$ is the salt used in the mass limited targets. The chemical formula is shown below.

$$SnCl_2\ (aq) + H_2O\ (l) \rightleftharpoons \mathrm{Sn}(OH)Cl\ (s) + HCl\ (aq) \quad (5.2)$$

By adding hydrochloric acid (HCl) to the solution, the above formula is unbalanced to the left side of the equation to reduce the formation of the insoluble chemical Sn(OH)Cl. First 100 ml of water is added to a beaker, and heated to ~30 ºC. 180 grams of $SnCl^2$ crystals is added to the water. A magnetic stir bar is used to mix the solution. 5 ml of 31.45% HCl solution, is added to the $SnCl_2$ solution. After the solution is fully dissolved it was filtered with a 2.7 µm pore filter, to remove any insoluble material from the solution, yielding 140 ml of solution which contains %39.5 Sn by mass, or 4.7% Sn atoms. The density of this solution is ~2 g/mL at 30 ºC. The solution at room temperature is a super saturated solution, and readily forms crystals and subsequent precipitation of $SnCl_2$. By maintaining the temperature of the solution above 30 ºC, the saturation point is raised, preventing crystal formation.

5.2.2 Dispenser Capillary

A piezo actuated capillary is used to dispense the target solution. The piezo capillary as seen in Figure 5.5, has a 10 µm inner diameter glass capillary. Target fluid entering the housing passes through a 6 µm pore sized ceramic filter. The piezo crystal is fixed to the outside of the glass capillary inside of the capillary housing with an epoxy. This piezo accepts a signal up to 1.2 MHz with a peak-to-peak voltage of 20 V. The piezo acts to create a regular induced pressure wave in the stream of the capillary. Upon exiting the capillary, the Rayleigh instability causes the liquid stream to break up at the regions of lower pressure and a regular stream of droplets is formed at the area of high pressure.

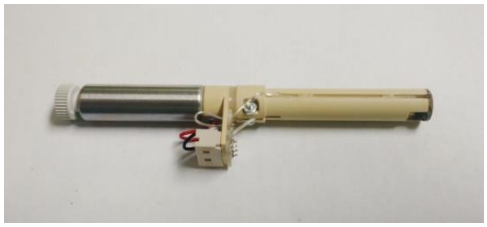

Figure 5.5: Target droplet dispencer capilary

5.2.3 Temperature Control

Crystallization of the target material due to a reduction of temperature can clog the chemical delivery system. A heating system was used to maintain the temperature along the chemical reservoir, delivery lines, and dispenser capillary. As seen in the schematic in Figure 5.6, the heating system is a circulating water system. A heat exchanger heats water in a closed loop system to 30 ºC. It is sent to the EUV target chamber within an insulated pipe, where it splits between three separate paths. One heating line wraps around an insulated reservoir where the target material is stored, and then returns to the heat exchanger. A second line goes inside the target chamber to the droplet dispensing capillary. Here, it heats the capillary and also cools the capillary heat shield. The third line flows parallel to the chemical feed line between the droplet dispenser and the chemical reservoir. The two lines are placed in close contact inside of an insulated tube.

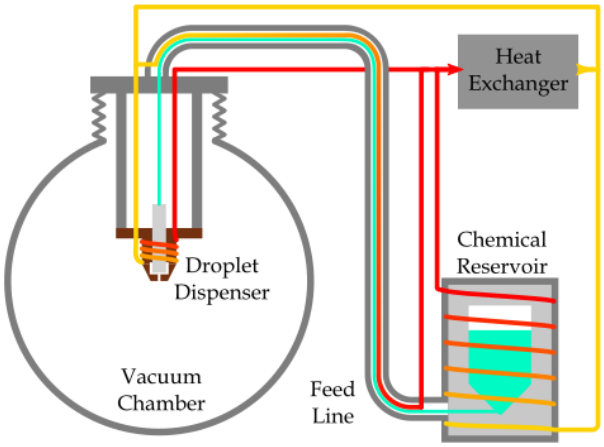

Figure 5.6: Schematic of temperateur control system for chemical dispensing system.

5.3 ADaPTS

Droplets travel through the target chamber vacuum, 25 mm from the droplet dispenser to the laser plasma position. While traveling this distance, there are many forces that perturb the droplet target. One of these forces is the droplet's interaction with remains of the previously vaporized target. This creates an uneven drag on the droplet target, causing it to drift out of position. Furthermore, plasma radiation incident on the droplet causes heating of the droplet surface closest to the plasma position. At the low vacuum pressures within the target chamber, heating of the incoming droplet causes its surface to boil and vaporize, which pushes the droplet away from the plasma position. The laser plasma also radiates charged particles. These charges repel and attract nearby droplets changing their direction. Another significant perturbation on droplet position is localized heating of the target chamber and droplet apparatus. With all of these disruptions to the droplet position, Advanced Droplet and Plasma Targeting System (ADaPTS) was developed. [114]

The ADaPTS system consists of an illumination and imaging system which captures a shadowgraph of a droplet target, positioning actuators of the droplet dispenser, the piezo driver

for the capillary, and synchronization and control system that tracts and adjusts the droplet position. A schematic diagram showing this system is shown in Figure 5.7. Here the ADaPTS system takes frequency input from the irradiation laser. It then triggers the illumination laser, which illuminates the droplet target from two orthogonal angles. The shadowgraph is imaged onto two CCDs, which is sent back into ADaPTS to determine the droplet position. Droplet position is compared with the optimal target position through a PID loop, and corrections to the droplets position and phase are adjust with outputs from ADaPTS to the droplet capillary and the translation stages. The different aspects of the ADaPTS systems are discussed further in the following sections.

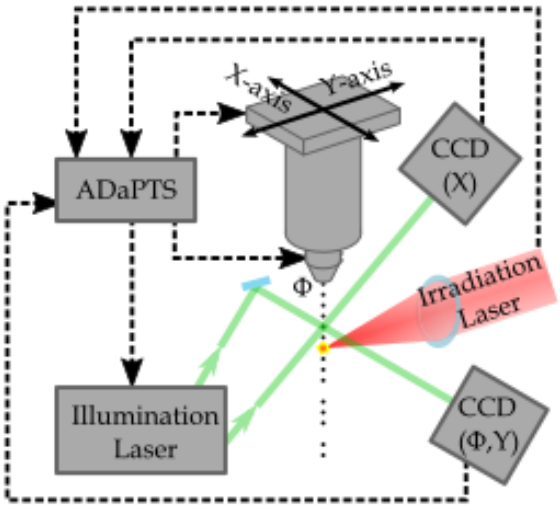

Figure 5.7: Schematic layout of ADaPTS system

5.3.1 Droplet Positioning

Positioning of the droplet target is defined by 3 orthogonal axes. The X–axis is horizontal, and perpendicular to the irradiation laser optical axis. The Y–axis is horizontal, and

aligned along the laser optical axis. The negative direction is toward the laser beam dump, and the positive direction is toward the focusing lens. The Φ–axis is vertical, and aligned with the droplet target stream. To adjust the target droplet position, the droplet dispenser capillary is adjusted by linear stages in the X and Y axes. Adjusting the Φ–axis, the phase of the droplet piezo is adjusted with respect to the laser pulses. Delaying the droplet's phase with respect to the laser positively shifts the target position up.

The X and Y linear stage for droplet positioning is a MDC Vacuum PSMA-4004, which provides 20 mm of travel in each axis. They are actuated using a 4 tread per inch ACME tread rotated by a Probotix HT23-280-8 stepper motor, which pushes an ACME nut attached to the linear stage. The stepper motor has 200 steps per revolution with 16 micro steps, for a total of 3200 micro steps per revolution. The holding torque of these motors is 2 Nm, which prevents slipping of the motor position. The X, Y position accuracy of these motors is 2 microns. The stepper motors are driven by a Changzhou RATTM Motor Co USB6560T4 controller, which provides up to 3 Amps of current to the stages.

The phase of the piezo in the droplet capillary is adjusted by switching three different cocks into a divider, which triggers capillary piezo. To advance the phase, which has the effect of shifting the droplet position down from the plasma position, the clock is switched to a 50 MHz clock from the main 20 MHz clock. For a delay in phase, which has the effect of shifting the droplet position up from the plasma position, the clock is switched from the main 20 MHz clock to a 12.5 MHz clock. After the droplet reaches the correct position with respect to the laser pulse the clock is switched back to the 20MHz clock. For the experiments discussed in this thesis, the clock is divided to a 35 kHz piezo driving frequency.

5.3.2 Imaging

The imaging system for ADaPTS is shown in Figure 5.8. Here, a 1064 nm DPSS laser beam is split into two optical paths. These optical paths cross orthogonally 5 mm above the target position, illuminating untargeted droplets. The illuminated droplets are imaged onto a CCD camera using a 3X microscope.

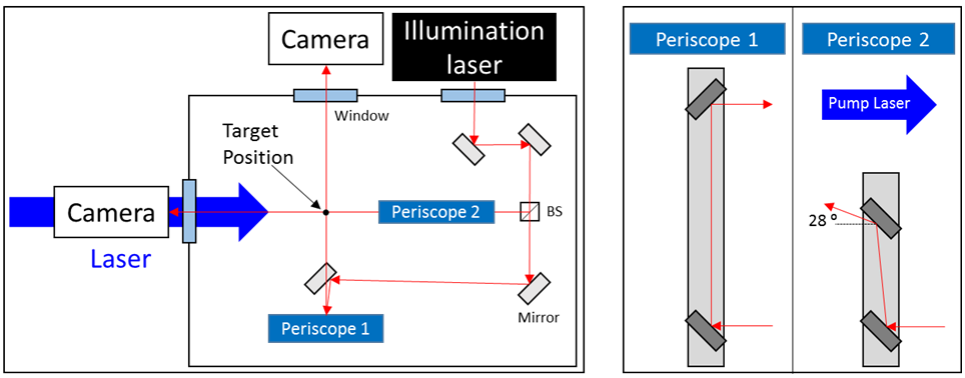

Figure 5.8: Schematic of ADaPTS imaging system showing illumination laser, optics, and camera

The DPSS illumination laser has an average power output of 100 mW and a maximum frequency of 100 kHz. At frequencies below 5 kHz the pulse width is 65 ns, and ~100 ns for the frequency range of 20 – 100 kHz. The gain material in the laser is a 3x3x4 mm Nd:YVO_4 with a 0.5% neodymium doping. It is pumped by a 3 W TEC cooled 808 nm diode. On the pump side of the gain medium an AR coating at 808 nm and an HR coating at 1064 nm, which acts as the back mirror in the cavity. The opposite face of the gain medium is AR coated for 1064 and 808 nm. The output coupler for the cavity has a 95% reflectivity, with a 30 cm radius of curvature. To pulse the laser an AOM was added inside of the cavity for Q switched operation.

Pulses from the laser are directly triggered by the ADaPTS control system, and are synchronized with the droplet repetition rate. Output from the laser is passed into the chamber

through a window AR coated for 1064 nm. Inside the target chamber the illumination laser light is routed to the droplet imaging position using 1064 nm HR mirrors (Figure 5.8). After illuminating the droplets, a shadowgraph is imaged onto a CCD using the optics system shown in Figure 5.9. These lenses are Thorlabs AR 1064 nm coated, and include a plano-convex f = 125 mm lens (LA1986), plano-convex f = 250 mm lens (LA1461), plano-concave f = -75 mm (LC1852) lens, and a meniscus f = -300 mm lens (LF1015). The microscope has a 1064 nm notch filter to prevent plasma radiation, and 1030 nm light from the high power laser from imaging to the CCD. The working distance of this microscope is 584.2mm, with a magnification of 3X.

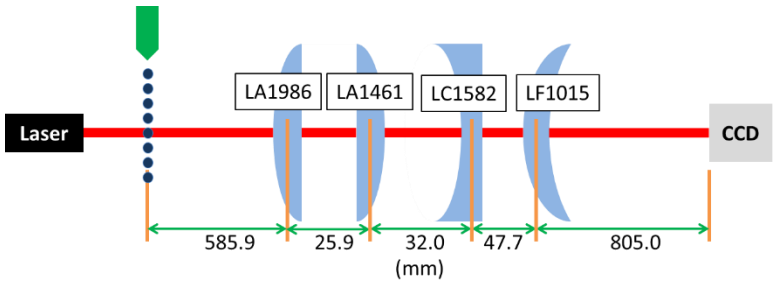

Figure 5.9: Layout of imaging optics for ADaPTS system

At the imaging plane a DMK23U618 (The Imaging Source) CCD recorded the image at a rate of 120 frames per second, at a resolution of 640 x 480 pixels. The pixel size of the CCD is 5.6 µm, which provides an object plane resolution of ~2 µm. The image captured by this imaging system is used by the ADaPTS system to calculate the centroid of the droplet from the image. By spreading the droplet image over larger number of pixels, a larger number of data points can be used when computing the centroid. To enable this, the imaging optics were adjusted to provide an object plane resolution of ~53.8 µm.

5.3.3 PID control

The ADaPTS system used to control the droplet position in these studies is controlled with a proportional-integral-derivative (PID) controller. The system determines the error in the droplet position in each axis. The value of the error is multiplied by a proportional (P) constant. Over a time interval, the error value is integrated and multiplied by the integral constant (I). The accumulation of error over time contributes to a larger value with this term. The derivative of the value is multiplied by the derivative constant (D). The value is proportional to the slope of the error over time, the term increases with high system velocity, and contributes to quicker settling of the corrective values. All of these terms are summed for each axis and the corrective value output to the system. The process repeats to maintain the target position. The representative equation is shown below.

$$u(t) = P \cdot e(t) + I \cdot \int_0^t e(t)\,dt + D \cdot \frac{de(t)}{dt} \qquad (5.3)$$

5.4 High Power Laser

Providing the correct laser light parameters to the mass-limited target is critical for efficient EUV light generation. The high power laser used for these studies was the TRUMPF TruDisk 8000. This laser provides a maximum average power of 2 kW, a maximum pulse energy of 100 mJ at a wavelength of 1030 nm, and a pulse width of 34.4 ns FWHM. At 100 mJ the maximum pulse repetition rate is 20 kHz. At reduced pulse energies of 20 mJ the laser can achieve 100 kHz pulse repetition rates. The minimum repetition rate that this laser can operate at

is 5 kHz. The measured beam parameter product of the laser was ~5 mm·mrad, and the beam diameter was 5 mm at the output mirror.

The laser is a thin disk type laser with a cavity dump design. The gain medium in the laser is an Yb:YAG thin disk, which is pumped by a laser diode array. The emitted light at 1030 nm circulates in the laser cavity and builds until it reaches the selected energy. At this point, a Pockels cell in the cavity switches the polarization, so that it passes through a polarizer in the cavity. This laser design provides high average power and high pulse energy. However, this design adds challenges to synchronization of this laser with droplet and imaging systems. Due to the cavity dump style optical cavity if the energy is left to build in the cavity past the deigned energy level, then optical damage of the optics will occur. To prevent this, a photodiode internal to the laser monitors the cavity energy and triggers the Pockels cell to dump the energy when the next system clock cycle occurs. For this reason, the laser pulses cannot be externally triggered. To synchronize the HP-EUV-Facility to the laser, the laser was treated as the master clock. A digital TTL clock signal is provided by the laser, which has the same frequency of the laser pulses. The laser pulses have a 50 ns jitter with respect to the TTL signal.

Working with this high power laser of this type requires several considerations. The first considerations are the necessary facilities such as electrical power, chilled water systems, and laboratory space required for operation and servicing of the laser. This laser operates on a 460V 3-phase 75kVA electrical feed. In order to install this laser in the HP-EUV-Facility electrical power then it was necessary to install a 208V/460V power transformer. Facility chilled water needs to provide 20 L/min at 65 °C to deliver adequate cooling. The laser has external dimensions of 199 x 155 x 120 cm (width x height x depth). To acuminate the required space for

this laser, the laser was installed in a neighboring laboratory, with an optical feed through path between the laboratories.

The combined high average power and high pulse energy required careful consideration of stray light management and optical damage. At the first mirror in the optical path of the laser, the beam diameter is approximately 5 mm, resulting in an average intensity of 10.2 kW/cm^2 and a peak intensity of ~15 MW/cm^2. At these intensities high quality optics with high damage thresholds are required. To reduce stray light, mirrors must have high reflectivity. With 0.02 % transmission of the reflected beam from high reflectivity (HR) mirrors used in this work, the leaked beam could have an average power of 0.4 watts, resulting in an average intensity of 2 watts/cm^2 and a maximum peak intensity of 3 kW/cm2. At these intensities, leaked light can cause damage to absorptive materials. To mitigate safety risks associated with this light beam blocks were installed behind the HR mirrors. When the laser is focus onto a droplet target in the HP-EUV-Facility, the laser light may not be fully absorbed into the target, or may miss the target all together. This transmitted light must be collected and dissipated to prevent damage to the facility. A water cooled beam dump, described further in Section 5.1.3, was installed to collect unused laser light.

5.4.1 Laser Metrology

In order to optimize a laser plasma and to understand the irradiance conditions of the laser plasma formation, precise measurements of the laser characteristics were obtained. Key measurements include time resolved laser irradiance on target, laser spot spatial intensity distribution, and transmitted unabsorbed laser energy. To measure time resolved irradiance of the laser, the fraction of light (0.02 %) leaked through a high reflectivity mirror in the laser optics

was measured using a silicon photodiode. As seen in Figure 5.10, the average laser pulse energy was measured using two calibrated energy meters. One for reflected laser light (position A), and one for the transmitted fraction of the laser light (position B). The energy meter in position A and B was removed and a photodiode assembly was installed after position B. The photodiode assembly (Figure 5.10) consists of a several neutral density filters, a lens, and Thorlabs DET10A photodiode. The neutral density filters are selected to reduce the maximum input laser signal to a level below the saturation of the photodiode. A 100 mm focal length lens is used to focus the input beam onto the 1 mm diameter photodiode. The electrical signal from the photodiode is recorded with a digital oscilloscope providing a 1 ns signal rise time.

To monitor the beam profile of the high power laser, a lens was used to image the laser special profile onto a CCD, Figure 5.10. Neutral density filters were added to reduce the signal intensity under the saturation of the CCD. The imaging of the beam profile occurs after the last mirror before laser focusing lens. Placing the imaging system here allows detection of changes in alignment and deleterious effects of the optics prior to the plasma source target chamber.

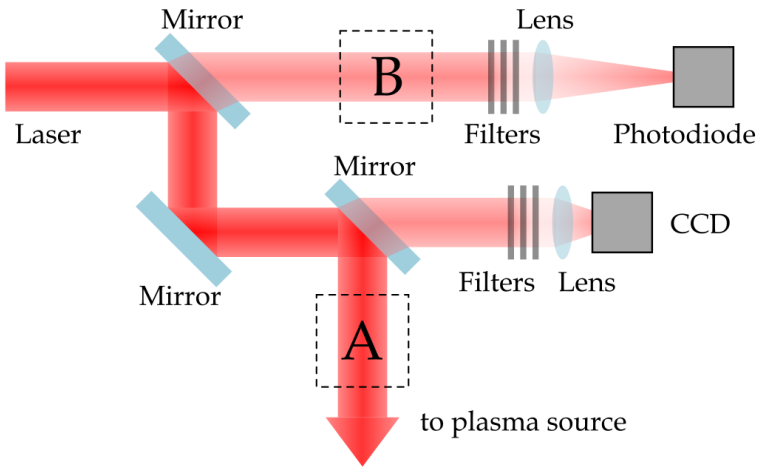

Figure 5.10: High power laser energy measurement

To determine the fraction of laser light that is not absorbed or scattered by the target, either by transmitting through or by the target. A Thorlabs DET10A photodiode was added to the beam dump, just before the diverging lens in the beam dump (Figure 5.4). Here the spatial distribution of the laser light is effectively homogenized and a fraction of the laser light can be measured. By measuring fully transmitted and fully blocked laser light, an effective measurement of unused laser energy can be obtained. An oscilloscope was used to capture the signal from this photodiode. The recorded signals were normalized to the 100 % transmitted signal provided by fully misaligned target to the laser. Measurements from this photodiode provide a measurement to determine alignment of the laser with the plasma target, and provides an estimate of the laser light not used in forming the laser plasma.

5.4.2 Laser Pulse Shape

The pulse shape of the laser was measured using the metrology described in Section 5.4.2. As seen in Figure 5.11, the pulse shape shows three key regions. The region highlighted in red, which is called the foot of the pulse, is light leaked from the cavity through the polarizer prior to the Pockels cell switching. The first 226 ns part of the pulse contains 2.6 % of the pulse energy. The green highlighted region is the main pulse. It has a pulse width of 34.4 ns FWHM. The pulse has significant energy after the peak, which is called the tail. This region is 147.6 ns long and contains 35.2 % of the pulse energy in a region, highlighted in blue.

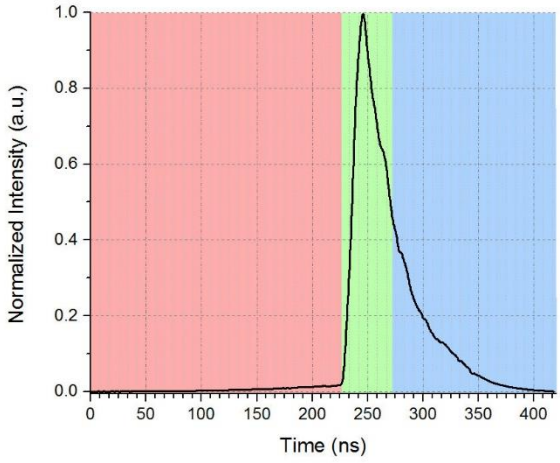

Figure 5.11: Measured pulse shape of TruMicro 8000 laser.

5.4.3 Calibration

Measurement of conversion efficiency (CE) from laser energy into the bandwidth of the collection optics is required to judge effectiveness of the HP-EUV-Facility. CE is calculated, from measurements from the EUV spectrometer and energy meter, over 2π sr into 2% bandwidth at 13.5 nm (13.365 – 13.635 nm) of the Mo-Si multi-layer mirrors. Calibration of the metrological equipment using the well know methods outlined in [128], [129], [130] to provide absolute measurement of CE, are outlined below.

The in-band energy collectable by the Mo-Si mirror is defined as,

$$E_{2\%BW} = \frac{\int_{all} I_0 I_s(\lambda) R_{mirror}(\lambda)\, d\lambda}{R_{mirror}(\lambda_{max})} \qquad (5.4)$$

where I_s is the relative spectral intensity measured by the EUV spectrometer in arbitrary units, $R_{mirror}(\lambda)$ is the reflectivity of the Mo-Si mirror (Section 4.2.1), λ_{max} is the wavelength of peak

reflectivity, and I_0 is the normalization factor change relative spectral intensity to the absolute scale. The normalization factor is calculated by, [128]

$$I_0 = \frac{2\pi}{\Omega \cdot R_{scope} \int_{all} I_s(\lambda) T_{gas}(\lambda) R_{mirror}(\lambda) T_{filter}(\lambda) \eta_{diode}(\lambda)\, d\lambda} \quad (5.5)$$

where Ω is the collection solid angle of the energy meter (Section 5.5), R_{scope} is the impedance of the oscilloscope in Ohms, T_{gas} is the transmission function of the atmosphere in the optical path of the energy meter, T_{filter} is the transmission of the Zr filter (Section 4.2.3), $\eta_{diode}(\lambda)$ is the responsivity of the EUV photodiode (Section 4.2.2), A_{scope} is the integrated area under the measured signal from the EUV energy meter in V·s. It is defined as,

$$A_{scope} = \int V(t)\, dt \quad (5.6)$$

By combining Equation (5.4) and Equation (5.5) the in-band energy can be calculated as,

$$E_{2\%BW} = C \cdot A_{scope} \quad (5.7)$$

where C is defined as,

$$C = \frac{2\pi}{\Omega \cdot R_{scope} \int_{all} I_s(\lambda) T_{gas}(\lambda) R_{mirror}(\lambda) T_{filter}(\lambda) \eta_{diode}(\lambda)\, d\lambda} \frac{\int_{all} I_s(\lambda) R_{mirror}(\lambda)\, d\lambda}{R_{mirror}(\lambda_{max})} \quad (5.8)$$

By calculating C for a given source spectrum, for a specific irradiance condition. The CE can be quickly calculated over 2π sr into 2% bandwidth at 13.5 nm,

$$CE = \frac{E_{2\%BW}}{E_{laser}} = \frac{C \cdot A_{scope}}{E_{laser}} \quad (5.9)$$

All calculations of CE for EUV light studies in this thesis were performed using the above methods.

5.4.4 Beam Profile

Single shot beam profile of the laser was measured using the CCD described in Section 5.4.2. Based on these measurements, this laser has two mode distributions as seen in Figure 5.12. The laser oscillated between these two energy distributions. These distributions are likely due to competing gain within the cavity between two pulses. When measuring laser intensity with a photodiode, care was taken to measure the whole mode area. Clipping of the imaged laser spot on the photodiode by its aperture, can cause shot to shot relative measurement errors as high as 30 %.

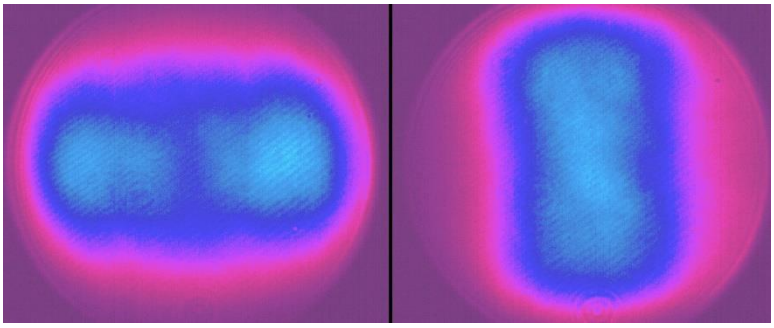

Figure 5.12: Measured ocillating beam profiles of the TruMicro 8000 laser

The beam profile was also measured at the plasma position. Here, the change in mode profile does not make measurable changes in the distribution. At the focus position the laser spot size was 45 μm FWHM.

5.5 Metrology

Two metrological devices were used in this system to measure plasma emission. For high resolution spectrum in the EUV region a grazing incident Harada style spectrometer, as described in Section 4.1.2.2, was used. The position of the CCD in this spectrometer was fixed, to capture spectrum for 10.5 – 18 nm. The second metrological device was the absolutely calibrated energy meter, as described in Section 4.2. Each instrument was fixed at 28 ^{o} horizontally from the pump laser optical axis, as seen in Figure 5.13. The input slit of the EUV spectrometer is 849.2 mm from the plasma position, and the input aperture of the EUV energy meter is 527.4 mm from this position. An input slit of 73 μm, on the EUV spectrometer provide a numerical aperture of 4.3×10^{-5}. The input aperture of the energy meter has a diameter of 6.35 mm, providing a collection solid angle of 1.14×10^{-4} sr.

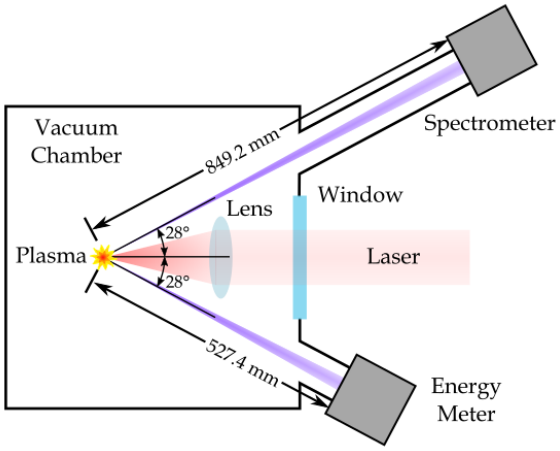

Figure 5.13: Schematic layout (top view) of EUV spectrometer and energy meter on target chamber

5.6 Emission Spectrum of Liquid Droplet Laser Produced Plasmas

Spectra for water droplets were generated using the TRUMP TruMicro 8000 laser (Section 5.4). The laser spot size was 50 µm, with a repetition rate of 5 kHz. The droplet size was 40 µm with a repetition rate of 20 kHz. Several laser intensities were used: $5.0x10^{10}$, $8 x10^{10}$, $1x10^{11}$, $1.3x10^{11}$ W/cm^2, $2x10^{11}$ W/cm^2, $2.3x10^{11}$ W/cm^{2,} and $2.6x10^{11}$ W/cm^2. The spectra shown in Figure 5.14, was acquired with the EUV Harada spectrometer for a spectral range of 12.7 – 20 nm. Strong line emission from oxygen, arising from the charge states O VI and O V have peaks at 13.15, 15.07, 15.89, 17.21, 18.137, 18.57, 19.3, and 19.9 nm.

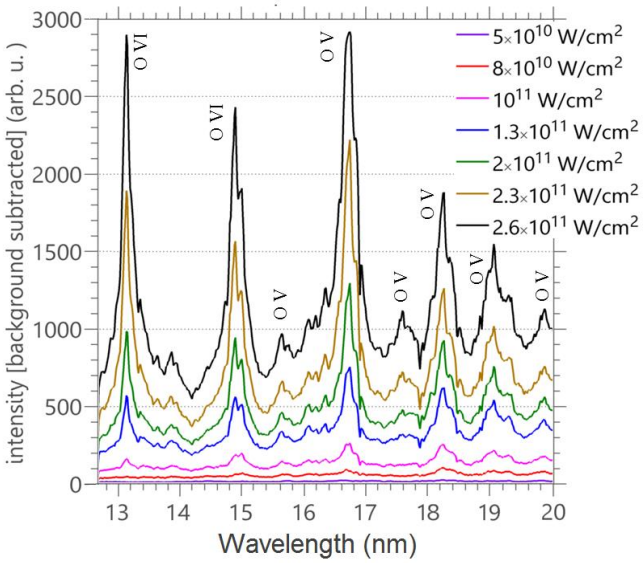

Figure 5.14: Emission spectrum of water droplet source for several laser intensities

Spectra for mass limited tin (Sn) based droplets were generated using the same laser as for the water droplets. The droplets were composed of $SnCl_2$ solution in water, with 39.5 % Sn by mass. The laser spot size was 50 µm, with a repetition rate of 5 kHz. The droplet size was 45 µm with a repetition rate of 35 kHz. Several laser intensities were used: 0.9×10^{10}, 1.1×10^{10}, 1.3×10^{11}, 1.4×10^{11} W/cm^2, and 1.6×10^{11} W/cm^2. The spectra shown in Figure 5.15, was acquired with the EUV Harada spectrometer for a spectral range of 10.5 – 17.5 nm. Emission lines from the charge states O VI and O V are visible at 11.4, 13.15, 15.07, 15.89, and 17.21 nm. The peak of the UTA emission from tin is located at 13.8 nm. The shift of the peak emission from the in-band emission suggests that for these conditions, the intensity on target was lower than optimal.

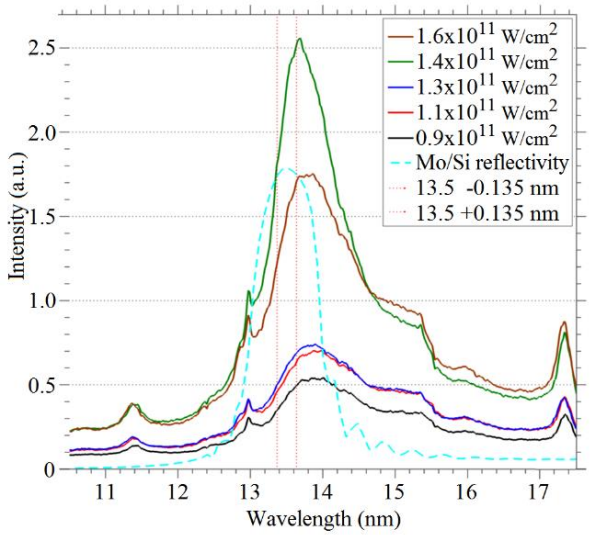

Figure 5.15: EUV Spectrum of mass limited Tin droplet source for several laser intensities, with Mo/Si mirror reflectivity in a.u.

CHAPTER 6: VUV METROLOGY SOURCE FACILITY

For investigation of VUV sources, as well as out-of-band (OOB) emission for EUV sources, an experimental plasma source is needed that can provide a wide range of experimental conditions. Additionally, absolute calibrated spectroscopy across the 125-250 nm VUV range is vital for understanding these laser plasmas. Different target geometries, as discussed in CHAPTER 3, have many benefits and disadvantage depending on the application. This requires an experimental system that can accommodate various target types. Emission in the VUV region encounters many different absorption bands from atmospheric gases; therefore, control of the environmental gases is critical. An experimental facility (Figure 6.1), referred to as the "VUV Metrology Source Facility" (VUV-MS-Facility) was designed and built to measure absolute calibrated broadband spectrum of the plasma emission, while providing an adjustable environmental pressure for various gases, a wide range of laser irradiation parameters, and variable target geometries. The facility provides broadband spectral measurements across the 22 – 250 nm wavelength range. This system was absolutely calibrated across the 125 – 250 nm wavelength range. With this system, absolute broadband plasma emission can be recorded for a diverse range of plasmas. Furthermore, the facility provides nanosecond resolved imaging provides measurement of the plasma emission size, which can be used to determine the collectable light of the source.

The VUV-MS-Facility is composed of many sub-systems including, experimental chamber, irradiation laser focusing, target alignment system, several interchangeable target systems, two laser systems to provide a range of laser intensities and pulse durations, and suite of metrology systems. These systems are discussed in detail in the following sections. First the

target chamber will be described including gas management systems, irradiation laser properties and focusing optics, and attached metrological systems. It is followed by a section about the calibration of the spectrometers. The irradiation lasers used in the experimental studies will be described in the following section. Then the gas target delivery system will be described, including the positioning system, and emitted spectrum. The next section discusses solid planar target system including its alignment system and motion control, target mounting, and emitted spectrum. Next the lasers used to generate and irradiate the plasmas and their output properties will be described. The final section will describe the attached metrology systems and their calibration.

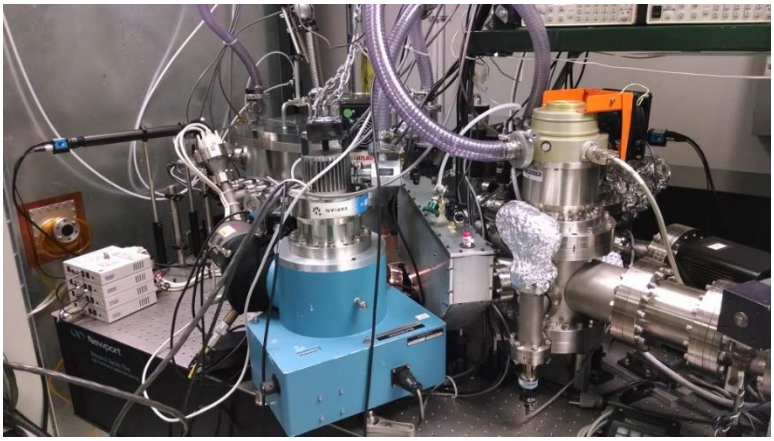

Figure 6.1: VUV-MS-Facility

6.1 VUV Target Chamber

In order to maintain optimal environmental conditions for the VUV-MS-Facility, while providing multi-angle options for metrology, a multi-port vacuum chamber was used. The shape of the chamber, is a truncated cylindrical section, as seen in Figure 6.2. The chamber is designed around a central plasma point which is 97.2 mm above the floor of the chamber. With an overall

chamber height of 254 mm. The large flat wall of the chamber opposite of curved surface, is 43.18 mm from the plasma position, and is 696.5 mm long. The curved surface has an inner radius of 482.6 mm, with the centroid as the plasma position. On its curved side it has 11 ports aligned to the central point with a 10 º interval, for a total angular coverage of 110 º. These ports are all aligned to the central plasma position. The internal volume of the chamber is ~83 L. The floor of the chamber is a 23 mm thick plate of metal with ½-20 threaded holes in a 25.4 inch grid. This allows optical elements to be securely secured in place, with minimal deflection as the pressure of the chamber changes.

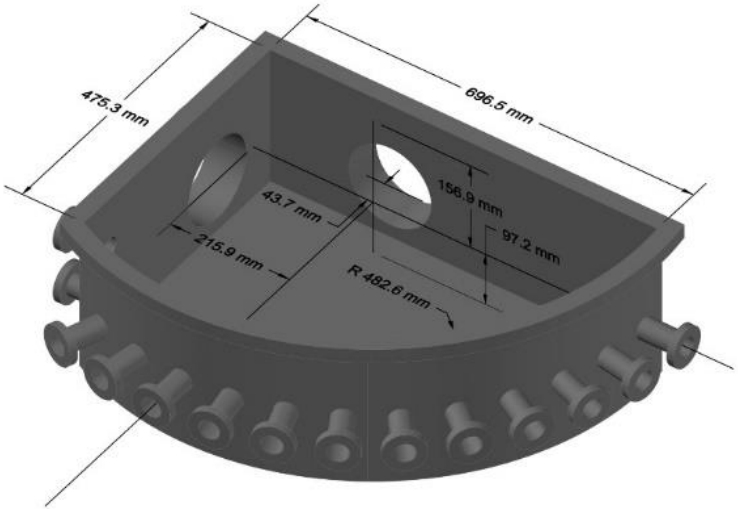

Figure 6.2: Layout of VUV target chamber

6.1.1 Gas Management Systems

Controlling the environmental gases of the VUV-MS-Facility is critical to prevent absorption of plasma emission. With planar targets the target chamber is maintained at 10^{-4} Torr. The vacuum in maintained with a Varian Turbo-V 551 Navigator turbomolecular pump, with an Alcatel ADS-1202P Roots pump as a backing pump. The turbomolecular pump were operated in

parallel with the turbo pumps of the spectrometers, and in series with the Roots pump. The Roots pump has an ultimate pressure of $3.7x10^{-4}$ Torr, with a maximum flow rate of 19167 L/minute. The pump is connected to the turbomolecular pump through 1 inch PVC pipe. The turbomolecular pump can provide up to 550 L/s each at $1x10^{-10}$ Torr. It is cooled with 5 l/m of water. At the exhaust port of the turbomolecular pump, is a manual vacuum valve. When evacuating the atmospheric pressure gases from the chamber, the valve is partially opened to reduce the initial flow of gas out of the chamber. After the pressure reaches $1x10^{-1}$ Torr, the valve is fully opened and the turbomolecular pump can start the final pump down to the experimental pressure

With gas targets there are two types of gas plasma, high pressure (>10 Torr) bulk gas plasmas, and high pressure gas jet plasmas. For bulk gas plasmas the target chamber is evacuated using the above vacuum systems. Once the chamber is evacuated the chamber is purged with the target gas to flush the remaining atmospheric gases from the turbomolecular pump. Then the valve of the pump is closed and the pump is turned off. Once the pump stops, the chamber is filled to the desired pressure using a metering valve. Care was taken to make sure that the gas feed lines were evacuated prior to pressurizing with the target gas. The pressure is measured using a Varian Multi-Gauge convection gauge which can measure to 10^{-3} Torr. Depending on the target gas, the measurement of the gauge is corrected using published correction factors. [131] For gas jet targets the chamber was evacuated using the above vacuum systems. However, to maintain a low pressure (<10 Torr) environment around the high pressure (>760 Torr) gas jet, the turbomolecular pump was left operating to remove the inflow of target gas. The gas pressure at the gas jet was maintained using a metered valve.

For spectrometers measuring spectra for wavelengths from 5 – 125 nm additional turbomolecular pumps are required for maintaining the low pressure environment. At these wavelengths there are no transmissive optics, and therefore there are no transmissive windows to prevent target gas from entering the spectrometer. For the VUV Harada (Section 4.1.2.1) a turbomolecular pump was added to the grating chamber (Figure 4.6). The EUV Harada (Section 4.1.2.2) also had a turbomolecular pump added to its grating chamber. The exhaust of these turbomolecular pumps were connected in parallel to the target chambers backing pump. A limiting aperture was added between the target chamber and these spectrometers to limit the flow of gas into the spectrometer while having a large NA to fully illuminate the input slit with the laser plasma emission. The pressure in each spectrometer was maintained below 10^{-4} Torr.

6.1.2 Pulsed Lasers

Two different pulsed lasers were used with the VUV-MS-Facility in the experiments described in this thesis. For high intensity laser pulses a Spectra Physics Quantaray GCR-190-100 was used. It provides a maximum average power of 35 W, a maximum pulse energy of 350 mJ at 100 Hz, with a wavelength of 1064 nm, and a pulse width of 10 ns. It is a flash lamp pumped, Nd:YAG, Q-switched unstable resonator laser. The optical cavity of the laser from the HR mirror to the output coupler, is composed of a HR mirror, wave plate, Pockels cell, polarizer, first flash lamp cavity with a Nd:YAG rod and two flash lamps, quartz polarization compensator, second flash lamp cavity with a Nd:YAG rod and two flash lamps, and a Gaussian HR coated output coupler. Each flash lamp cavity has two flash lamps. In order to achieve 100 Hz operation, each lamp in a flash lamp cavity takes turns pumping the cavity at 50Hz with 10 ms delay between the lamps. When the Pockels cell triggers an increase in cavities Q, laser light

generated in the cavity oscillates between the HR mirror and the center of the output coupler where the mirror has 100% reflectivity. As the light diverges from the optical axis toward the low reflectivity edges of the output coupler the light leaks out of the laser cavity, and diffracts around the Gaussian mirror, to form a top hat intensity distribution. The beam diameter at the far field of the laser is 8mm.

For this laser, the beam profile and beam pointing changes with flash lamp energy, and pulse to pulse stability is reduced at lower flash lam energies. For these reasons, the laser is designed to operate at a full flash lamp energy. To operate in this stable regime and have pulse energy adjustment, a light valve was used to attenuate the energy of the pulses. The light valve, as seen in Figure 6.3, consists of a horizontally polarized thin film polarizer which removed vertically polarized light from the beam due to thermal depolarization in the laser cavity. Following this is a half-wave plate that when rotated, rotates linear polarization of the transmitted light rotates by 2 times the angle of the crystal axis. With a rotation of 45 º the polarization is vertically polarized. After the wave plate, there is another horizontally polarized thin film polarizer. Which removes the vertically polarized fraction of light from rotated linear polarized light, and directs it into a beam dump. The optical system effectively attenuates the energy of the beam without changing the alignment or profile of the laser beam on target. The laser was focused using a 25.4 mm diameter 60 mm focal length GRADIUM® lens. The focal spot size at the laser plasma target was 20 μm FWHM in diameter. With this spot size the light valve was used to vary the intensity on target from $1.6x10^{10}$ – $2.2x10^{12}$ W/cm^2. For lower intensity measurement on solid targets, the lens was brought closer to the target for a spot size diameter of 400 μm FWHM. At this spot size the laser intensity was adjusted between $1.6x10^{8}$ –

$11.6x10^{10}$ W/cm^2. An energy meter and a photodiode captured a leaked part of the laser beam to provide metrics on laser energy and pulse shape to determine the laser intensity.

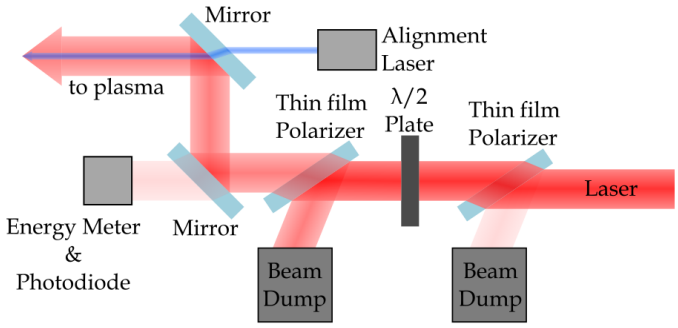

Figure 6.3: Light valve and laser metrology for 100 Hz laser

The Spectra Physics Quantaray laser allows for external independent triggering of the flash lamps and Pockels cell. This allows for synchronization of the laser with the VUV-MS-Facility. By adjusting the delay between the flash lamps and Pockels cell the efficiency of the laser can be tuned.

The other laser used with the VUV-MS-Facility, to provide a higher pulse repetition rate and to study the effect of pulse width on laser plasmas was the IPG YLP-HP-25-100-20-500-EQ fiber laser. The laser is an ytterbium pulsed fiber laser, which provides a maximum average power of 500 Watts at 1064 nm, with an adjustable repetition rate of 2 – 50 kHz, a maximum pulse energy of 42 mJ at 11.9 kHz, and a maximum average power of 500 W. The pulse width of the laser can be set to 60, 100, 250, and 500 ns. The laser has a top hat intensity distribution with an output beam diameter of 10 mm. An advantage of this laser over the Quantaray laser, is that it maintains its beam profile and pointing stability during changes in energy, frequency, and pulse width settings. Therefore, a light valve to attenuate the laser was not necessary. In this configuration, the same mirrors, alignment beam, and the focusing lens were used in Figure 6.3;

however, the thin film polarizers, beam dumps, and the wave plates were removed. The spot size at the laser plasma target was 200 μm FWHM in diameter, providing an intensity range of $4.9x10^6 – 1.3x10^9$. Unlike the Quantaray laser described above which has analog potentiometers to control laser energy, the IPG laser has a software interface that allows the user to set parameters such as laser frequency, pulse energy, and pulse width. This interface provides calibrated output energy from the laser, so the laser power monitor shown in Figure 6.3 was not used. This laser allows for external triggering of laser pulses.

6.1.3 Metrology

A suite of metrological tools was attached to the ports across an angular range of 40 º, as seen in Figure 6.4. Covering the 250 – 5 nm range are four spectrometers. For measuring absolute spectral intensity in the 150 – 250 nm range, the Maya200 Pro UV spectrometer, as described in Section 4.1.3, is aligned to the plasma at a 50 º angle from the irradiation laser. For the absolute spectral intensity in the 170 – 110 nm region, the Seya-Namioka style spectrometer ("McPherson"), described in Section 4.1.1, is aligned to the plasma at a 60 º angle from the irradiation laser. The VUV system also has two relatively calibrated spectrometers. Measuring the 22 – 124 nm range is the VUV Harada spectrometer, as described in Section 4.1.2.1, this spectrometer is aligned at a 40 º angle from the irradiation laser. For the 5 – 20 nm region the EUV spectrometer, described in Section 4.1.2.2, is aligned to the plasma at an angle of 30 º from the irradiation laser. In addition to the spectrometers, a nanosecond gated plasma imaging system, described in Section 4.3, records plasma images. Imaging optics for this imager is located in the target chamber, with the iCCD and wavelength filter located outside of the target

chamber separated by an MgF2 optical window. The optical axis of this imaging system, is aligned to the plasma at an angle of 70 º from the irradiation laser.

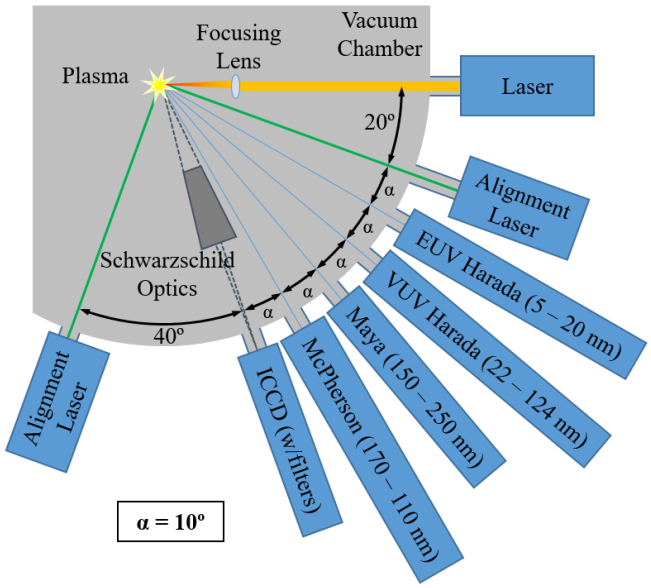

Figure 6.4: Layout of the VUV-MS-Facility's spectrometers, imaigng system, irradiation laser, and alignment lasers

Alignment of these metrology devices was aided by the use of two orthogonal 532 nm, 1 mm diameter alignment beams, a 1mm diameter 632.8 nm laser beam coaxial to the irradiation laser and several alignment tools. The two 532nm beams originate from one 15 mW laser passed through a 50/50 beam splitter. These two beams are aligned into the chamber using mirrors external to the chamber. Located in the center of the chamber 12.7mm mount was installed. Into this mount, two different alignment tools were installed. The first tool is a frosted glass disk with a 1 mm hole. This tool rotates in the 12.7 mm mount with the 1 mm hole at the center of rotation. At each input port of the target chamber, 444.5 mm from the plasma location, is an adjustable 1 mm iris through which the alignment beams pass. When these beams are able to pass through the frosted glass alignment tool with minimal scattered light, the 532 nm beams are orthogonal and

cross at the plasma position. In addition, the irradiation laser alignment beam is 20 º and 110 º with respect to the 532 nm alignment beams. The alignment error of this tool, assuming a 10% beam to aperture overlap, is ~0.013 º. The second alignment tool is a planar mirror mounted with the rotational axis of the 12.7 mm mount in the plane of the mirror. When this mirror is placed so that the incident angle is 45 º for both of the 532 nm alignment beams, each beam counter propagates along the same path as the other alignment beam, however in the opposite direction. When these beams return to the 50/50 beam splitter, 50% of each incident beam is projected onto an alignment card. When the beams overlap with an error of less than 10% beam diameter. The angular alignment error is 0.002 º. This provides an alignment error at the plasma position of less than 17 μm. By rotating the mirror so that the 632.8 nm alignment beam passed through the iris of the 110 º green beam path, a similar alignment could be performed for the irradiation alignment beam. Continuing this same technique to reflect one of the 532 nm alignment beams through the alignment iris of each metrology device and verifying that this transmitted beam passed through the optics into the spectrometer, the alignment of these devices could be verified

6.2 Spectral Calibration

Calibration of the spectrometers used on the VUV-MS-Facility, were calibrated using a NIST traceable Hamamatsu L9841 deuterium (D2) lamp. It emits across 115 – 400 nm wavelength. The lamp has a source aperture of 0.5 mm in diameter, and a flat calibrated irradiance profile across a solid angle of 0.006 sr at a distance of 500 mm. To block the effects off scattered light by the lamp housing a 5mm aperture 8 mm from the source aperture was used It was measured that the irradiance spectrum of the D2 lamp varies with angle. To minimize this effect several fixed apertures were fixed to the lamp to transmit only the central portion of the

emitted light. Additionally, the L9841 D2 lamps spectrum varies by its temperature. To maintain the lamp temperature, forced air at 20 °C was used to cool the lamp. The spectral irradiance of the D2 lamp was absolutely calibrated at a distance of 500 mm as a secondary source using a Seya-Namioka style spectrometer which was calibrated using PTB synchrotron source calibrated D2 lamp as a primary source. This primary source had a calibration error of +/-7% for the wavelength range of 114 – 165 nm, and +/-5% in the 165 – 410 nm range

The D2 lamps was mounted on a rotary stage so that the center of its source was at the axis of rotation. The assembly was then mounted so that D2 lamp's source was centered at the laser plasma position. Final alignment of the D2 lamps was performed by rotating the D2 lamp with the rotary stage until the emission was centered on through each spectrometer alignment iris (Section 6.1.3). Prior to each spectral acquisition, a tube was installed between the output of the D2 lamp and the spectrometer. The tube was purged with argon for 15 minutes until the nitrogen and oxygen were expelled. As seen in Figure 6.5, the transmitted unpurged spectrum varies greatly (red) vs the purged spectrum. Air totally absorbs the spectrum below 180 nm, with absorption lines from 180 – 195 nm. At longer wavelengths oxygen molecular bonds are broken by photo-ionizations. When these ions recombine a significant quantity recombine to form ozone (O_3). Ozone causes absorption starting at 205 nm, with increasing absorption till 240 nm where the light is fully absorbed. [132] Over time the buildup of ozone increase, causing the absorption in this region to increase.

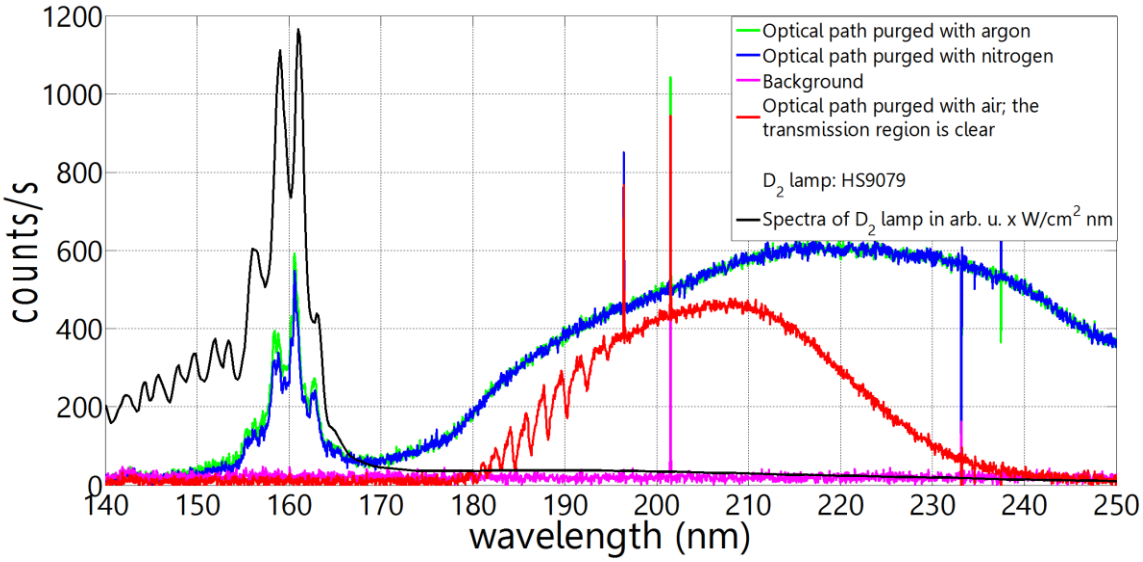

Figure 6.5: Calibrated deterium lamp emission spectrum, compred to un-calibrated spectra captured by Maya 2000 spectrometer under varius conditions.

With the D2 lamp and purge tube aligned to each spectrometer and purged with argon for 20 minutes, the background spectra were then obtained for each spectrometer with the D2 lamp off. Background spectra was integrated for several different time frames corresponding to the integration time of each laser plasma spectrum. The D2 lamp was then turned on and left idle with forced air cooling for 15 minutes, while the lamp temperature and emission spectrum stabilized. Acquired D2 spectra was integrated for 6 seconds for the Maya 2000 spectrometer, 60 seconds for the McPherson spectrometer, and 60 seconds for the VUV Harada. The irradiance transfer function was calculated for these acquired spectra from the calibration data for the D2 lamp. Due to the numerous spectral peaks present in the D2 lamp from 115 – 165 nm, spectral artifact from these peaks were present in the irradiance transfer function. To compensate for these, a smoothing function was applied to the transfer function in order to remove these spectral artifacts. The resulting irradiance transfer functions are shown in Figure 4.3 and Figure 4.12.

The wavelength range of the McPherson spectrometer was spectrally calibrated across the 123 -165 nm range, using emission lines including the Lyman-α emission line of Hydrogen (~121.5 nm), Oxygen emission lines of O IV (~ 134.29 nm), O V (~ 137.12 nm), and lines of the D_2 lamp at ~159 nm and ~161 nm. Using these spectral line positions and regression, in addition to,

$$\lambda = a_1 + a_2 p + a_3 p^2 + a_4 p^3 \quad (6.1)$$

where λ is the wavelength of pixel p, a_1 is the wavelength of pixel 0, a_2 is the first coefficient (nm/pixel), a_3 is the second coefficient (nm/pixel^2), and a_4 is the third coefficient (nm/pixel^3). The coefficients for the McPherson central grating position of 145 nm are, $a_1 = 1.23 \times 10^2$, $a_2 = 6.01 \times 10^{-2}$, $a_3 = -4.20 \times 10^{-5}$, and $a_4 = 2.26 \times 10^{-8}$. For a central grating position of 115 nm they are, $a_1 = 1.1 \times 10^2$, $a_2 = -2.03 \times 10^{-2}$, $a_3 = -6.6 \times 10^{-5}$, and $a_4 = -1.9 \times 10^{-8}$.

When processing the acquired spectra from the laser plasma, first the background spectrum was subtracted from the spectrum. For McPherson spectrometer, the background subtracted spectra was wavelength calibrated using the above method. Then the spectra were calibrated for absolute irradiance using the spectrometers respective smoothed irradiance transfer functions (Figure 4.12 and Figure 4.3).

6.2.1 Spectral Measurement Error

Sources of error in spectral calibration of the D2 lamp, as well as the spectrometers used on the VUV-MS-Facility, arise from many sources. These leads to errors in absolute spectral

irradiance measurements presented in this work. The most common sources of measurement error are calibration errors arise due spectral drift during lamp operation, as well as errors of lamp alignment during calibration, and temperature fluctuations of the lamp.

During operation, the temperature of the D2 increases until it reaches a steady state. When the lamp is left to convectively cool it can reach temperatures as high as 50 °C. At these temperatures the lamp is considered overheated and the plasma emission is affected. Wavelengths less than 135 nm the irradiance of the overheated lamp can increase by as much as 2 times. Across the wavelength range of 125 – 159 nm, the irradiance of the lamp decreases by as much as 50%. In addition, D2 lamps have several emission lines between 115 – 128 nm that ratios by many times with the Lyman Alpha emission line at 121.6 nm changing the most, reducing by 4 times. To prevent these calibration errors it is important to use a forced air cooling (Section 6.2) to maintain the bulb temperature at 20 °C during the calibration of the bulb and when using it to calibrate a metrology device.

D2 lamps used in this work typical have a flat irradiance at 500 mm from the source, over a 1 mm diameter area. Outside of this spot the D2 lamp emits significant spectral power over 2π sr solid angle. Calibration of this spot is highly sensitive to misalignments. At angles of greater than 1 degree the change in irradiance be reduced as much as 60%. To reduce this, an angular alignment of less than 0.1 degrees is required to maintain a +/- 10% error. To verify alignment of the D2 lamp to the spectrometer the lamp was rotated about the source position to verify that the peak irradiance is centered on the spectrometer.

When obtaining spectra from a calibrated D2 lamp with a spectrometer the signal to noise ratio (SNR) of the recorded spectra can greatly impact the accuracy of the subsequent calibration of the spectrometer. For example, when the SNR is less than 2 the calibration error can be more

than 2 times. Due to the SNR issue, the McPherson (Section 4.1.1) wavelengths lower than 133nm, and the Maya2000 (Section 4.1.3) at wavelengths lower than 176 nm can expect measurement errors of +/- 100%.

By including the SNR measurement error and calibration errors due to possible misalignment, and calibration lamp drift, the total measurement error can be estimated. Figure 6.6 shows the estimated measurement error for the spectra obtained by McPherson and Maya2000 spectrometers. For the McPherson, the measurement error is +/- 17% for 137 – 165 nm wavelength band. As the wavelength decreases the wavelength error increases to +/- 100% at 133 nm and shorter. The Maya2000 has a measurement error of +/- 15% for 187 – 250 nm wavelength band. As the wavelength decreases the wavelength error increases to +/- 100% at 176 nm and shorter.

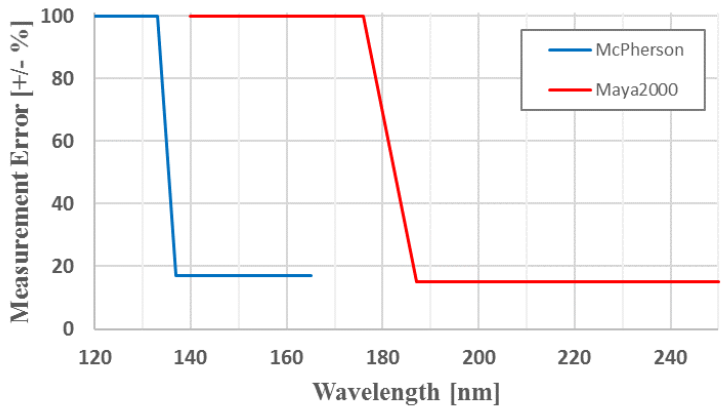

Figure 6.6: Estimated measurement error of McPherson and Maya2000

6.3 Gas Jet Laser Produced Plasma

In order to investigate possible gas target laser plasma source, a gas jet system was designed to provide, a limited plasma size, and high gas densities. One of the advantages of this

system, is that high densities are possible without the need of a pressure chamber. The purpose of this system was to investigate emission properties of several gases, argon, krypton, and xenon. These gases were chosen because of their many possible electron transitions, and inert chemical properties. For these studies the Spectra Physics Quantaray GCR-190-100 laser as discussed in Section 6.1.2 was used to irradiate these gases. The target chamber was maintained at 10^{-4} Torr. At this pressure, the residual atmospheric gas concentration in the target chamber where, $\mathrm{Ar} = 3.1\mathrm{x}10^{10}$, $\mathrm{O} = 1.4\mathrm{x}10^{12}$, $\mathrm{N} = 5.2\mathrm{x}10^{12}$, $\mathrm{C} = 1.0\mathrm{x}10^{9}$ atom/cm^3. While some of these atoms will become ionized in the laser plasma and will contribute to the obtained spectrum, their concentration is significantly lower than the densities of the gas jet on the order of 10^{19} atom/cm^3.

6.3.1 Gas Capillary

The gas target capillary as seen in Figure 6.7 was used to generate a gas jet. The capillary was made of glass with an inner diameter is 230 µm. The glass capillary was inserted into a copper plate with hole matching the outer diameter of the capillary. The capillary was then glued into the copper plate using vacuum compatible epoxy, to seal the capillary into the copper plate. This copper plate was then clamped in place of the gasket in a VCR® fitting of a 5 um inline filter, providing a high vacuum seal. Between the filter and the copper plate. The filter was then connected to the gas supply line feed through on the chamber.

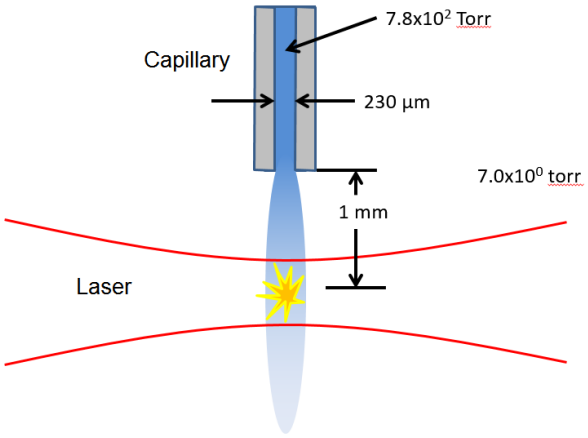

Figure 6.7: Layout of gas jet capilary

The target chamber, gas supply line, and capillary assembly, were evacuated using the turbomolecular pump discussed in Section 6.1.1. When a pressure of 10^{-4} Torr was reached a high pressure gas was applied to the capillary. A pressure was chosen, to provide a high enough density of gas to form a measurable laser plasma, while also providing a mass flow lower than the vacuum pumping capacity.

The highest ion density in a gas jet is closest to the capillary; however, the capillary tip is exposed to high radiation flux from the laser plasma. The absorption of this light causes the capillary tip to heat causing deformation and in some cases, melt. In order to prevent this the capillary was positioned 1mm from the laser focus. At this distance, the solid angle of the capillary tip is small enough that the absorbed energy can be safely conducted through the capillary mount.

6.3.2 Positioning Apparatus

In order to position and align the gas capillary to the plasma position. A 3-axis linear stage was used. Two horizontal stages (X and Y) were motorized with a total linear travel of 25

mm and minimum repeatable step size of 2 μm. The vertical stage (Z) provided 10 mm of travel with a manual micrometer adjustment. The capillary assembly was mounted to the 3 axis stage. Once the capillary was installed, a small threshold plasma was created in atmospheric air. The capillary tip was brought within 1 mm of this plasma position vertically and a rough alignment was performed. The chamber was then evacuated and a supply of nitrogen was applied to the capillary. With the gas jet in operation, the laser intensity was increased until a plasma could be observed. At these conditions, the visible emission increases with the density of gas. The capillary was scanned along one of the horizontal axis until the plasma emission was at its highest. The same was repeated with the orthogonal horizontal axis. Once the high visible emission had been achieved, the capillary was aligned to the laser plasma position. The chamber, gas feed line, and capillary were then evacuated and the target gas was applied.

6.3.3 Emission Spectra

Emission spectra for argon, krypton, and xenon were obtained plasma formed by the Spectra Physics Quantaray GCR-190-100 laser (Section 6.1.2). The intensity of the laser at the plasma position was $2x10^{11}$ W/cm^2. For gas spectra, a non-smoothed irradiance transfer function Figure 6.8 was used for calibrating the spectra obtained from the Maya 2000 Pro spectrometer (Maya). For wavelengths below 155 nm the transfer function has significant sharp lines. These lines results from the low signal emitted by the D2 lamp, and the low sensitivity of the Maya. Here the signal to noise of the acquired spectra was very low. At wavelengths from 155 – 165 nm the line artifacts, as discussed in Section 6.2, are present in the transfer function.

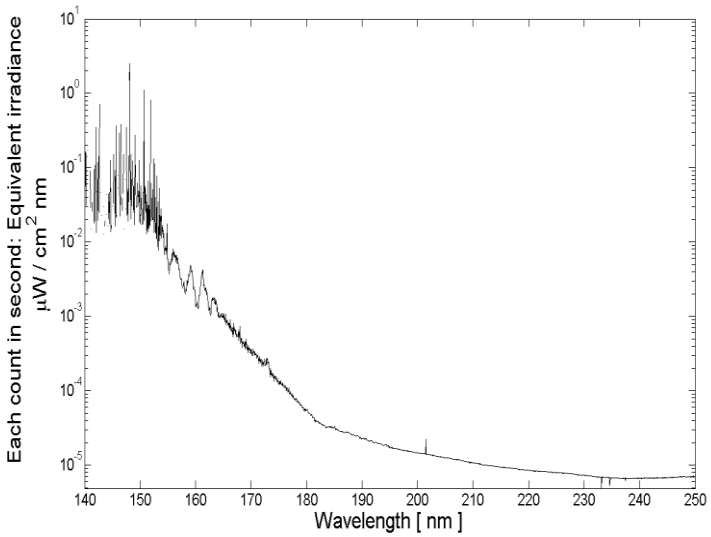

Figure 6.8: Maya 2000 non-smoothed irradiance transfer function used for argon, krypton, and xenon

A non-smoothed irradiance transfer function Figure 6.9 was also used for calibrating the spectra obtained from the McPherson spectrometer. At wavelengths shorter than ~130 nm the line artifacts, as discussed in Section 6.2, are present in the transfer function. They are also present in a 10 nm band centered on 160 nm.

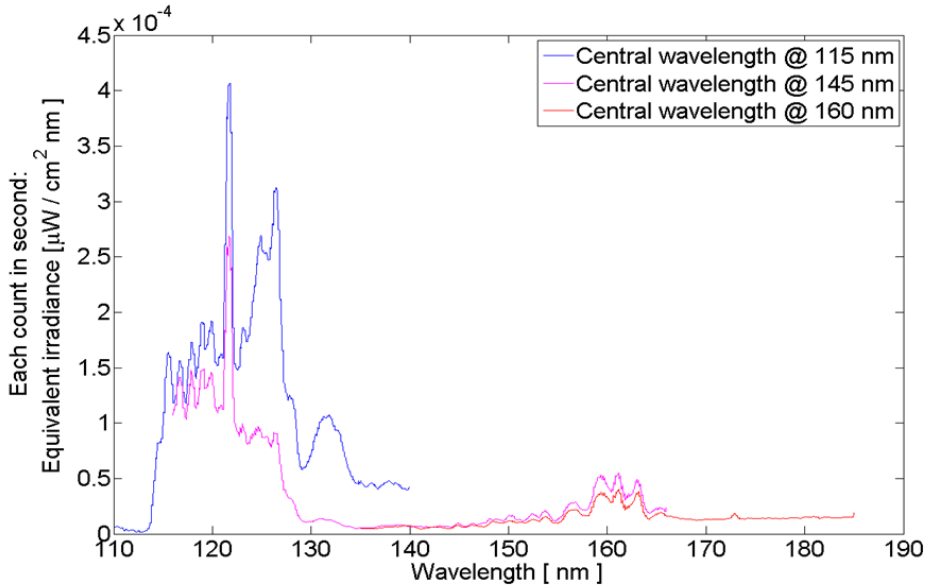

Figure 6.9; McPherson non-smoothed irradiance transfer function, for grating positions of 115, 145, and160 nm

6.3.3.1 Argon

Argon did not produce a strong enough signal to use a gas jet at longer wavelengths, due to the limitation of 6 second integration time of the Maya 2000. None the less, in order to obtain a stronger signal, the chamber was filled with argon at a pressure of 863 Torr, to provide a plasma with a larger target volume. This provides a larger etendue and provides a stronger signal. Figure 6.10 shows the acquired spectrum from the Maya 2000 with an integration time of 6 seconds, calibrated with the transfer function from Figure 6.8. In this spectral range, there is a strong spectral line at 173.8 nm with an irradiance of 0.015 $\mu W/cm^2 \cdot nm$. In addition, there are several lines less 0.002 $\mu W/cm^2 \cdot nm$ at 192.7, 218, 231.6, and 242.4 nm. The sensitivity of the Maya 2000 renders the spectrum unresolvable at wavelengths below 170 nm.

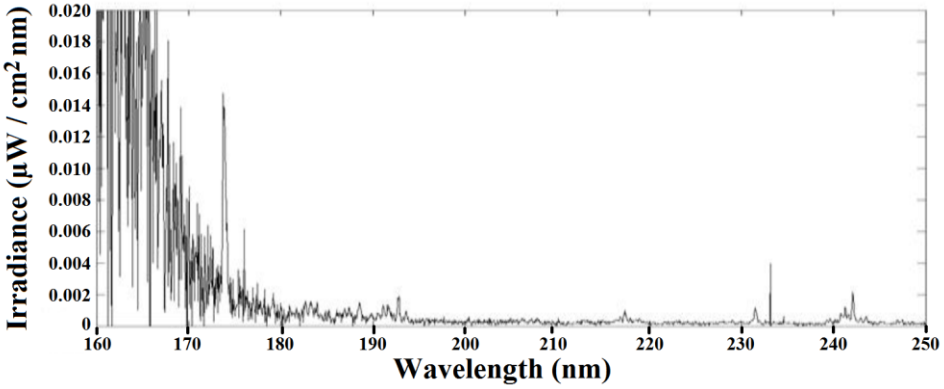

Figure 6.10: Spectrum of argon for 160 - 250 nm captured with Maya 2000

The McPherson acquired spectrum at the same time as the Maya. Figure 6.11 shows the acquired spectrum from the McPherson with an integration time of 600 seconds, calibrated with the transfer function from Figure 6.8. There are two strong peaks in this range. The Lyman-alpha peak at 121.5 nm with an irradiance of 0.63 $\mu W/cm^2 \cdot nm$ and one at 123.2 nm with an irradiance of 0.8 $\mu W/cm^2 \cdot nm$.

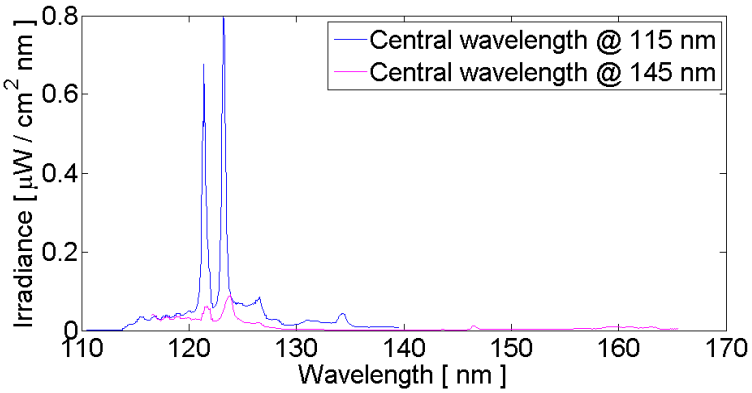

Figure 6.11: Spectrum of argon for 115 - 170 nm acquired with McPherson

6.3.3.2 Krypton

Due to the limitation of 6 second integration time of the Maya 2000 and krypton's low emission at longer wavelengths a gas jet could not be used to obtain spectra. To obtain a stronger

signal the chamber was filled with krypton, at a pressure of 863 Torr. This gas condition provides a larger target area, providing a stronger signal with the larger etendue. Figure 6.12 shows the acquired spectrum from the Maya 2000 with an integration time of 6 seconds, calibrated with the transfer function from Figure 6.8. In this spectral range, there is a strong spectral line at 196.4 nm with an irradiance of 0.0075 $\mu W/cm^2 \cdot nm$. In addition, there are several lines less 0.001 $\mu W/cm^2 \cdot nm$ at 192.8, 208.6, 228, 231.4 nm, and 235.1. Below 170 nm the sensitivity of the Maya 2000 renders the spectrum unresolvable.

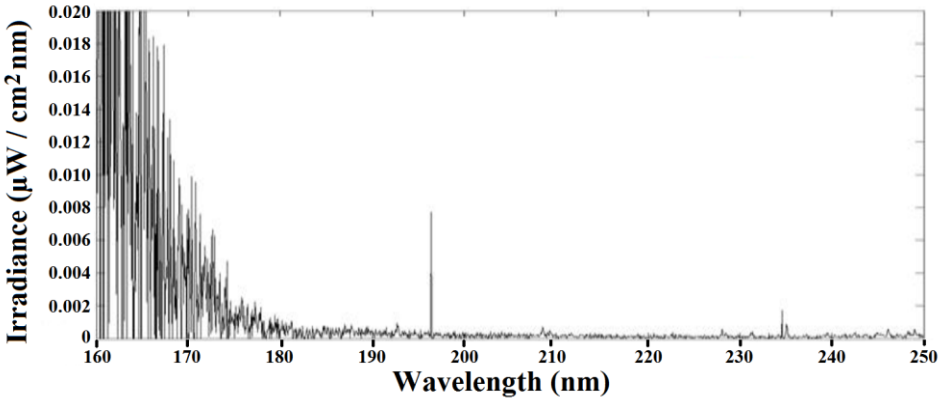

Figure 6.12: Spectrum of krypton for 160 - 250 nm captured with Maya 2000

The McPherson acquired spectra using a gas jet with a pressure of 2311 Torr. Figure 6.13 shows the acquired spectra from the McPherson with an integration time of 600 seconds, calibrated with the transfer function from Figure 6.8. In this spectral range, there are three strong peaks one at 118.8 nm with an irradiance of 0.084, a Lyman-alpha peak at 121.5 nm with an irradiance of 0.63 $\mu W/cm^2 \cdot nm$, and a peak at 161 nm with an irradiance of 0.158 $\mu W/cm^2 \cdot nm$. However, there are significant spectral artifacts from the irradiance transfer function in this spectrum. These have an effect of hiding lines and changing relative line irradiance.

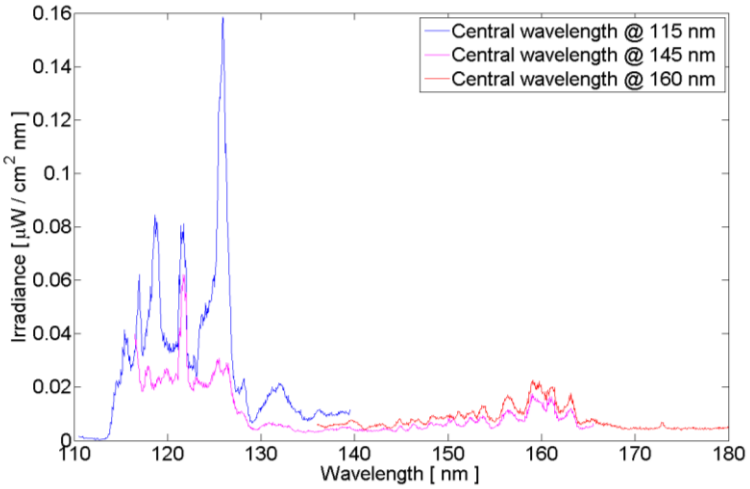

Figure 6.13: Spectrum of krypton for 115 - 170 nm aquired with McPherson

6.3.3.3 Xenon

Like the other noble gas targets the 6 second integration time of the Maya 2000 and xenon's low emission at longer wavelengths prevented the use of a gas jet target for the Maya. The chamber was filled to a pressure of 863 Torr, to provide a larger target volume. This bulk gas condition provides a larger target area, providing a stronger signal with the larger etendue. Figure 6.14 shows the acquired spectrum from the Maya 2000 with an integration time of 6 seconds, calibrated with the transfer function from Figure 6.8. In this spectral range, there are many spectral lines. There are three spectral line of note 229.4 nm with an irradiance of 0.006 $/cm^2 \cdot nm$, 223.2 nm with an irradiance of 0.0049 $\mu W/cm^2 \cdot nm$, and 247.2 with an irradiance of 0.0068 $\mu W/cm^2 \cdot nm$. There is also a group of strong emission lines from 182 – 190 nm with irradiances 0.004 $\mu W/cm^2 \cdot nm$. The sensitivity of the Maya 2000 renders the spectrum unresolvable at wavelengths below 170 nm.

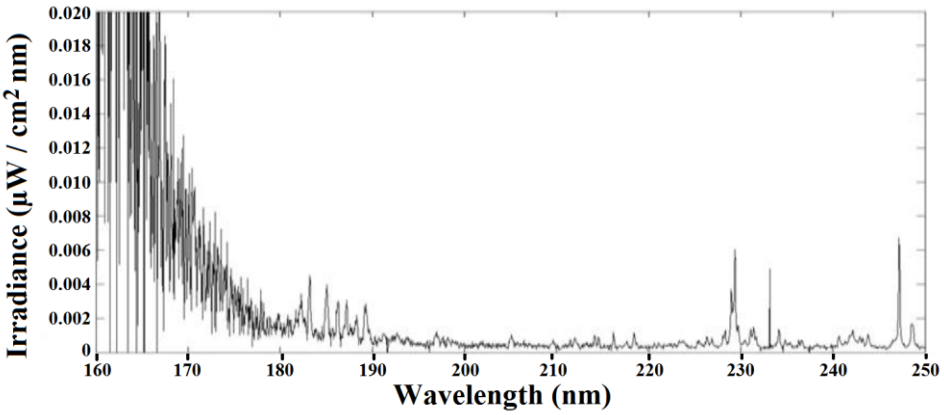

Figure 6.14: Spectrum of xenon for 160 - 250 nm quired with Maya 2000

The McPherson acquired xenon spectra using a gas jet with a pressure of 2311 Torr. Figure 6.15 shows the acquired spectra from the McPherson with an integration time of 600 seconds, calibrated with the transfer function from Figure 6.8. Like the Maya spectrum there are many emission peaks across the entire spectrum. The longest being the Lyman-alpha peak at 121.5 nm with an irradiance of 0.16 $\mu W/cm^2 \cdot nm$. Significant spectral artifacts from the irradiance transfer function contribute to this spectrum. Due to this, it is difficult to resolve particular lines with accuracy.

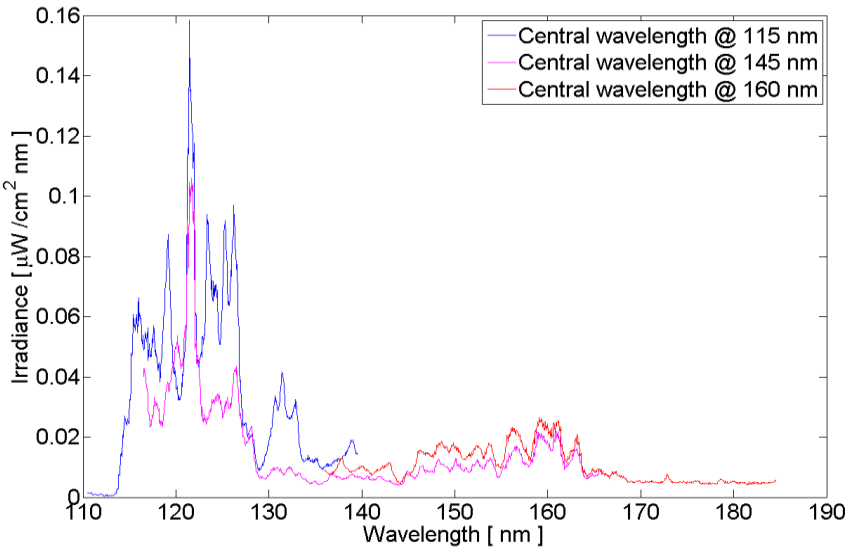

Figure 6.15: Spectra of xenon for 115 - 170 nm aquired with McPherson

6.4 Planar Solid Laser Produced Plasma

An investigation of planar target laser plasma sources, was performed using several pure (99.9%) elements. The purpose of these studies was to investigate emission properties of several materials, with different irradiance conditions. The targets chosen were magnesium, aluminum, silicon, copper, zinc, molybdenum, indium, tin, and tantalum. These gases were chosen because of their many possible electron transitions and inert chemical properties. For these studies the Spectra Physics Quantaray GCR-190-100 laser and the IPG YLP-HP-25-100-20-500 EQ laser as discussed in Section 6.1.2 was used to irradiate these planar targets. The target chamber was maintained at 10^{-4} Torr.

6.4.1 Positioning Apparatus

In order to prove a fresh target for each laser pulse the rotary target scheme discussed in Section 3.1.1 was used. To move the target a linear and rotary stage was used, as seen in Figure

6.16. For linear motion a linear DC servo motor was used. This actuator translated a stage in the plane of the target by 25 mm with a ±1.5 μm bi-directional repeatability and a maximum travel rate of 0.4 mm/s. Attached to this stage was a rotational stage actuated with a DC servo motor, with its axis normal to target surface. The motorized stage provides up to 20°/s maximum angular speed, with a 0.15° bi-directional repeatability. Mounted on this stage, was a planar target holder, which will be discussed further in Section 6.4.2. In order to align the stage a mirror was installed into the target holder. The 532 nm alignment beams as discussed in 6.1.3 were reflected off of the mirror while the stages were adjusted so that the beams were reflected onto one another through the alignment iris mounted in the chamber. Once propagation of the alignment beams satisfied the conditions described in Section 6.1.3 the stage was aligned. In addition, during this process the linear and rotary stages were activated to verify the alignment of the travel to the plane of the target, and to the focus of the irradiation laser.

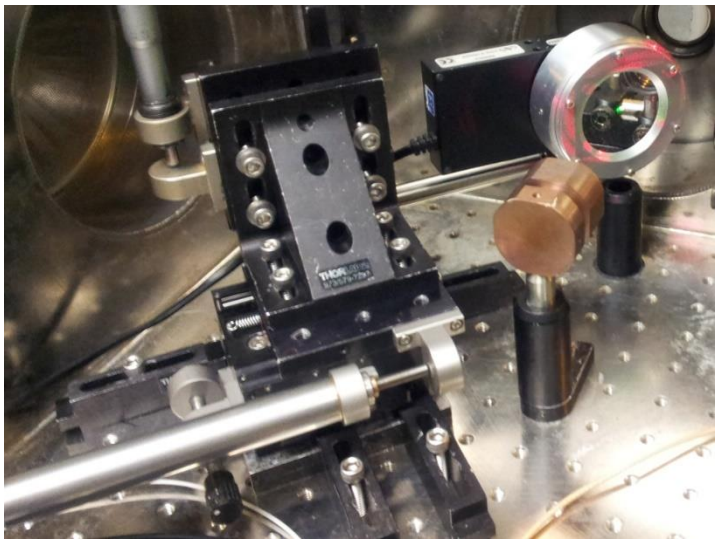

Figure 6.16: Solid target positioning apparatus showing linear stage, rotational stage, and target holder with alignment mirror.

6.4.2 Target Mounting

Mounting of a solid target onto a rotary stage requires that the surface of the target to be aligned with the metrology and optics of the system. Planar targets are expendable; therefore, it needs to be exchanged while maintaining the alignment. To facilitate these requirements a target holder was developed to provide repeatable alignment of the target surface within 50 micron of the focal plane. The principle features of this mounting system are the mount and the case. The mount is fixed to the rotary stage and has a mechanism that holds and aligns the case to the stage and optics. The case serves 3 functions: to clamp the solid target to an alignment surface on the case, to provide a surface to align the case to the mount, and to center the target in the mount. These functions must also accommodate different thickness targets, as thickness can vary depending on material. Also included in the apparatus, is a backing plate. The plate pushes evenly on the target to clamp it to the surface of the case. Several techniques were used for these studies. The first technique, as seen in Figure 6.17(a) the case has a female thread matching the male thread of the backing plate. When the backing plate is tightened, it clamps the target against the lip of the case. The case is then inserted into the holder. In Figure 6.17(b) the backing plate slides into the case, and instead asset screw in the case pushes the backing plate clamping the target. With the third method, spring pins built into the holder push the backing plate into the target, clamping it to the case. Each method has pros and cons. Method (a) while having the best clamping, suffers from high friction in the threads causing the backing plate to lock into the case. Method (b) provides an alternative with less friction on the set screw than the backing plate in Method (a). However, it requires a case which is deeper, which can be a problem in smaller spaces. In method (c) the threads are removed, and spring pins provide the clamping force.

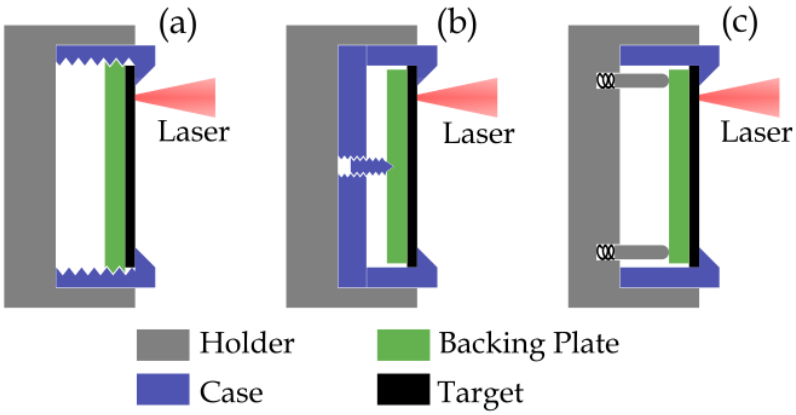

Figure 6.17: Solid Target holder configuations:(a) threaded backing, (b) set screw, (c) spring pin

6.4.3 Emission Spectra

Emission spectra for silicon, copper, molybdenum, indium, tantalum, tin, and zinc were obtained from plasmas formed by the Spectra Physics Quantaray GCR-190-100 and the IPG YLP-HP-25-100-20-500 EQ lasers (Section 6.1.2). The intensity of the lasers at the plasma position was varied between $8x10^6$ and $3.2x10^{12}$ W/cm^2. For spectra in the 123.4 – 140 nm range the Seya-Namioka style McPherson spectrometer (McPherson) was used. A smoothed irradiance transfer function Figure 4.3 was used for calibrating the spectra obtained spectra. For the wavelength region of 165 – 250 nm the Maya 2000 Pro spectrometer (Maya) was used calibrated with the smoothed irradiance transfer function in Figure 4.12. For wavelengths below 175 nm the sensitivity of the Maya spectrometer is limited so artifacts of the low signal to noise of the transfer function is evident in the acquired spectra.

6.4.3.1 Silicon

Spectra for planar silicon were generated using the Spectra Physics Quantaray GCR-190-100 laser (Section 6.1.2), with a target beam diameter of 60 µm at the target, and a 10 ns pulse width. Several laser intensities were used: $1.5x10^{11}$, $7.0x10^{11}$, $1.4x10^{12}$, $2.0x10^{12}$, $2.8x10^{12}$, and $3.2x10^{12}$ W/cm^2. The spectra shown in Figure 6.18, was acquired with the McPherson spectrometer for a spectral range of 123.4 – 165 nm. Silicon has a near flat continuum with a small increase at longer wavelengths at intensities higher than $1.4x10^{10}$ W/cm^2. In addition to the continuum silicon has several strong line emissions at 129.9, 139.4, 141, 151, and 153.8 nm.

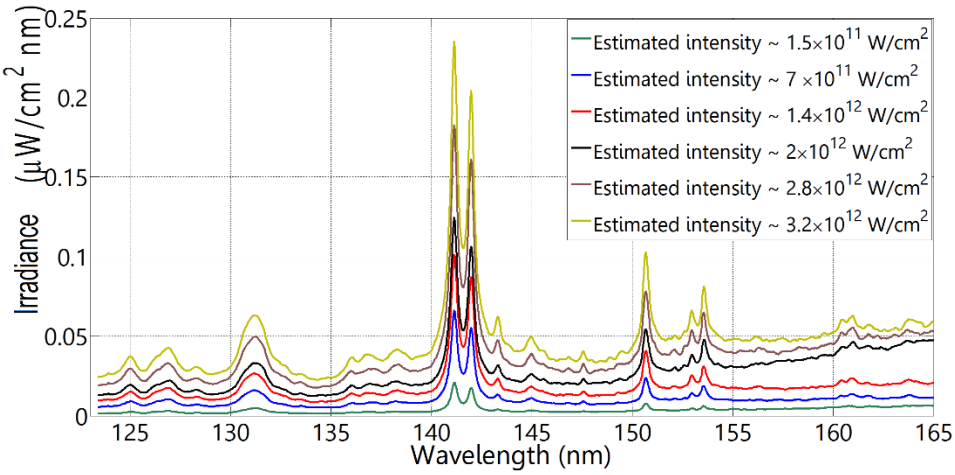

Figure 6.18: Spectra of silicon for 123.4 – 165 nm for different laser intensities, aquired with McPherson

For each laser intensity, the irradiance spectra were integrated and multiplied by the ratio of 2π sr to the collection solid angle of the spectrometer for 3 separate bands: 123.4 – 140 nm, 140 – 160 nm, and 160 – 165 nm. The resulting in-band power in 2π sr vs laser intensity is shown in Figure 6.19. Here, the in-band region of 140 – 160 nm has the highest power of 0.065 Watt in 2π sr.

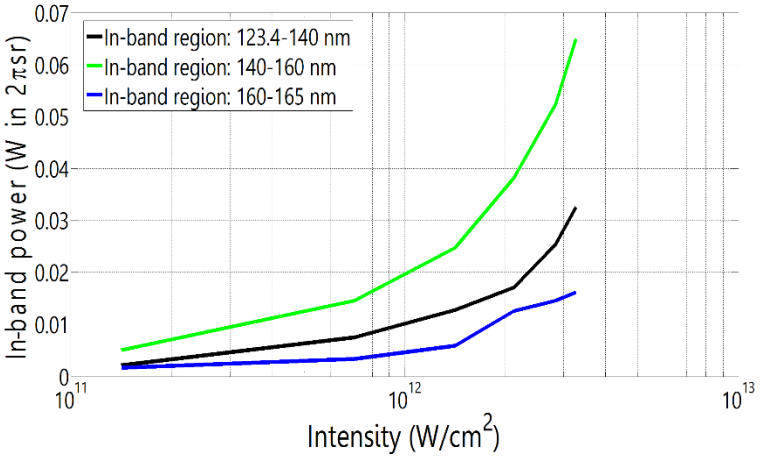

Figure 6.19: Inband power of silcon for wavlength regions of 123.4 – 140 nm, 140 – 160 nm, and 160 – 165 nm vs laser intensity

The conversion efficiency (CE) for each laser intensity was determined by dividing the resulting in-band power by the laser input power and multiplying by 100. As seen in Figure 6.20, the highest CE occurs at low intensities. This is due to stronger emission at shorter out of band wavelengths due to the higher energy of the plasma. The lowest CE occurs at $1.4x10^{12}$ W/cm^2 for in band regions 140 – 160 nm, and 160 – 165 nm, and at $2.0x10^{12}$ for 123.5 – 140 nm.

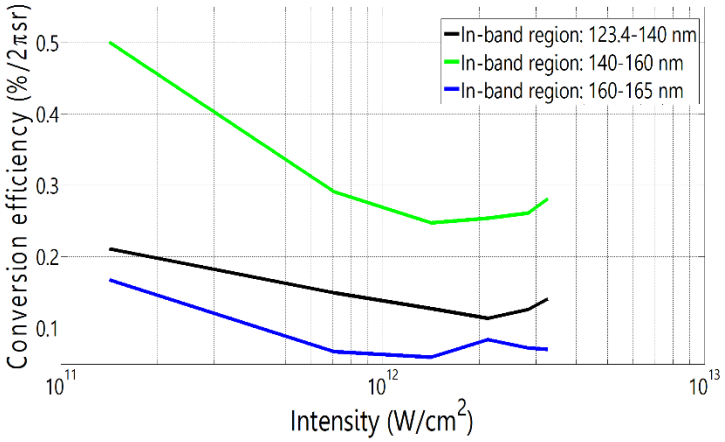

Figure 6.20: Conversion efficency (CE) of silicon for inband regions 123.4 – 140 nm, 140 – 160 nm, and 160 – 165 nm vs laser intensity

6.4.3.2 Copper

The Spectra Physics Quantaray GCR-190-100 laser (Section 6.1.2), with a target beam diameter of 60 µm at the target, and a 10 ns pulse width, was used to generate VUV spectra for planar copper targets. The laser intensities used were: $3.0x10^9$, $6.0x10^9$, $9.0x10^9$, $2.0x10^{10}$, $4.0x10^{10}$, and $8.9x10^{10}$ W/cm^2. Spectra (Figure 6.21) was acquired with the McPherson spectrometer with an integration time of 15 minutes. Significant spectral continuum is seen across the range of 123.4 – 168 nm. The spectra have a minimum across the range of ~147 – 156 nm, as the continuum increases up to 3 times the minimum values. At $8.9x10^{10}$ W/cm^2 there is a significant line emission at 136.7 nm this line emission is over 0.025 W/cm^2.

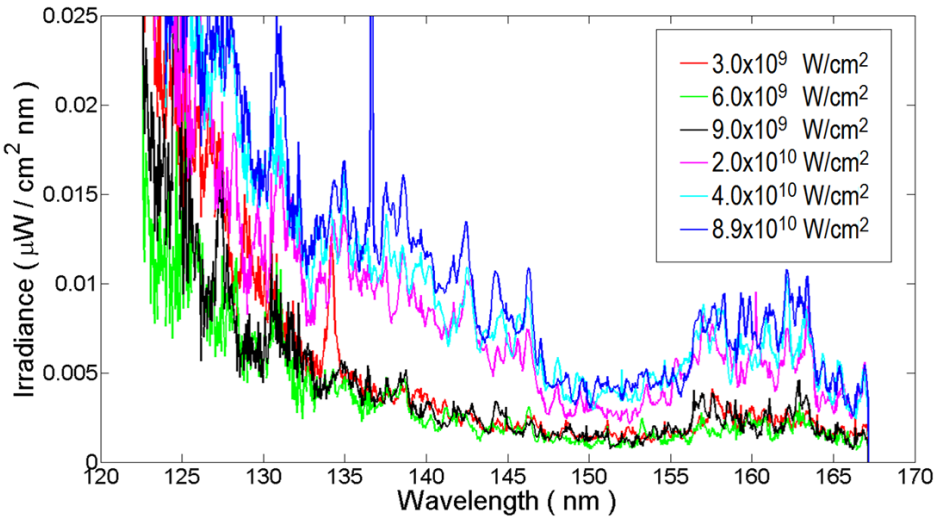

Figure 6.21: Spectra of copper for 123.4 – 168 nm for different laser intensities, aquired with McPherson

6.4.3.3 Molybdenum

Molybdenum spectra for planar targets, was produced using the Spectra Physics Quantaray GCR-190-100 laser (Section 6.1.2). Laser intensities of $3.0x10^{10}$, $1.5x10^{11}$, $7.0x10^{11}$, $1.4x10^{12}$, $2.0x10^{12}$, $2.8x10^{12}$ W/cm^2, and $3.2x10^{12}$ W/cm^2 where used. The McPherson spectrometer acquired spectra for a spectral range of 123.4 – 165 nm, and is shown in Figure 6.22. The spectra have broad continuum across the range with irradiance at wavelengths longer than 142 nm increasing up to 2.3 times the shorter wavelength continuum. There are two prominent line emissions at 148.8 and 159.6 nm.

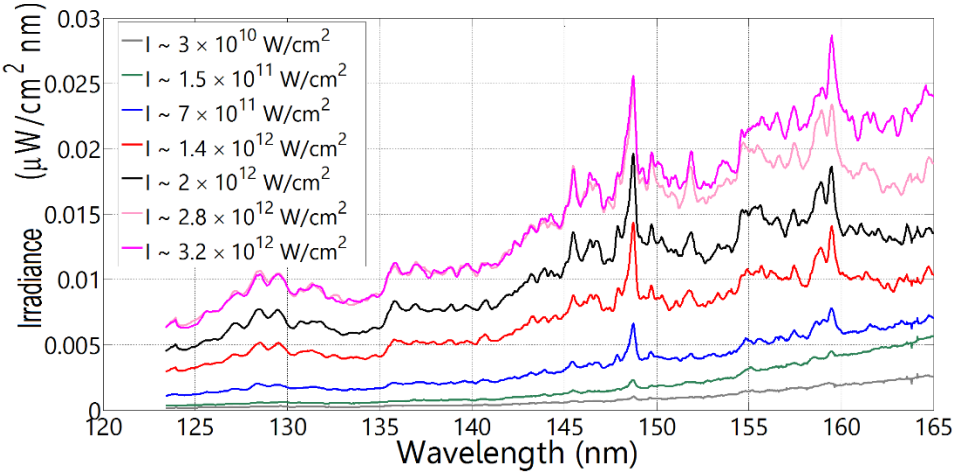

Figure 6.22: Spectra of molybdenum for 123.4 – 165 nm for different laser intensities, aquired with McPherson

At each laser intensity in 3 separate bands, 123.4 – 140 nm, 140 – 160 nm, and 160 – 165 nm. As described in Section 6.4.3.1, in-band power vs laser intensity was calculated and is shown in Figure 6.23. Here, the in-band region of 140 – 160 nm has the highest power of 0.021 Watt in 2π sr.

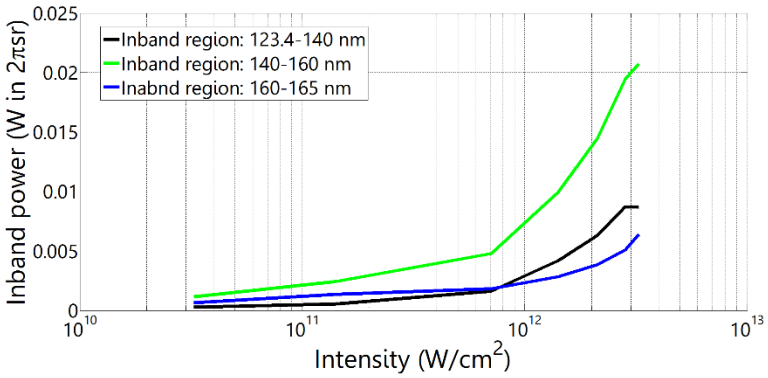

Figure 6.23: The in-band power of molybdenum for wavelength regions of 123.4-140 nm, 140-160 nm, and 160-165 nm vs the laser intensity

The conversion efficiency (CE) (Figure 6.24) was determined by dividing the resulting in-band power by the laser input power and multiplying by 100. The highest CE occurs at low intensities. The lowest CE occurs at 7.0×10^{11} W/cm^2 for in band regions 123.5 – 140 nm, 3.2×10^{12} W/cm^2 for 140 – 160 nm, and at 2.8×10^{11} W/cm^2 for 160 – 165 nm.

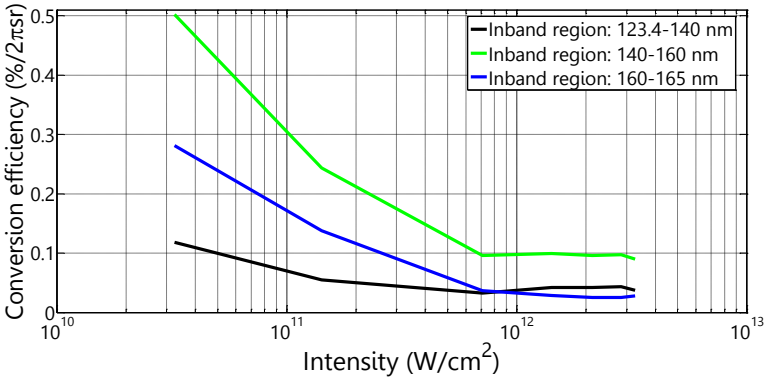

Figure 6.24: Conversion efficienct (CE) of molybdenum for wavelength regions of 123.4-140 nm, 140-160 nm, and 160-165 nm vs the laser intensity

6.4.3.4 Indium

Planar molybdenum spectra were generated using the Spectra Physics Quantaray GCR-190-100 laser (Section 6.1.2). The laser intensities used were: 3.0×10^9, 6.0×10^9, 9.0×10^9,

$2.0x10^{10}$, and $4.0x10^{10}$. Spectra for a spectral range of 123.4 – 168 nm, shown in Figure 6.25, was acquired with the McPherson spectrometer.

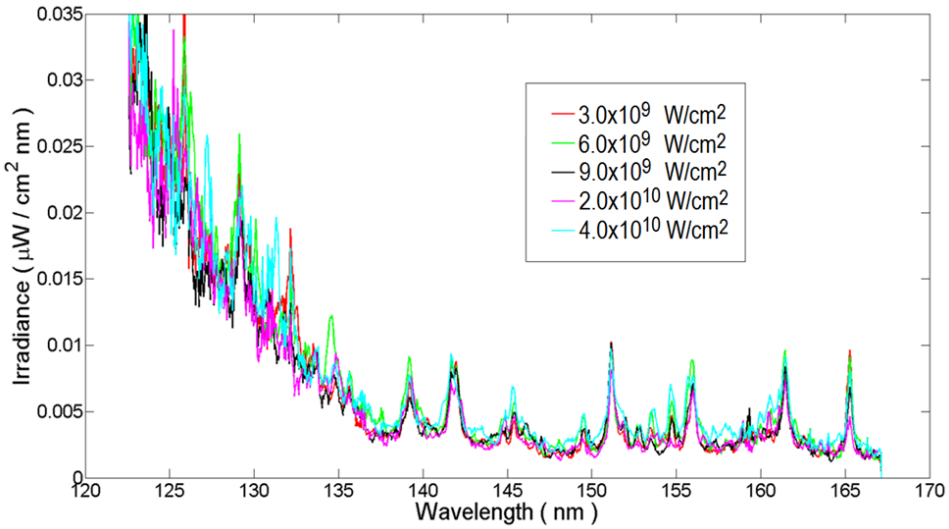

Figure 6.25: Spectra of indium for 123.4 – 168 nm for different laser intensities, acquired with McPherson

Here the spectra have relatively flat continuum across wavelengths longer than 138 nm, with little change in emission with laser intensity. In this wavelength range, there are several strong line emissions that are several times stronger than the background continuum at 139.3, 141.7, 145.4, 149.5, 151.2, 153.5, 154.7, 155.9, 161.4 and165.3nm. At shorter wavelengths, the continuum increases several times as wavelength decrease. At these wavelengths, there are many strong line emissions, with several prominent wavelengths at 134.9, 132.2, 129.2, and 125.9 nm.

6.4.3.5 Tantalum

For planar tantalum, the Spectra Physics Quantaray GCR-190-100 laser (Section 6.1.2) was used to provided laser intensities of $1.5x10^{11}$, $7.0x10^{11}$, $1.4x10^{12}$, $2.0x10^{12}$, $2.8x10^{12}$ W/cm^2,

and $3.2x10^{12}$ W/cm^2. The generated spectra are shown in Figure 6.26, was acquired with the McPherson spectrometer for a spectral range of 123.4 – 165 nm. The spectra of tantalum have a broad continuum over this range and numerous line emissions. Some of the strongest line emissions are at 141.1, 147.9, 154.6, 156.6, 159.4, 160.8, 163.5, and 164.9 nm. The irradiance from this plasma is stronger for wavelengths longer than 135 nm, with peak emission around 160 nm.

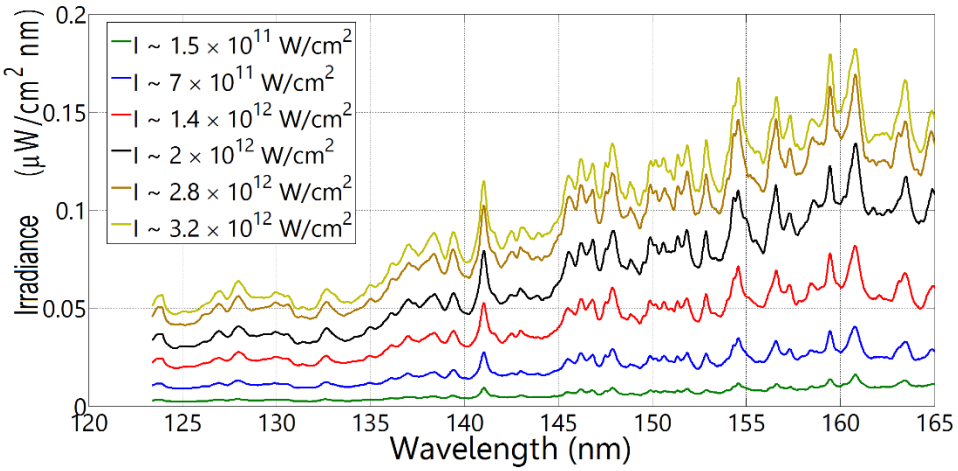

Figure 6.26: Spectra of tantalum for 123.4 – 165 nm for differnt laser intensities, aquired with McPherson

Irradiance spectra was calculated for each laser intensity for the wavelength bands: 123.4 – 140 nm, 140 – 160 nm, and 160 – 165 nm. Irradiance spectra were integrated and multiplied by the ratio of 2π sr to the collection solid angle of the spectrometer, resulting in-band power vs laser intensity, as shown in Figure 6.27. Here, the in-band region of 140 – 160 nm has the highest power of 0.13 Watt in 2π sr.

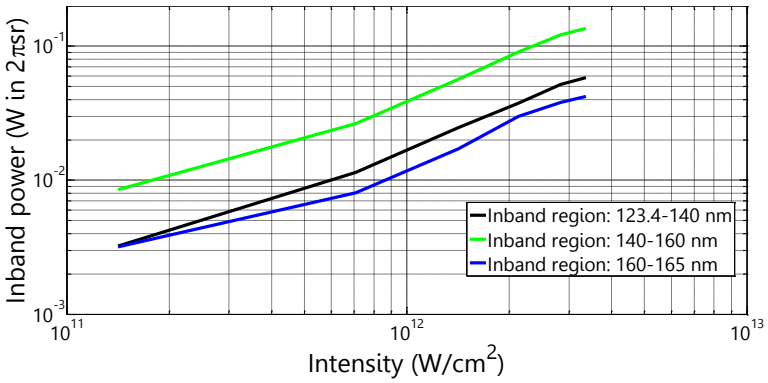

Figure 6.27: In-band power of tantalum for wavelength regions of 123.4-140 nm, 140-160 nm, and 160-165 nm vs the laser intensity

By dividing the resulting in-band power by the laser input power and multiplying by 100, the conversion efficiency (CE) was determined (Figure 6.28). the highest CE is at low laser intensities. The lowest CE occurs at 7.0×10^{12} for in band regions 123.5 – 140 nm, 140 – 160 nm, and 160 – 165 nm.

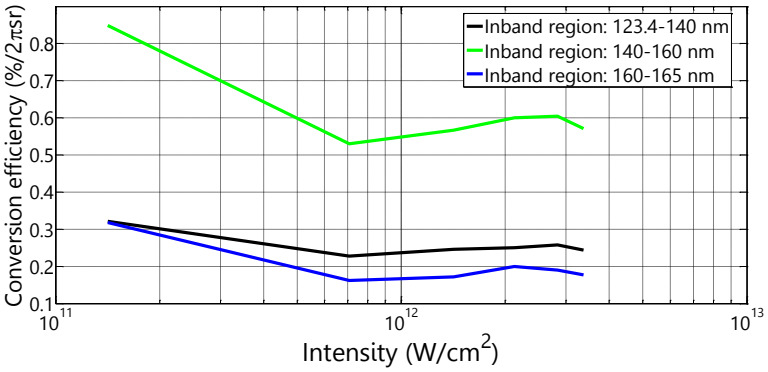

Figure 6.28: Conversion efficiency (CE) of tantalum for wavelength regions of 123.4-140 nm, 140-160 nm, and 160-165 nm vs the laser intensity

6.4.3.6 Tin

Spectra for planar tin targets were produced using the Spectra Physics Quantaray GCR-190-100 laser (Section 6.1.2). The laser spot size was 200 µm. Several laser intensities were

used: $7.0x10^9$, $1.4x10^{10}$, $5.5x10^{10}$, $1.0x10^{11}$ W/cm^2, $4.0x10^{11}$ W/cm^2, and $1.0x10^{12}$ W/cm^2. For a spectral range of 123.4 – 165 nm, the spectra shown in Figure 6.29, was acquired with the McPherson spectrometer for a. For these lower laser intensities, tin has stronger emission at wavelengths less than 140 nm. At $1.0x10^{12}$ W/cm^2 it has stronger line emission at shorter wavelengths. Strong line emission from tin is present across a broad continuum, with peaks at 157.1, 149.7, 148.5, 146.3, 145.3, 142.8, 141.8, 136.8, 133.1, 130.6, and 125.2 nm. The strongest peak is at 145.3 nm.

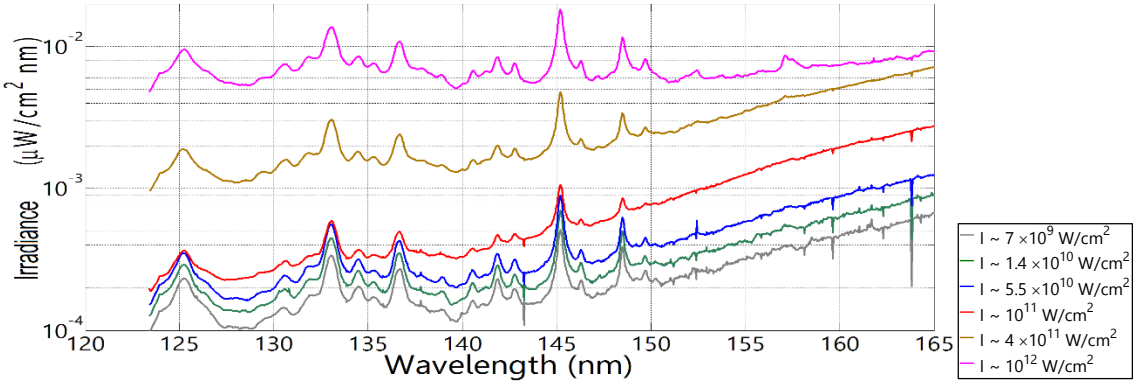

Figure 6.29: Spectra of tin for 123.4 – 165 nm for different laser intensities, aquired with McPherson

As described in Section 6.4.3.5, irradiance spectra were calculated for each laser intensity across three separate bands: 123.4 – 140 nm, 140 – 160 nm, and 160 – 165 nm. The resulting in-band power vs laser intensity is shown in Figure 6.30. Here, the in-band region of 140 – 160 nm has the highest power of 0.008 Watt radiated in 2π sr.

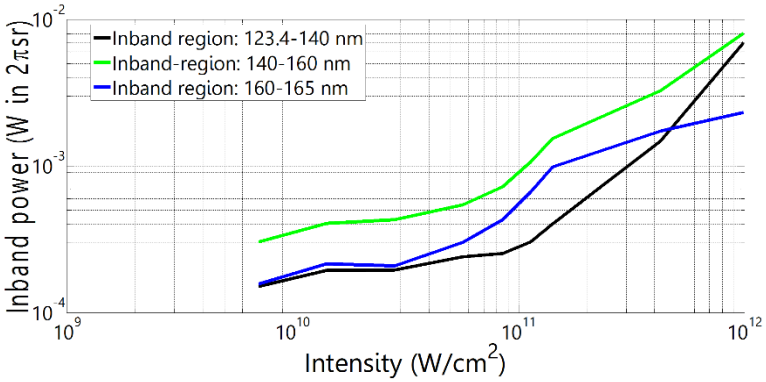

Figure 6.30: In-band power of tin for wavelength regions of 123.4-140 nm, 140-160 nm, and 160-165 nm vs the laser intensity

By dividing in-band power by the laser input power and multiplying by 100, conversion efficiency (CE) was calculated. As seen in Figure 6.31, the highest CE is at low intensities. The lowest CE occurs at $1.0x10^{11}$ W/cm^2 for in band regions 123.5 – 140 nm, $4.0x10^{11}$ W/cm^2 for 140 – 160 nm, and at $1.0x10^{12}$ W/cm^2 for 160 – 165 nm.

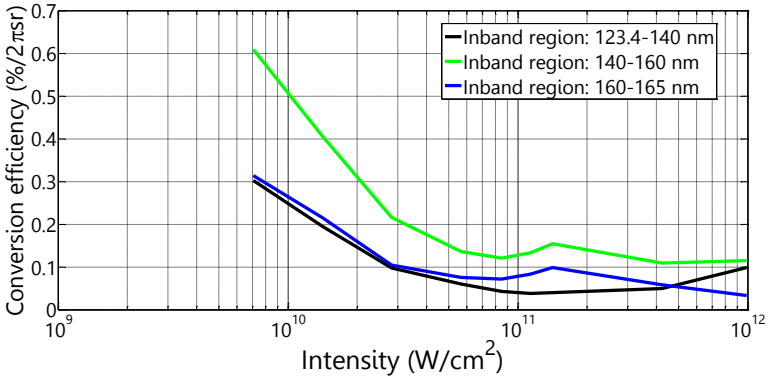

Figure 6.31: Conversion efficiency (CE) of tin for wavelength regions of 123.4-140 nm, 140-160 nm, and 160-165 nm vs the laser intensity

In addition to the above, spectra for a spectral range of 165 – 250 nm (Figure 6.32), was acquired with the Maya 2000 spectrometer. The laser intensities of $8.0x10^9$, $1.0x10^{10}$, and $1.6x10^{10}$ were used. For this spectral range, tin has a higher spectral irradiance, with the background continuum approximately 10 times higher than for the 123.4 – 165 nm range and

similar laser intensities. The spectra have a relatively flat continuum is relatively with higher emission at shorter wavelengths, and numerous strong emission lines with emission as high as 3.5 times background continuum. The peaks of the line emission for this spectral range occur at 248.4, 243.4, 242.7, 241.9, 235.4, 233.3, 231.6, 226.7, 224.5, 222.8, 222.0, 215.1, 208.2, 206.9, 194.1, 189.8, 182.9, 177.8, and 175.6 nm. Also present in this spectra, is a wide fluctuation of spectral intensity across the 176 – 165 nm range. This is due to a low signal to noise ratio of the acquired spectra. Artifacts from the high noise in calibration transfer function artificially increase the irradiance in this range.

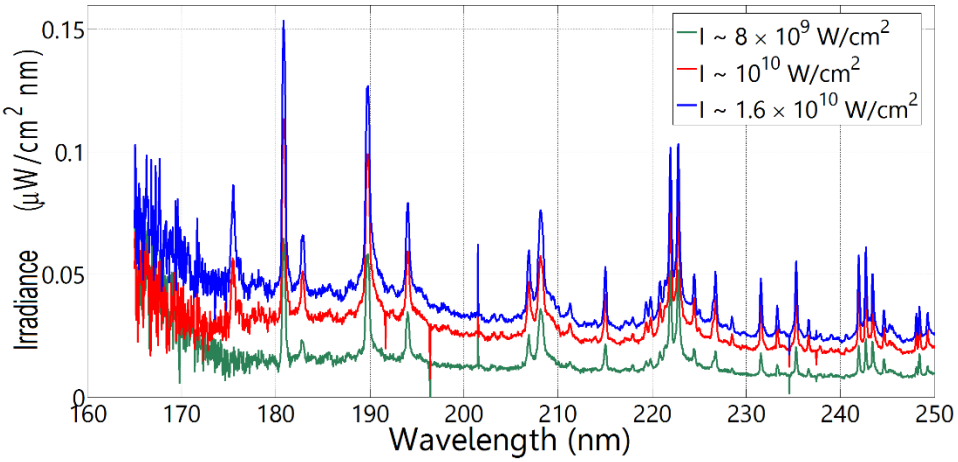

Figure 6.32: Spectra of tin for 165 – 250 nm for different laser intensities, aquired with Maya 2000

The in-band power vs laser intensity, shown in Figure 6.33, was calculated from the irradiance spectra for 5 separate bands: 165 – 180 nm, 180 – 200 nm, 200 – 220 nm, 220 – 240 nm and 240 – 250 nm. The in-band region of 180 – 200 nm has the highest power of 0.039 Watt in 2π sr.

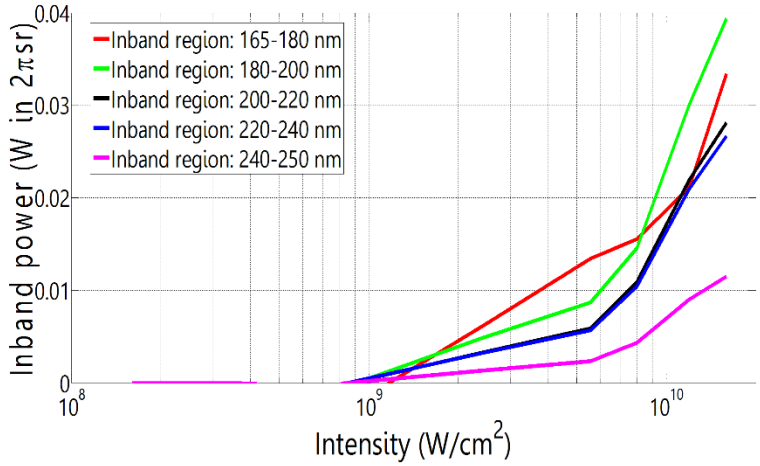

Figure 6.33: In-band power of tin for wavelength regions of 165-180 nm, 180-200 nm, 200-220 nm, 220-240 nm, and 240-250 nm vs the laser intensity

The conversion efficiency (CE) was calculated and is shown in in Figure 6.34 the highest CE is at low intensities. The lowest CE occurs below 7.0×10^8 W/cm^2 for in-band regions 180 – 200 nm, 200 – 220 nm, 220 – 240 nm, 240 – 250 nm, and 5.0×10^9 W/cm^2 for 165 – 180 nm.

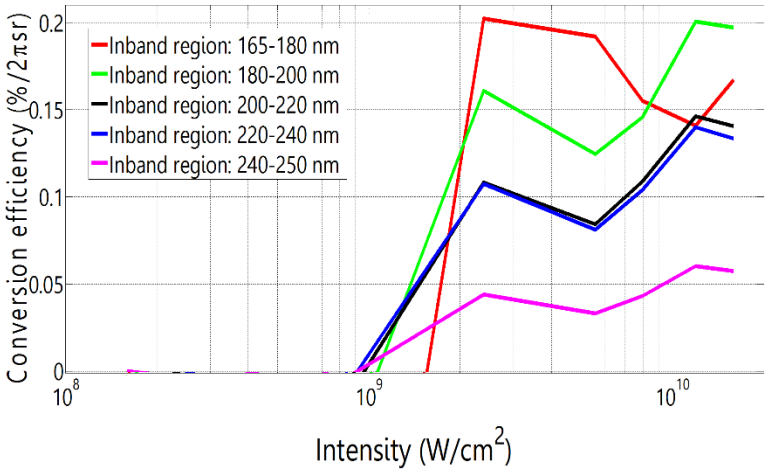

Figure 6.34: Conversion efficiency (CE) of zinc for wavelength regions of 165-180 nm, 180-200 nm, 200-220 nm, 220-240 nm, and 240-250 nm vs the laser intensity

Imaging of the tin plasma was performed using the Schwarzschild plasma imager discussed in Section 4.3. Plasma images shown in Figure 6.35 were obtained with the Spectra

Physics Quantaray GCR-190-100 laser (Section 6.1.2). The laser spot size was 200 µm with a laser intensity of $6.3x10^8$ W/cm^2. The plasma images were captured at 10 ns intervals with an integration time of 10 ns. The imager used a 172 nm filter, with a spectral bandwidth of 24 nm FWHM. The plasma emission at this wavelength is approximately 65 ns in duration. The images show that the plasma size is ~400 µm at peak emission at 25 ns after irradiation by the laser.

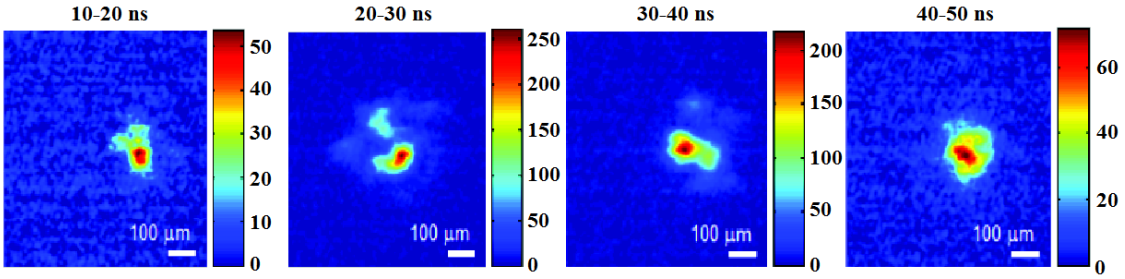

Figure 6.35: Time-resolved image of tin plasma at 172 nm for 10 ns intervals with a laser intesity of $6.3x10^8$ W/cm2. False color scale in abitrary intensity units.

6.4.3.7 Zinc

Spectra for planar zinc targets were generated using the Spectra Physics Quantaray GCR-190-100 laser (Section 6.1.2). The laser spot size was 200 µm. Several laser intensities were used: $8.0x10^9$, $1.0x10^{10}$, and $1.6x10^{10}$. Higher intensities where limited due to the low melting point of zinc as compared to other planar targets. At these higher intensities the average power was enough to melt the neighboring target material, causing erratic plasma conditions. Figure 6.36 shows spectra was acquired with the McPherson spectrometer for a spectral range of 123.4 – 165 nm. The spectra have two characteristic regions: wavelengths shorter and longer than 140 nm. The shorter wavelength region has a broad continuum increasing toward longer wavelengths, with several line emissions. This emission has peaks at 139.3, 138.0, 136.9, 136.0,

134.5, 133.6, 131.8, 130.4, 128.9, 127.9, 127.0, 125.1, and 123.8. The longer wavelength region also has continuum that increases at longer wavelengths. However, this spectral band has a higher density of line emission, with peaks at 164.3, 163.1, 162.2, 159.9, 158.0, 156.0, 155.2, 151.9, 151.0, 150.5, 148.5, 148.2, 146.7, 146.2, 145.7, 144.5, 144.0, 143.6, 141.1, and 140.5. The short wavelength line emission FWHM is on average 50% broader than the long wavelength band. In addition, at lower laser intensities, the shorter wavelength band has a higher irradiance that the long wavelength band. At higher laser intensities, the longer wavelengths increase at a greater rate than the shorter wavelengths.

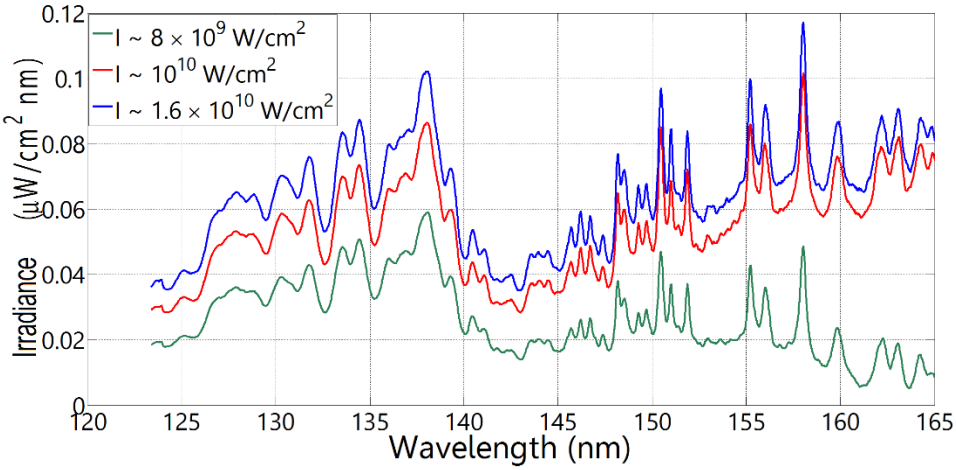

Figure 6.36: Spectra of zinc for 123.4 – 165 nm for different laser intensities, aquired with McPherson

At each laser intensity three bands, 123.4 – 140 nm, 140 – 160 nm, and 160 – 165 nm, the in band power in 2π sr was calculated. As seen in Figure 6.37, the in-band region of 123.4 – 140 nm has the highest power of 0.09 Watt in 2π sr.

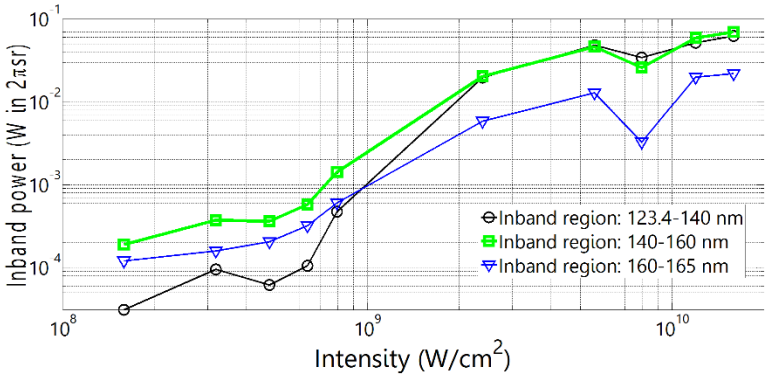

Figure 6.37: In-band power of zinc for wavelength regions of 123.4-140 nm, 140-160 nm, and 160-165 nm vs the laser intensity

Conversion efficiency (CE) for these bands for each laser intensity, as seen in Figure 6.38, were calculated. The highest CE occur at laser intensities between $2.2\text{x}10^9$ – $5.3\text{x}10^9$ W/cm^2, and the lowest CE occurs at $4.6\text{x}10^8$ W/cm^2 for in band regions 123.5 – 140 nm, 140 – 160 nm, and 160 – 165 nm.

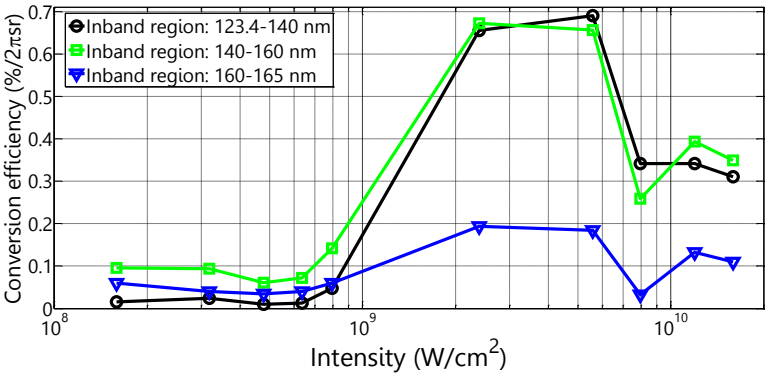

Figure 6.38: Conversion efficienct (CE) of zinc for wavelength regions of 123.4-140 nm, 140-160 nm, and 160-165 nm vs the laser intensity

The spectra shown in Figure 6.39, was acquired with the Maya 2000 spectrometer for a spectral range of 165 – 250 nm. The laser intensities used were $8.0\text{x}10^9$, $1.0\text{x}10^{10}$, and $1.6\text{x}10^{10}$. For this spectral range, tin has a higher peak spectral irradiance with similar background continuum than the 123.4 – 165 nm range. The broad continuum emission for zinc is relatively flat with very

little line emission. The notable exception to this is the four strong line emission peaks at 216.5, 221.7, 227.1, and 232.6. These peaks have and irradiance as high as 8.5 times the background continuum, and line widths of 0.6 – 1.0 nm FWHM. There is also one smaller line emission peak at 176.7 nm, and several line emissions at longer wavelengths with peaks at 272.3, 273.6, 275.7, 279.1, 280.1, 282.0, and 282.7. Wide fluctuation of spectral intensity across the 176 – 165 nm range, are also present in these spectra. This is due to the low signal to noise ratio of the acquired spectra in this region. Artifacts from the high noise in calibration transfer function artificially increase the irradiance in this range.

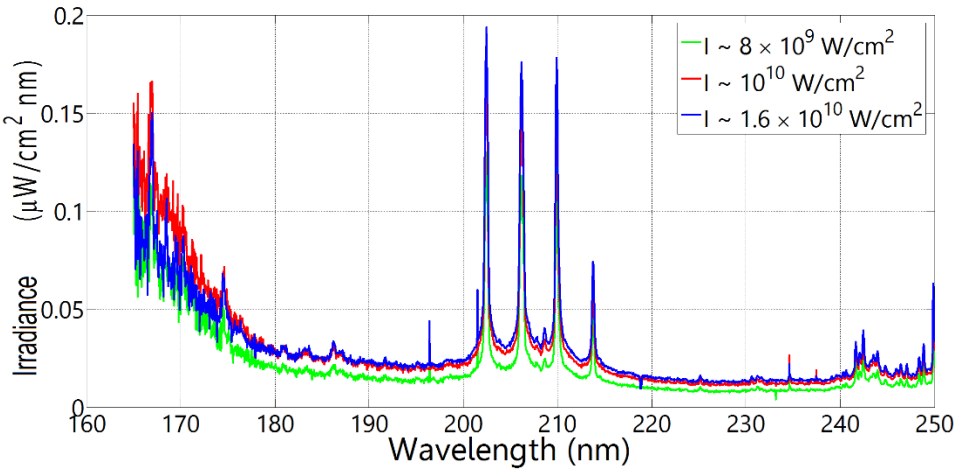

Figure 6.39: Spectra of zinc for 165 – 250 nm for different laser intensities, aquired with Maya 2000

Five separate bands: 165 – 180 nm, 180 – 200 nm, 200 – 220 nm, 220 – 240 nm and 240 – 250 nm, were used to calculate the in-band power vs laser intensity (Figure 6.40). The in-band region of 165 – 180 nm has the highest power of 0.043 Watt in 2π sr

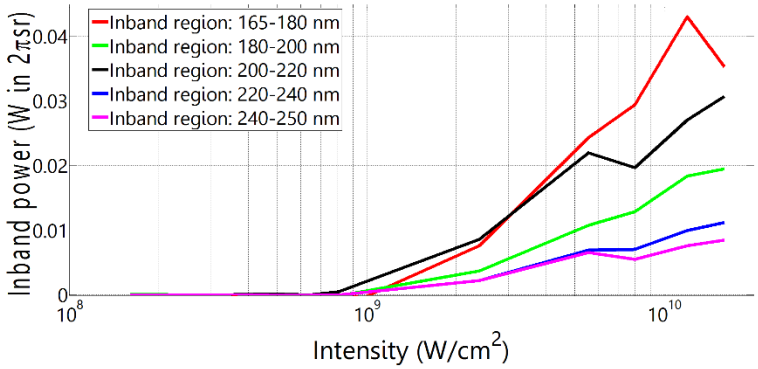

Figure 6.40: In-band power of zinc for wavelength regions of 165-180 nm, 180-200 nm, 200-220 nm, 220-240 nm, and 240-250 nm vs the laser intensity

Conversion efficiency (CE) of several laser intensities where calculated from irradiance spectra. As seen in Figure 6.41, the highest CE is at 5.4×10^9 W/cm^2. The lowest CE occurs at 5.0×10^8 W/cm^2 for in-band regions 180 – 200 nm, less than 2.0×10^8 W/cm^2 for 200 – 220 nm, less than 6.4×10^8 W/cm^2 for 220 – 240 nm, 240 – 250 nm, and less than 1.3×10^9 W/cm^2 for 165 – 180 nm. At laser intensities greater than 6×10^9 W/cm^2 CE begins to reduce due to out of band emission in shorter wavelengths.

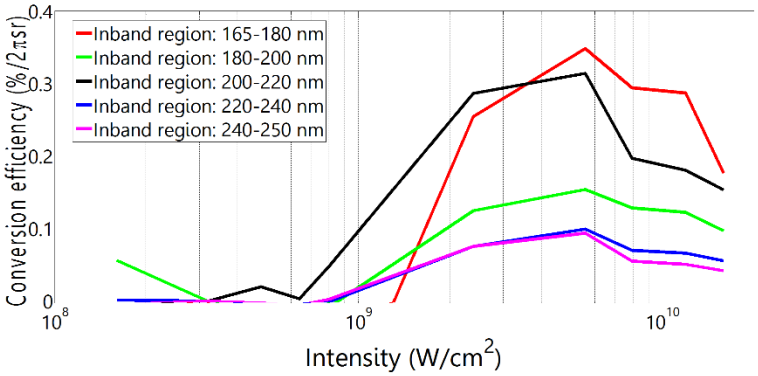

Figure 6.41: Conversion efficiency (CE) of zinc for wavelength regions of 165-180 nm, 180-200 nm, 200-220 nm, 220-240 nm, and 240-250 nm vs the laser intensity

For plasmas formed with laser intensities of 10^9 W/cm^2 or less, the sensitivity of the Maya 2000 spectrometer is low due to the low emitted power. In order to perform spectral

measurements, a higher repetition rate laser is required to increase the average emitted power and increase the number of integrated laser shots on the target. These low intensity plasmas were generated using the IPG YLP-HP-25-100-20-500-EQ fiber laser (Section 6.1.2). The laser spot size was 200 µm FWHM, the repetition rate was 2 kHz, and the pulse width was 60 ns FWHM. Spectra shown in Figure 6.42, was acquired with the Maya 2000 spectrometer for a spectral range of 165 – 250 nm. The laser intensities used were $2.5x10^8$, and $8.0x10^8$ W/cm^2.

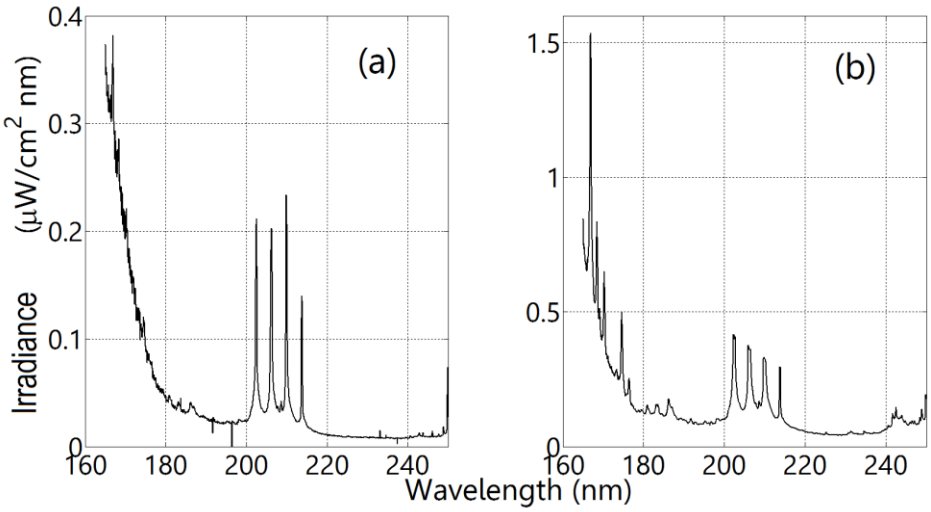

Figure 6.42: Spectra of zinc plasma with 2kHz 60ns laser with (a) $2.5x10^8$ W/cm^2 and (b) $8x10^8$ W/cm^2 laser intensity for 165 – 250 nm

For several low laser intensities, the irradiance spectra were determined for the bands: 165 – 180 nm, 180 – 200 nm, 200 – 220 nm, 220 – 240 nm and 240 – 250 nm. The resulting in-band power vs laser intensity is shown in Figure 6.43. The in-band region of 165 – 180 nm has the highest power of 0.258 Watt radiated in 2π sr.

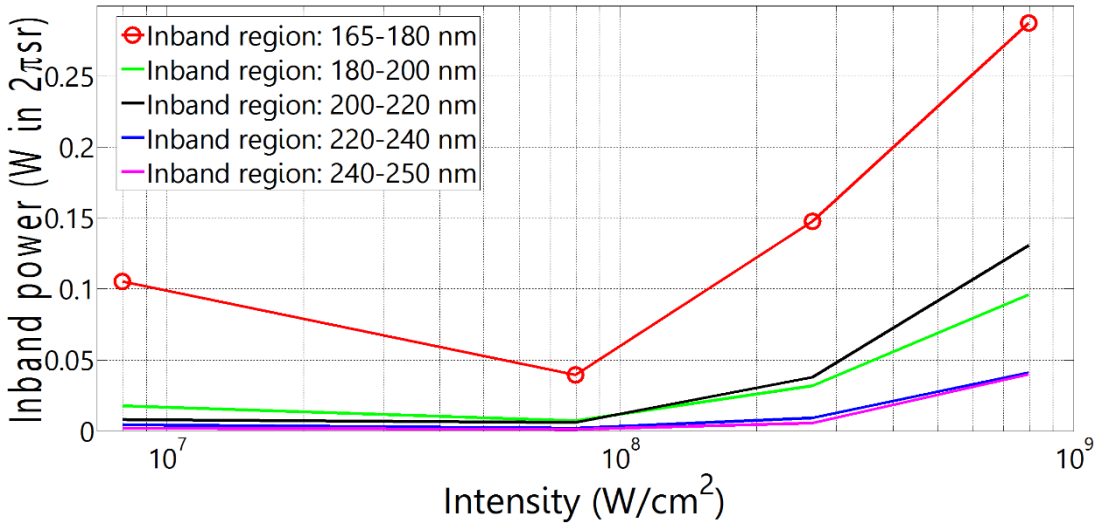

Figure 6.43: In-band power of zinc with 2kHz 60ns laser for wavelength regions of 165-180 nm, 180-200 nm, 200-220 nm, 220-240 nm, and 240-250 nm vs the laser intensity

Conversion efficiency (CE) was calculated for each intensity, as seen in Figure 6.44. The highest CE occurs at 6.0×10^6 W/cm^2, and the lowest occurs at 8.0×10^7 W/cm^2 for in-band regions 180 – 200 nm, 200 – 220 nm, 220 – 240 nm, 240 – 250 nm. At 8.0×10^8 W/cm^2 the lowest CE occurs for 165 – 180 nm.

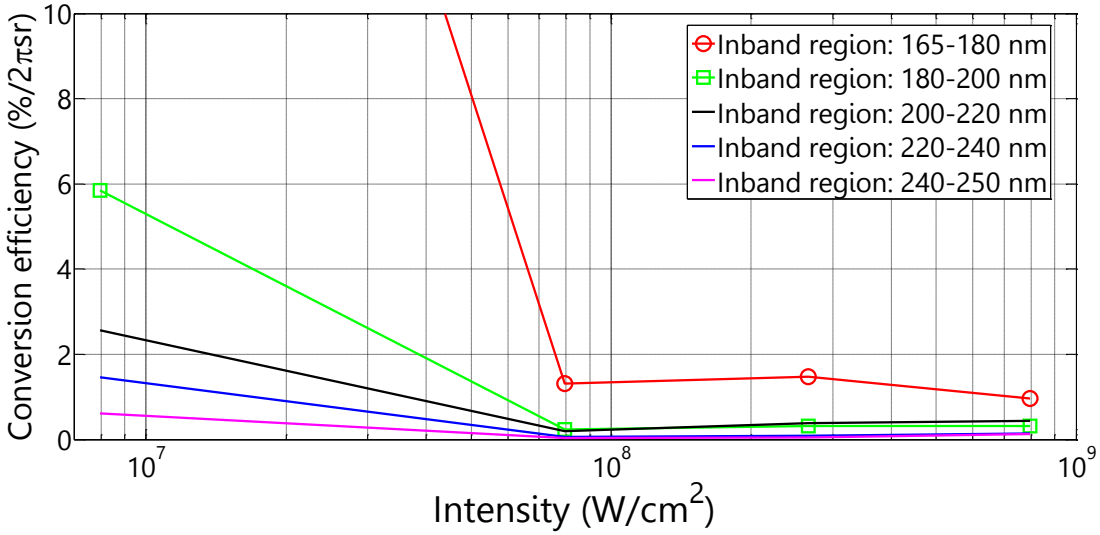

Figure 6.44: Conversion efficiency (CE) of zinc with 2kHz 60ns laser for wavelength regions of 165-180 nm, 180-200 nm, 200-220 nm, 220-240 nm, and 240-250 nm vs the laser intensity (165-180 nm is 35 %/2πsr for 8×10^6)

Using the time resolved Schwarzschild plasma imager discussed in Section 4.3, the zinc plasma was imaged at 172 nm, with a spectral bandwidth of 24 nm FWHM. Figure 6.45 show the plasma images obtained with the Spectra Physics Quantaray GCR-190-100 laser (Section 6.1.2). For these images the laser spot size was 200 µm with a laser intensity of $1.5x10^{10}$ W/cm^2. The plasma images were captured at 10 ns intervals with an integration time of 10 ns. The plasma emission at this wavelength is approximately 50 ns in duration. The plasma size is ~130 µm at peak emission at 25 ns after irradiation by the laser.

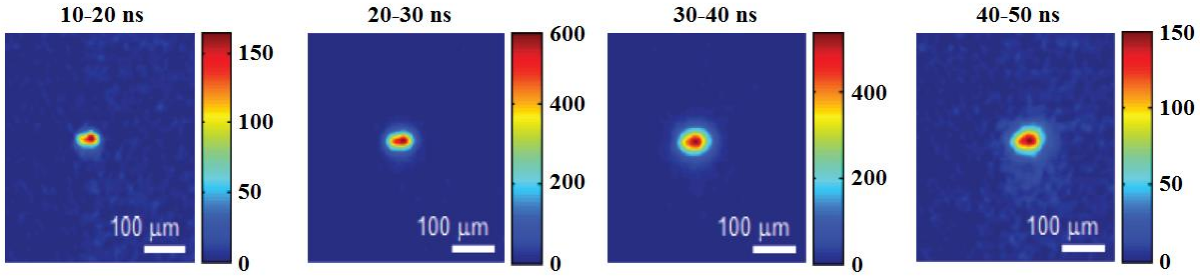

Figure 6.45: Time-resolved image of zinc plasma in abitrary units at 172 nm for 10 ns intervals with a laser intesity of $1.5x10^{10}$ W/cm^2

CHAPTER 7: CONCLUSION

Two comprehensive EUV/VUV laser plasma source systems were developed to measure emission from several laser plasma sources for the XUV band. These sources have important application as light sources across many industries including the semiconductor industry. By taking calibrated measurements of these sources, understanding the physics underlying the processes within laser plasmas can be improved. This allows for the improvement of efficiency and ultimate power output of these sources. For the EUV band (13.5 nm ±2%) a mass limited tin based droplet source was investigated. For the VUV band 250-20 nm band noble gas jets and solid planar targets were investigated.

In this thesis, the fundamental physics behind laser plasmas was discussed. The laser light absorption process was described, and the processes which give rise to line emission and continuum emission. Also discussed was the collisional model and hydrodynamic simulations of these models. Following this, three types of laser plasma types were discussed: planar solid targets, liquid droplet targets and gas jet targets. Their initial ion densities and advantages and disadvantages were described. The mechanical considerations of these targets were discussed in depth including the constraints of each target geometry.

Metrology of the plasma sources were described in detail. The suite of absolutely calibrated spectrometers was described and their calibration techniques. Additionally, several metrology devices, including a time resolved imaging system, and absolute energy meters were also described. For the HP-EUV-Facility a Harada spectrometer was described and an absolute calibrated energy meter. The calibration of this energy meter was detailed and the use of the spectrometer to provide absolute in-band power measurements of the source. For the VUV-MS-

Facility several spectrometers were discussed covering a 250 – 20 nm wavelength range. These spectrometers included a Seya-Namioka style intensified spectrometer covering 115 – 170 nm, a Czerny-Turner design range 140 – 250 nm, and two Harada style spectrometers covering the 124 – 22 nm, and 20 – 5 nm range. These spectrometers where absolutely calibrated for spectral irradiance. The methods of calibration of these spectrometers were described in detail.

Laser plasma sources require significant equipment and sub systems to provide stable operation. The experimental facilities and their necessary subsystems for investigating these plasmas were described. The three lasers used in these studies to generate laser plasmas were described, in addition to the design of their focusing optic and laser metrology systems. The mechanics, design, and operation of the target management systems were described, which was critical to the operation of the laser plasma sources. The method of alignment and preparation of the target management systems was described in detail.

The underlying physics and mechanics of these laser plasma sources were presented. Additionally, the design of the metrology equipment and the methods used to provide absolute calibration were described. This was followed by a presentation of the experimental data of the plasma emission. Calibrated spectral data of Argon, Krypton, and Xenon gas sources was presented. This was followed by a detailed presentation of data from solid target based plasmas. These targets included Silicon, Copper, Molybdenum, Indium, Tantalum, Tin, and Zinc. The data included broadband spectra covering the VUV range, analysis of spectral lines, in-band power, and conversion efficiency. In addition, at wavelength time resolved imaging of these source was presented showing the scale of these plasmas.

The absolute calibrated spectral measurements of EUV and VUV laser plasma sources are critical to the development of these sources for industrial and scientific applications. With

construction of these calibrated laser plasma metrology facilities, the development of laser plasma source can be explored and insight into the underlying their physics can be gained. Furthermore, the viability and physics can be investigated for novel sources. These plasma source metrology facilities also provide a compact source of light for investigating and measuring EUV and VUV light's interaction with mater, and an illumination source for imaging in these wavelengths. Further studies and experimentation with EUV and VUV sources will provide improvements in brightness and efficiency for XUV sources that are needed across many industries.

LIST OF REFERENCES

[1] I. Newton, *Opticks: or, a treatise of the reflexions, refractions, inflexions and colours of light. Also two treatises of the species and magnitude of curvilinear figures*.: Printers to the Royal Society, 1704.

[2] W. Crookes, "On radiant matter a lecture delivered to the British Association for the Advancement of Science, at Sheffield, Friday, August 22, 1879," *American Journal of Science*, vol. 18, no. 106, pp. 241-262, October 1879.

[3] R. Fitzpatrick, *Plasma Physics: An Introduction*. Boca Raton: CRC Press, 2014.

[4] W. Röntgen, "On a New Kind of Rays," vol. 53, pp. 274-276, 1896.

[5] M. Z. Zainol et al., "Towards improving the etch performance of KrF excimer laser micromachining on silicon material," in *EEE Regional Symposium on Micro and Nanoelectronics (RSM)*, Kuala Terengganu, 2015.

[6] M. Switkes, M. Rothschild, and M. Salvermoser, "Imaging of 1-nm-thick films with 193-nm microscopy," *Optics Letters*, vol. 26, pp. 1182-1184, 2001.

[7] R. D. Allen, G. M. Wallraff, D. C. Hofer, and R. R. Kunz, "Photoresists for 193-nm lithography," *IBM Journal of Research and Development*, vol. 41, no. 1.2, pp. 95-104, 1997.

[8] R. Chao et al., "Advanced in-line metrology strategy for self-aligned quadruple patterning," in *SPIE 9778, Metrology, Inspection, and Process Control for Microlithography XXX, 977813*, 2016.

[9] T. Faure et al., "Development of a new high transmission phase shift mask technology for 10 nm logic node," in *SPIE, Photomask Japan 2016: XXIII Symposium on Photomask and Next-Generation Lithography Mask Technology, 998402*, Japan, 2016.

[10] D. L. Goldfarb, W. Broadbent, M. Wylie, N. Felix, and D. Corliss, "Through-pellicle defect inspection of EUV masks using an ArF-based inspection tool," in *SPIE 9776, Extreme Ultraviolet (EUV) Lithography VII, 97761H*, 2016.

[11] L. Gavilan et al., "VUV spectroscopy of carbon dust analogs: contribution to interstellar extinction," *Astronomy & Astrophysics*, vol. 586, no. A106, 2016.

[12] I. Velchev, W. Hogervorst, and W. Ubachs, "Precision VUV spectroscopy of Ar I at 105 nm," *Journal of Physics B: Atomic, Molecular and Optical Physics*, vol. 32, no. 17, 1999.

[13] A. R. Talley et al., "Results one year after using the 193-nm excimer laser for photorefractive keratectomy in mild to moderate myopia," *American Journal of Ophthalmology*, vol. 118, no. 3, pp. 304-311, 1994.

[14] D. S. Keyes et al., "Optomechanical design and tolerance of a microscope objective at 121.6 nm," in *SPIE 9575, Optical Manufacturing and Testing XI*, 2015.

[15] I. T. R. S. (2011) ITRS lithography roadmap for semiconductors 2011 Edition Lithography. [Online]. http://www.semiconductors.org/clientuploads/Research_Technology/ITRS/2011/2011Lit Lithogra.pdf

[16] D. Attwood, *Soft X-rays and Extreme Ultraviolet Radiation: Principles and Applications*. Berkeley: Cambridge University Press, 1999.

[17] P. Jaeglé, *Coherent sources of XUV radiation: soft X-ray lasers and high-order harmonic generation*. New York: Springer, 2005.

[18] P. A. Tipler and R. A. Llewellyn, *Modern Physics*, 3rd ed. New York: W. H. Freeman and Company, 1999.

[19] T. L. Cottrell, *The Strengths of Chemical Bonds*, 2nd ed. London: Academic Press, 1958.

[20] S. and Capper, P. Kasap, *Springer handbook of electronic and photonic materials*. 2006: Springer.

[21] F. Tran and P. Blaha, "Phys. Rev. Letters," *Accurate Band Gaps of Semiconductors and Insulators with a Semilocal Exchange-Correlation Potential*, vol. 102, no. 226401, 2009.

[22] J. Clark. (2014) Insertion Devices Lecture 2 Wigglers and Undulators. [Online]. https://www.cockcroft.ac.uk/wp-content/uploads/2014/12/CLarke-Lecture-2.pdf

[23] C. Settakorn. (2016) Synchrotron Radiation - Indico - ICTP: Synchrotron Radiation. [Online]. http://indico.ictp.it/event/a0343/session/48/contribution/30/material/0/0.pdf

[24] O. Wood and A. A. MacDowell, "Synchrotron Radiation Sources for EUVL," in *EUV Sources:*, V. Bakashi, Ed.: SPIE Press, 2005, ch. 32.

[25] P. Schmüser, M. Dohlus, J. Rossbach, and C. Behrens, *Free-Electron Lasers in the Ultraviolet & X-Ray Regime*.: Springer Science & Business Media B.V., 2014.

[26] K. Zhukovsky. (2016) High Energy and Short Pulse Lasers: Undulators for Short Pulse X-Ray Self-Amplified Spontaneous Emission-Free Electron Lasers. [Online].

http://www.intechopen.com/books/high-energy-and-short-pulse-lasers/undulators-for-short-pulse-x-ray-self-amplified-spontaneous-emission-free-electron-lasers

[27] Berkeley Laboratory. (2016, June) The Advanced Light Source. [Online]. http://www.als.lbl.gov

[28] Australian Synchrotron. (2016) How is synchrotron light created? [Online]. http://www.synchrotron.org.au/synchrotron-science/how-is-synchrotron-light-created

[29] J. E. Balmer, D. Bleiner, and F. Staub, "Extreme ultraviolet lasers: principles and potential for next-generation lithography," *J. Micro/Nanolith, MEMS MOEMS*, vol. 11, no. 2, 2012.

[30] V. N. Shlyaptsev et al., "Capillary Discharge X-Ray Lasers: The Quest for Sub-10 nm Lasers," *X-Ray Lasers*, vol. 169, pp. 103-112, 2015.

[31] P. Zuppella et al., "Spectral enhancement of a Xe-based EUV discharge plasma source," *Plasma Sources Science and Technology*, vol. 18, 2009.

[32] B. A. Reagan et al., "High-average-power, 100-Hz-repetition-rate, tabletop soft-x-ray lasers at sub-15-nm wavelengths," *Physical Review*, vol. 89, no. 053820, 2014.

[33] E. J. Takahashi, Y. Nabekawa, and K. Midorikawa, "Low-divergence coherent soft x-ray source at 13 nm by high-order harmonics," *Applied Physics Letters*, vol. 84, no. 4, 2004.

[34] U. Stamm et al., "High-power EUV lithography sources based on gas discharges and laser-produced plasmas," in *SPIE 5037, Emerging Lithographic Technologies VII*, 2003, p. 119.

[35] J. Pankert et al., "Physical Properties of the HCT EUV Source," in *SPIE 4688*, 2002, pp. 87-93.

[36] H., Nakarai, H., Abe, T., Nowak, K.M. Mizoguchi et al., "Development of 250W EUV light source for HVM lithography," in *SPIE 10097, High-Power Laser Materials Processing: Applications, Diagnostics, and Systems VI*, 2017.

[37] F. D'Hoore, "ASML," in *Deutshe Bank 2007 Technology Conference*, London, 2007.

[38] J. Fujimoto, T. Hori, T. Yanagida, and H. Mizoguchi, "Development of Laser-Produced Tin Plasma-Based EUV Light Source Technology for HVM EUV Lithography," *Physics Research International*, vol. 2012, no. 249495, 2012.

[39] A. Pirati et al., "EUV lithography performance for manufacturing: status and outlook," in *Extreme Ultraviolet (EUV) Lithography VII, 97760A*, 2016.

[40] D. W. Myers, I. V. Fomenkov, B. A. M. Hansson, B. C. Klene, and D. C. Brandt, "EUV source system development update: advancing along the path to HVM," in *SPIE 5751, Emerging Lithographic Technologies IX*, 2005, p. 248.

[41] K. Takenoshita, "Debris Characterization and Mitigation of Droplet Laser Plasma Sources for EUV Lithography," University of Central Florida, PhD 2006.

[42] M. Richardson et al., "Temporal and Spatial Multiplexing for HMV EUV Sources," in *Sematech Source Workshop*, Baltimore, 2007.

[43] J. -P. Delaboudinière et al., "EIT: Extreme-ultraviolet Imaging Telescope for the SOHO mission," *Solar Physics*, vol. 162, no. 1-2, pp. 291-312, 1995.

[44] L. Juschkin and R. Freiberger, "Two magnification steps EUV microscopy with a Schwarzchild objective and an adapted zone plate lens," in *SPIE Optics+ Optoelectronics: EUV and X-Ray Optics: Synergy between Laboratory and Space*, 2009.

[45] M. D. Seaberg et al., "Ultrahigh 22 nm resolution coherent diffractive imaging using a desktop 13 nm high harmonic source," *Opt. Express*, vol. 19, pp. 22470-22479, 2011.

[46] M. Benk, K. Bergmann, D. Schäfer, and T. Wilhein, "Compact soft x-ray microscope using a gas-discharge light source," *Opt. Lett.*, vol. 33, pp. 2359-2361, 2008.

[47] J. Filevich, K. Kanizay, M. C. Marconi, J. L. A. Chilla, and J. J. Rocca, "Dense plasma diagnostics with an amplitude-division soft-x-ray laser interferometer based on diffraction gratings," *Opt. Lett.*, vol. 25, pp. 356-358, 2000.

[48] J. Ojeda et al., "Harmonium: A pulse preserving source of monochromatic extreme ultraviolet (30–110eV) radiation for ultrafast photoelectron spectroscopy of liquids," *Structural Dynamics*, vol. 3, no. 023602, 2016.

[49] G. E. Moore, "Cramming More Components onto Integrated Circuits," *Electronics*, vol. 38, no. 8, pp. 114–117, 1965.

[50] G. E. Moore, "Progress in Digital Integrated Electronics," *IEEE, IEDM Tech. Digest*, pp. 11-13, 1975.

[51] Intel Corporation. (2017) Intel® Microprocessor Transistor Count Chart. [Online]. http://download.intel.com/pressroom/images/events/moores_law_40th/Transistor_Count_bar_chart.jpg

[52] Intel Corporation. (2006) Dual-Core Intel® Itanium® Processor. [Online]. http://www.intel.com/pressroom/kits/itanium2/

[53] M. Feldman. (2011) Intel Scales Up Cores and Memory with New Westmere EX CPUs. [Online]. https://www.hpcwire.com/2011/04/06/intel_scales_up_cores_and_memory_with_new_westmere_ex_cpus/

[54] P. Alcorn. (2016) Tom's Hardware Guide: Intel Xeon E5-2600 v4 Broadwell-EP Review. [Online]. http://www.tomshardware.com/reviews/intel-xeon-e5-2600-v4-broadwell-ep,4514-2.html

[55] Y. Chen et al., "Self-aligned triple patterning for continuous IC scaling to half-pitch 15nm," in *Optical Microlithography XXIV, 79731P*, 2011.

[56] M. van den Brink, "Shrink, an expanding (litho) market," in *SEMI Industry Strategy Symposium 2007 (ISS 2007)*, 2007.

[57] H. Meiling, "EUVL - getting ready for volume introduction," in *SEMICON West 2010*, 2010.

[58] R. Peeters, "NXE Platform Performance Overview," in *SPIE Advanced Lithography 2014: Lithography V*, 2014, pp. 9048-9054.

[59] M. McLaren, "DUV," in *ASML Investor Day 2014*, London, 2014.

[60] F. van Hout, "EUV," in *ASML Investor Day2014*, London, 2014.

[61] S. Yulin, N. Benoit, T. Feigl, and N. Kaiser, "Interface-engineered EUV multilayer mirrors," *Journal Microelectronic Engineering*, vol. 83, 2006.

[62] J. van Schoot et al., "EUV Lithography High-NA Scanner for Sub 8 nm Resolution," in *ASML 2016 International Workshop on EUV Lithography*, 2016.

[63] T. Wallow et al., "Evaluation of EUV resist materials for use at the 32 nm half-pitch node," in *Emerging Lithographic Technologies XII, 69211F*, 2008.

[64] Y. Hishiro, "Novel EUV resist development for 13nm half pitch," in *JSR Micro Inc, 2016 International Workshop on EUV Lithography*, 2016.

[65] EDGAR Online, Inc. (2016, February) Intel Corp. Form 10-K: Annual Report February. [Online]. http://files.shareholder.com/downloads/INTC/867590276x0xS50863-16-105/50863/filing.pdf

[66] J. A. Samson and D. L. Ederer, *Vacuum Ultraviolet Spectroscopy*, 1st ed. San Diego: Academic Press, 1972.

[67] B. L. Henke, E. M. Gullikson, and J. C. Davis, "X-ray interactions: photoabsorption, scattering, transmission, and reflection at E=50-30000 eV," *Atomic Data and Nuclear Data Tables*, vol. 54, no. 2, pp. 181-342, 1993.

[68] S. A. George, "Spectroscopic studies of laser plasmas for EUV sources," University of Central Florida, PhD Thesis 2007.

[69] A. G. Michette, *Optical systems for soft x-rays*, 1st ed. New York: Plenum Press, 1986.

[70] E. Hecht, *Optics*, 4th ed. New York: Pearson/Addison Wesley, 2002.

[71] E. Meltchakov, V. Vidal, H. Faik, M-J. Casanove, and B Vidal, "Performance of multilayer coatings in relationship to microstructure of metal layers. Characterization and

optical properties of Mo/Si multilayers in extreme ultra-violet and x-ray ranges," *Journal of Physics: Condensed Matter*, vol. 18, no. 13, pp. 3355-3365, 2006.

[72] J. A. R. Samson, *Techniques of vacuum ultraviolet spectroscopy*. New York: Wiley, 1967.

[73] A. Giuliani et al., "A differential pumping system to deliver windowless VUV photons at atmospheric pressure," *J. Synchrotron Rad*, vol. 18, pp. 546-549, 2011.

[74] Laseroptik. (2016) Laseroptik: Transmission Curves. [Online]. http://lo.de/index.php?Catalog:Substrates:Transmission_Curves

[75] R. Sauerbrey and H. Langhoff, "Excimer ions as possible candidates for VUV and XUV lasers," *IEEE Journal of Quantum Electronics*, vol. 21, no. 3, pp. 179-181, 1985.

[76] W. Silvast, *Laser Fundamentals*, 2nd ed. Cambridge: Cambridge University Press, 2004.

[77] A. Ozawa, Z. Zhao, M. Kuwata-Gonokami, and Y. Kobayashi, "High average power coherent vuv generation at 10 MHz repetition frequency by intracavity high harmonic generation," *Opt. Express*, vol. 23, pp. 15107-15118, 2015.

[78] Hamamatsu Photonics K.K. (2016) DEUTERIUM LAMPS L2D2 LAMPS. [Online]. https://www.hamamatsu.com/resources/pdf/etd/L2D2_TLS%201006E.pdf

[79] I. Bezel, A. Shchemelinin, and M. A. Panzer, "Laser Sustained Plasma Bulb Including Water," 20140042336 A1, Feb 13, 2014.

[80] I. Bezel et al., "High Power Laser-Sustained Plasma Lightsources for KLA-Tencor Broadband Inspection Tools," in *CLEO: 2015*, 2015, p. ATu4M.2.

[81] M. Masnavi, J. Szilagyi, H. Parchamy, and M. Richardson, "Laser-based plasma sources at 6.6 and 60 nm," in *CLEO: 2013*, 2013, p. JW1D.2.

[82] J. Szilagyi, H. Parchamy, M. Masnavi, and M. C. Richardson, "Laser-based vacuum-ultraviolet light source," in *SPIE Advanced Lithography 2014: Metrology, Inspection, and Process Control for Microlithography XXVIII*, 2014, pp. 9050-9080.

[83] N. Gambino, B. Rollinger, M. Brandstätter, and R. S. Abhari, "Vacuum ultraviolet spectral emission properties of Ga, In and Sn droplet-based laser produced plasmas," *Spectrochimica Acta Part B: Atomic Spectroscopy*, vol. 122, pp. 149-156, 2016.

[84] O. Kostko, B. Bandyopadhyay, and M. Ahmed, "Vacuum Ultraviolet Photoionization of Complex Chemical Systems," *Annual Review of Physical Chemistry*, vol. 67, pp. 19-40, 2016.

[85] J. Morgan,. New York: McGraw-Hill, 1953, p. 57.

[86] B. W. Smith, F. Yongfa, M. Slocum, and L. Zavyalova, "25 nm immersion lithography at 193 nm wavelength," *International Society for Optics and Photonics: Microlithography*, pp. 141-147, 2005.

[87] J. A. Hoffnagle, W. D. Hinsberg, M. Sanchez, and F. A. Houle, "Liquid immersion deep-ultraviolet interferometric lithography," *J. Vac. Sci. and Tech. B*, vol. 17, pp. 3306-3309, 1999.

[88] A. C. Parr, R. U. Datla, and J. L. Gardner, Eds., "Volume 41: Experimental Methods in the Physical Sciences," in *Optical Radiometry*. San Diego: Elsevier Academic Press, 2005.

[89] W. L. Kruer, *The Physics of Laser Plasma Interactions*.: Westview Press, 2003.

[90] C. Keyser, G. Schriever, and M. Richardson, "Studies of high-repetition-rate laser plasma EUV sources from droplet targets," *Applied Physics A: Materials Science and Processing*, vol. 77, pp. 217-221, 2003.

[91] F. F. Chen, *Introduction to Plasma Physics*. New York: Plenum Press, 1974.

[92] D. Giulietti and L. A. Gizzi, "X-ray emission from laser produced plasmas," *La Rivista del Nuovo Cimento*, vol. 21, no. 10, pp. 1-93, 1998.

[93] R. J. Goldston and P. H. Rutherford, *Introduction to Plasma Physics*. Philadelphia: Institute of Physics Publishing, 1995.

[94] D. Salzmann, *Atomic Physics in Hot Plasmas*.: Oxford University Press, 1998.

[95] M. Richardson et al., "EUV Sources for Lithography," in *Laser Plasma EUV Sources based on Droplet Target Technology*.: SPIE Press, 2005.

[96] M. Klapisch et al., "Interpretation of unresolved transition arrays in the soft-x-ray spectra of highly ionized molybdenum and palladium," *Physical Review A*, vol. 25, no. 4, pp. 2391--2394, 1982.

[97] D. Colombant and G. F. Tonon, "X-ray emission in laser-produced plasmas," *Journal of Applied Physics*, vol. 44, pp. 3524-3537, 19873.

[98] I. C. E. Turcu and J. B. Dance, *X-rays from Laser Plasmas*.: John Wiley and Sons, 1999.

[99] M. Al-Rabban, "Term structure of 4d-electron configurations and calculated spectrum in Sn-isonuclear sequence," *J. Quantitative Spectroscopy & Radiative Transfer*, vol. 97, pp. 278-316, 2006.

[100] M. Al-Rabban et al., "Radiation transport modeling for Xe and Sn-doped droplet laser-plasma sources," in *SPIE, 5751*, 2005, pp. 769-778.

[101] M. Al-Rabban, M. Richardson, and H. Scott, "Modeling LPP Sources," in *EUV Sources for Lithography*, V. Bakashi, Ed. Bellingham: SPIE Press, 2005, ch. 10.

[102] M. Masnavi, J. Szilagyi, H. Parchamy, and M. Richardson, "Laser-plasma source parameters for Kr, Gd, and Tb ions at 6.6 nm," *Applied Physics Letters*, vol. 102, p. 164102, 2013.

[103] J. Szilagyi, H. Parchamy, M. Masnavi, and M. Richardson, "Spectral irradiance of singly and doubly ionized zinc in low-intensity laser-plasma ultraviolet light sources," *J. Appl. Phys*, vol. 121, no. 033303, 2017.

[104] C. S. Koay, "Radiation studies of the tin-doped microscopic droplet laser plasma light source specific to EUV lithography," PhD Thesis 2006.

[105] J. Christiansen, D. Ashby, and K. Roberts, "MEDUSA: a one-dimensional laser fusion code," *Computer Physics Communication*, vol. 7, pp. 271-287, 1974.

[106] N. W. Ashcroft, N. W. Mermin, and N. D. Mermin, *Solid State Physics*. New York: Holt, Rinehart and Winston, 1976.

[107] M. Lenzner and W. Rudolph, "Laser-Induced Optical Breakdown in Solids," in *Strong Field Laser Physics*, T. Bravec, Ed.: Springer Science+Buisness Media, LLC, 2008.

[108] L. Shah, "Femtosecond Laser Micro-Machining of Glasses and Polymers in Air," University of Central Florida, PhD 2001.

[109] N. Chichkov, C. Momma, S. Nolte, F. von Alvensle, and A. Tiinnermann, "Femtosecond, picosecond and nanosecond laser ablation of solids," *Applied Physics A*, vol. 63, pp. 109-115, 1996.

[110] A. Ben-Yakar, A. Harkin, J. Ashmore, R. L. Byer, and H. A. Stone, "Thermal and fluid processes of a thin melt zone during femtosecond laser ablation of glass: the formation of rims by single laser pulses," *J Phys D Appl Phys*, vol. 40, no. 5, pp. 1447–1459, 2007.

[111] H. A. Bender, D. O'Connell, and W. T. Silfvast, "Velocity characterization of particulate debris from laser-produced plasmas used for extreme-ultraviolet lithography," *Applied Optics*, vol. 34, pp. 6513-6521, 1995.

[112] P. E. Ciddor, "Refractive index of air: new equations for the visible and near infrared," *Appl. Optics*, vol. 35, pp. 1566-1573, 1996.

[113] R. Peeters et al., "ASML's NXE platform performance and volume introduction," in *Extreme Ultraviolet (EUV) Lithography IV, 86791F*, 2013.

[114] R. Bernath et al., "Advanced Droplet and Plasma Targeting System," 7,718,985 Bl, May 18, 2010.

[115] F. R. S. Lord Rayleigh, "On the Instability of Jets," *Proc. London Math. Soc.*, vol. s1-10, no. 1, pp. 4-13, 1878.

[116] B. R. Munson, D. F. Young, and T. H. Okiishi, *Fundamentals of fluid mechanics*. Hoboken: J Wiley & Sons, 2006.

[117] P. M. Gerhart, R. J. Gross, and J. I. Hochstein, *Fundamentals of Fluid Mechanics*. Reading: Addison-Wesley Pub. Co., 1992.

[118] R. H. Perry and D. W. Green, *Perry's chemical engineers' handbook*. New York: McGraw-Hill, 2008.

[119] J. E. A. John and T. G. Keith, *Gas Dynamics*, 3rd ed.: Pearson Prentice Hall, 2006.

[120] N. Nakano, H. Kuroda, T. Kita, and T. Harada, "Development of a flat-field grazing-incidence XUV spectrometer and its application in picosecond XUV spectroscopy," *Applied Optics*, vol. 23, pp. 2386-2392, 1984.

[121] T. Harada, K. Takahashi, H. Sakuma, and A. Osyczka, "Optimum design of a grazing-incidence flat-field spectrograph with a spherical varied-line-space grating," *Applied Optics*, vol. 38, pp. 2743-2748, 1999.

[122] Ocean Optics, Inc., "Maya2000, Maya 2000Pro, and Maya2000Pro VIS-NIR Spectrometers Installation and Operation Manual: Document Number 020-00000-000-02-201207," Dunedin, 2009.

[123] Opto Diode, "AXUV/SXUV/UVG Salient Applications," Newbury Park, 2014.

[124] S. Schröder, T. Feigl, A. Duparré, and A. Tünnermann, "EUV reflectance and scattering of Mo/Si multilayers on differently polished substrates," *Optics Express*, vol. 15, pp. 13997-14012, 2007.

[125] Y. Jang, "High-resolution Time-resolved Imaging System in the Vacuum Ultraviolet Region," MS Thesis 2014.

[126] N. J. Mason et al., "VUV spectroscopy and photo-processing of astrochemical ices: an experimental study," *Faraday Discussions*, pp. 311-329, 2006.

[127] C-S. Koay, K. Takenoshita, and E. Fujiwara, "Spectroscopic studies of the Sn-Based droplet laser plasma EUV source," in *Emerging Lithographic Technologies VII*, 2004, p. 965.

[128] R. Stuik, F. Scholze, J. Tummler, and F. Bijkerk, "Absolute calibration of a multilayer based xuv diagnostic," *Nucl. Instrum. Methods*, vol. 492, pp. 305-316, 2002.

[129] I.J. Sola et al., "Sources of VUV radiation by high harmonic generation and their characteristics," in *2011 10th Euro-American Workshop on Information Optics (WIO)*, Benicassim, 2011, pp. 1-2.

[130] T. Schmid et al., "High repetition-rate LPP-source facility for EUVL," in *Emerging Lithographic Technologies XI*, vol. 6517, 2007.

[131] Varian, Inc., *Multi-Gauge Controller Document No. 699908091, Revision Y: Appendix A*. Lexigton: Varian, Inc., 2007.

[132] D. Daumont, J. Brion, J. Charbonnier, and J. Malicet, "Ozone UV spectroscopy I: Absorption cross-sections at room temperature," *Journal of Atmospheric Chemistry*, vol. 15, no. 2, pp. 145-155, 1992.